Universidade de Aveiro Departamento de Física
2014

Lara Filipa das Neves Dias Carramate

Desenvolvimento de um sistema de Tomografia Computorizada de contagem de fotão único usando MPGDs

Development of a single photon counting Computed Tomography system using MPGDs

Universidade de Aveiro Departamento de Física
2014

Lara Filipa das Neves Dias Carramate

Desenvolvimento de um sistema de Tomografia Computorizada de contagem de fotão único usando MPGDs

Development of a single photon counting Computed Tomography system using MPGDs

Tese apresentada à Universidade de Aveiro para cumprimento dos requisitos necessários à obtenção do grau de Doutor em Engenharia Física, realizada sob a orientação científica do Doutor João Filipe Calapez de Albuquerque Veloso, Professor Auxiliar do Departamento de Física da Universidade de Aveiro e co-orientação do Doutor Augusto Marques Ferreira da Silva, Professor Auxiliar do Departamento de Electrónica, Telecomunicações e Informática da Universidade de Aveiro.

Este trabalho for parcialmente financiado pelos projetos PTDC/FIS/110925/2009 e CERN/FP/123604/2011 através dos programas FEDER e FCT. Apoio financeiro da FCT através da Bolsa de Doutoramento com a referência SFRH/BD/71429/2010.

Aos meus pais.
Ao meu irmão.
Ao Armindo.

o júri / the jury

presidente / president

Prof. Doutor Nelson Fernando Pacheco da Rocha
Professor Catedrático da Secção Autónoma de Ciências da Saúde da Universidade de Aveiro

vogais / examiners committee

Prof. Doutor Joaquim Marques Ferreira dos Santos
Professor Catedrático da Faculdade de Ciências e Tecnologia da Universidade de Coimbra

Prof. Doutor Luís Filipe dos Santos Garcia Peralta
Professor Associado com Agregação da Faculdade de Ciências da Universidade de Lisboa

Prof. Doutor Pedro Miguel Dinis de Almeida
Professor Auxiliar com Agregação da Faculdade de Ciências da Universidade de Lisboa

Doutor Luís Manuel Panchorrinha Fernandes
Investigador do Grupo de Instrumentação Atómica e Nuclear da Faculdade de Ciências e Tecnologia da Universidade de Coimbra

Doutora Ana Luísa Monteiro da Silva
Investigadora de Pós-Doutoramento da Universidade de Aveiro

Prof. Doutor Augusto Marques Ferreira da Silva
Professor Auxiliar do Departamento de Eletrónica, Telecomunicações e Informática da Universidade de Aveiro

Prof. Doutor João Filipe Calapez de Albuquerque Veloso
Professor Auxiliar do Departamento de Física da Universidade de Aveiro

agradecimentos /
acknowledgements

Na fase final deste trilho com os usuais precalços, mas também com muitas paisagens agradáveis, não posso deixar de agradecer muito sinceramente a todos os que caminharam junto a mim ou se encontraram comigo algures no percurso. Muitos me apoiaram nos dias cinzentos e apreciaram comigo as paisagens fantásticas que foram surgindo, fazendo desta, uma aventura muito especial.

Agradeço, especialmente, ao Professor Doutor João Veloso, por me ter dado a oportunidade de trilhar este caminho junto de si e da sua equipa, a grande DRIM *team*, e de participar nos seus projectos de investigação. Obrigada por apostar na minha formação e crescimento.

Agradeço aos meus Orientadores, Professor Doutor João Veloso e Professor Doutor Augusto Silva, por darem um passo de cada vez comigo neste percurso, desde o ponto de partida até ao destino. Muito obrigada pela cuidadosa orientação, pela disponibilidade, pelas proveitosas discussões científicas, pela partilha de experiências e pela amizade.

Quero agradecer também à Fundação para a Ciência e Tecnologia por me ter atribuído uma Bolsa de Doutoramento e ao I3N - Departamento de Física da Universidade de Aveiro pelas condições de trabalho que proporcionou, incluindo aos técnicos Ivo Mateus, Miguel Rocha, Francisco Reis e Júlio Gonçalves.

Não posso deixar de agradecer aos meus fantásticos colegas da DRIM *team* pelo bom ambiente durante o caminho, pelo espírito de equipa, pela ajuda sempre que precisei, por todos os ensinamentos. Ana, Anabela, Andrêa, Arouca, Cacia, Carlitos, Daniel, Fábio, Hugo, Lipe, Luís e Pedro... muito obrigada!

Um agradecimento especial ao Doutor Carlos Azevedo pela revisão desta tese, pela partilha de conhecimento e pela permanente disponibilidade; e ao Doutor Filipe Castro pela revisão linguística.

I would like to thank to Fraunhofer Institute, especially to Frank Nachtrab and his group, particularly Markus Firsching and Thomas Ebensperger and also, to Michael Salamon and Thomas Hofmann for sharing their knowledge and for having made my stay more pleasant.

Um grande obrigada aos meus amigos pelo apoio, pela força, pelo carinho, pelos momentos de boa disposição e descontração, por me fazerem sentir mais eu e tornarem tudo mais fácil!

Pelo constante suporte, dedicação e carinho que me permitiram chegar ao final do trilho, a minha maior gratidão é dirigida à minha família. Acreditaram sempre em mim, mesmo nos momentos em que eu própria duvidei! Especialmente ao Armindo, pelo apoio incondicional, pela imensa paciência e pela compreensão de cada vez que não estive presente.

Muito Obrigada a todos!
É apenas o início da caminhada!!

Palavras Chave

Tomografia computorizada, detectores gasosos microestruturados, resolução em energia, tomografia computorizada espetral, contagem de fotão único

Resumo

O desenvolvimento de sistemas de tomografia computorizada que incorporem detetores com resolução em energia é um desafio atual em física médica e engenharia biomédica. Um sistema de tomografia computorizada espetral permite obter informações complementares comparativamente a um sistema convencional, que podem auxiliar no diagnóstico médico, sendo por isso de grande interesse em medicina. O trabalho exposto nesta tese prende-se com o desenvolvimento de um sistema de tomografia usando detetores gasosos microestruturados que permitem, simultaneamente, ter informação da posição de interacção e da energia de cada fotão que interage com o detetor. Este tipo de detetores possui ainda outras vantagens relativamente a custo ou características de funcionamento quando comparados com detetores de estado sólido. Foram realizadas aquisições tomográficas usando um detetor baseado numa MicroHole & Srip Plate que permitiu reconstruir imagens utilizando diferentes gamas de energia, aplicar técnicas de ponderação em energia e fazer pela primeira vez reconstrução multi-corte e obter imagens tri-dimensionais. Aplicando a técnica de ponderação em energia foi possível melhorar a relação contraste-ruído em 31% comparativamente à imagem correspondente aquela obtida nos actuais sistemas médicos. Posteriormente, foi desenvolvido um protótipo de um sistema de tomografia computorizada com flexibilidade para alterar o detetor, tornando possível utilizar vários detetores baseados na microestrutura Thick-COBRA. São apresentadas várias imagens adquiridas com estes detetores que evidenciam a sua aplicabilidade em imagiologia por raio-X. A operar no meio gasoso $NeCH_4$ o detetor permitiu um ganho de 8×10^4, uma resolução em energia de 20% (largura a meia altura a 8 keV), uma taxa de contagem de 1×10^6 Hz/mm^2, um funcionamento muito estável (variações de ganho inferiores a 5%) e uma resolução espacial de 1.2 mm para fotões de 3.6 keV. A operar em Kr puro foi possível aumentar a eficiência de deteção e alcançar um ganho de 2×10^4, uma resolução em energia de 32% (largura a meia altura a 22 keV), uma taxa de contagem de 1×10^5 Hz/mm^2, um funcionamento também bastante estável e uma resolução espacial de 500 μm. O software já existente no grupo para reconstrução de imagem foi melhorado e foram ainda desenvolvidas ferramentas para correcção de desalinhamentos geométricos do sistema. As reconstruções obtidas após correção geométrica surgem livres de artefactos originados pelos referidos desalinhamentos.

Keywords

Computed tomography, micropattern gaseous detectors, energy resolution, spectral computed tomography, single photon counting

Abstract

The development of computed tomography systems with energy resolving detectors is a current challenge in medical physics and biomedical engineering. A computed tomography system of this kind allows getting complementary informations relatively to conventional systems, that can help the medical diagnosis, being of great interest in medicine. The work described in this thesis is related to the development of a computed tomography system using micropattern gaseous detectors, which allow storing, simultaneously, information about the interaction position and the energy of each single photon that interacts with the detector. This kind of detectors has other advantages concerning the cost and characteristics of operation when compared with solid state detectors. Tomographic acquisitions were performed using a MicroHole & Strip Plate based detector, which allowed reconstructing cross-sectional images using energy windows, applying the energy weighting technique and performing multi-slice and tri-dimensional reconstructions. The contrast-to-noise ratio was improved by 31% by applying the energy weighting technique, comparing with the corresponding image obtained with the current medical systems. A prototype of a computed tomography with flexibility to change the detector was developed, making it possible to apply different detectors based on Thick-COBRA. Several images acquired with these detectors are presented and demonstrate their applicability in X-ray imaging. When operating in NeCH_4, the detector allowed a charge gain of 8×10^4, an energy resolution of 20% (full width at half maximum at 8 keV), a count rate of 1×10^6 Hz/mm^2, a very stable operation (gain fluctuations below 5%) and a spacial resolution of 1.2 mm for an energy photon of 3.6 keV. Operating the detector in pure Kr allowed increasing the detection efficiency and achieving a charge gain of 2×10^4, an energy resolution of 32% (full width at half maximum at 22 keV), a count rate of 1×10^5 Hz/mm^2, very stable operation and a spatial resolution of 500 μm. The software already existing in the group was improved and tools to correct geometric misalignments of the system were also developed. The reconstructions obtained after geometrical correction are free of artefacts due to the referred misalignments.

Contents

LIST OF ABBREVIATIONS AND SYMBOLS

2D	two-dimensional
3D	three-dimensional
ADC	Analogue to Digital Converter
ASIC	application specific integrated circuit
CCD	charge-coupled device
CNR	contrast-to-noise ratio
CT	Computed Tomography
CdTe	cadmium telluride
CZT	cadmium zinc telluride
DRIM	*Deteção de Radiação e Imagiologia Médica* - Radiation Detection and Medical Imaging
EWT	energy weighting technique
FBP	filtered backprojection
FOV	field-of-view
FT	Fourier transform
FWHM	full width at half maximum
GEM	Gas Electron Multiplier
GUI	graphical user interface
IDE	integrated development environment
IFT	inverse Fourier transform
LSF	line spread function
MCA	multi-channel analyser
MCP	microchannel plate
MHSP	MicroHole and Strip Plate
MPGD	MicroPattern Gaseous Detectors
MRI	Magnetic Resonance Imaging
MSMS	multislit multislice

MSP Micro Strip Plate

MSV mean square voltage

MTF modulation transfer function

MWPC Multiwire Proportional Counter

NIM nuclear instrumentation module

PCB printed circuit board

PEEK polyetheretherketone

PET Positron Emission Tomography

PMMA poly(methyl methacrylate)

PSF point spread function

ROI region of interest

Si silicon

SIM subscriber identity module

SDD source-to-detector distance

SOD source-to-object distance

SNR signal-to-noise ratio

SPECT single photon emission computed tomography

THCOBRA Thick-COBRA

THGEM Thick-GEM

USB Universal Serial Bus

List of Figures

List of Tables

INTRODUCTION

Computed Tomography (CT) is an X-ray imaging modality that allows the acquisition of cross-sectional images of objects such as the human body without superposition of structures from adjacent planes. This imaging modality allowed overcoming the limitations of conventional radiography, in which transmission images are obtained and a three-dimensional (3D) volume is projected in a two-dimensional (2D) image. CT images also have a contrast resolution higher than conventional radiography and were a crucial advance for diagnosis in Medicine, becoming thus an essential imaging tool on clinical environments. This imaging modality is widely installed in hospitals, including emergency services which are equipped with fast CT scanners to cope with trauma situations. Besides health care, CT is also used in forensic, archaeological, biomedical research and in industry quality control applications. [1]

CT has now a very good performance due to decades of research, however there is still space for improvement, namely in the radiation detectors. Recent developments in detectors provide the basis to extract more information when compared to current detector technology used in the commercial devices. However, the new detectors technology is not sufficiently matured and further improvements (studies) are needed in order to reach a stable operation and fulfil the specifications enabling the tomographic process to produce useful and good quality images.

This thesis describes the work performed in order to develop a single photon CT system using MicroPattern Gaseous Detectors (MPGDs). MPGDs applied in this system allow single photon detection and have energy resolving capability.

As a result of this thesis, a software package dedicated to image reconstruction, a Thick-COBRA (THCOBRA) [2] detector and a prototype of a CT system using a MPGD were

developed. During the work, problems were found in the detector development (as for example detector window) and in the search for adequate electronic parameters to operate the detector. These were solved by a thorough study addressing several ways to reach the main goal and elaborating study plans to search several combinations of electronic parameters. Other problems were found in the image reconstruction process, that were solved by careful reading of methodologies already implemented in many other systems.

The focus of this work was the development of CT systems using MPGDs, specifically the MicroHole and Strip Plate (MHSP) and the THCOBRA, including system alignment, synchronization of object motion and data acquisition, electronics instrumentation, as well as the definition of the detector operation conditions and parameters.

This thesis is divided into three main parts. The first part includes two chapters devoted to theoretical concepts, the second part one chapter describing the experimental setup and the third part five chapters where the main results are presented and discussed.

The initial subsections of the first chapter introduce and prepare the reader for the main theme of this thesis by addressing the interaction of radiation with matter and the production of X-rays with an X-ray tube. After these, a historic perspective of the evolution of CT systems is made referring the main milestones and their characteristics. This chapter ends with a revision of the state-of-the-art of CT systems using detectors with energy resolving capability.

The second chapter is related to gaseous detectors, explaining in different subsections their basic principles, the principle of operation of avalanche gaseous detectors and some general detector characteristics. A subsection is dedicated to the MPGD, the type of detectors used in this work.

The third chapter, included in the second part, describes the experimental assembly: X-ray tube, stepper motor, alignment system, detectors and electronics instrumentation. In this chapter, the method to reconstruct the cross-sectional images and the developed software are described.

The results are presented in the third part of this thesis. Chapter four presents the CT images obtained with 2D-MHSP detector using energy weighting technique, energy windowed images, multi-slice reconstruction and 3D images.

Since the sensitive area of the detectors was increased, a simulation to evaluate the geometry of the reconstruction algorithm was done, intending to verify the applicability of the parallel geometry to the next system configurations. The description and the results are described in chapter five.

Chapters six and seven present the results of 2D-THCOBRA based detectors operating in Ne/CH_4 (95 /5). In chapter six are presented the cross-sectional images acquired with a more complex detector configuration with a Thick-Gas Electron Multiplier (THGEM) structure to have a charge pre-amplification stage. Chapter seven describes the results of characterization

and imaging of a simpler detector, implemented after the initial configuration, in which the THGEM was removed.

The last chapter of the third part (chapter eight) has the characterization results of the 2D-THCOBRA detector operating in pure Kr and the first X-ray images acquired with this detector.

Finally, the conclusions and future work summarize the main results of this work, referring the aspects to improve in the future and some of the work that is still to be done.

The results achieved in this work were published in international peer-reviewed journals and presented in oral and poster communications in national and international conferences. Examples of these publications are *"THCOBRA X-ray imaging detector operating in Ne/CH_4"*, *"Multi-slice quantum Computed Tomography system using a MHSP"* and *"Energy weighting technique in Quantum Computed Tomography using a MPGD"*. All other contributions are listed in Appendixes.

Part I

FUNDAMENTALS

CHAPTER

1

COMPUTED TOMOGRAPHY

1.1 Interaction of Photons with Matter

The understanding of radiation interaction with matter is fundamental to the design of the experimental equipments, configurations, procedures, data analysis and results interpretation. In this work, the X radiation was produced using an X-ray tube and natural radioactive sources such as ^{109}Cd.

The capacity of the radiation to penetrate matter strongly depends on the material and photon energy. The interaction of photons with matter leads to the attenuation of the beam, i.e., the decrease of beam intensity by photon absorption/scattering. Considering a monoenergetic X-ray beam passing through an attenuation medium, its intensity decreases exponentially as the object thickness increases, as described by the Lambert-Beer's Law:

$$I = I_0 e^{-\mu(E)x} \tag{1.1}$$

where I is the final intensity, I_0 is the initial intensity (before interaction), μ is the linear attenuation coefficient, expressed in cm^{-1}, E is the energy of the incident photons and x the thickness of the material (expressed in cm) crossed by the beam [3–7]. An illustration of this process can be seen in Figure 1.1. The linear attenuation coefficient is the sum of the

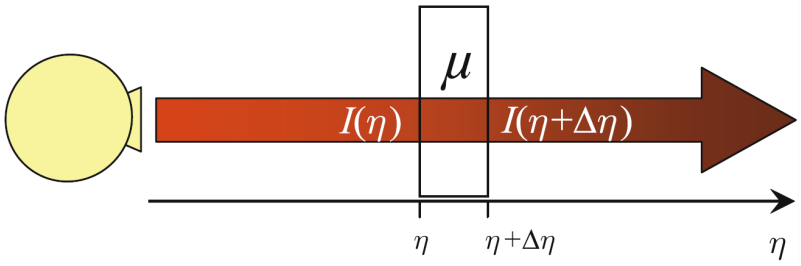

Figure 1.1: Lambert-Beer law illustration for a monochromatic beam and one material (one attenuation coefficient) [adapted from [3]].

attenuation coefficients that correspond to the different interaction processes, determined as:

$$\mu = \omega + \tau + \sigma + \kappa \tag{1.2}$$

where ω corresponds to the Rayleigh scattering, τ corresponds to the Photoelectric absorption, σ relates to the Compton scattering and κ corresponds to the pair production [4]: the possible mechanisms of interaction of photons with matter. Figure 1.2 shows the total radiation attenuation due to the different processes as a function of the incident photon energy in pure Xe and pure Kr. It can be seen that pair production only occurs for higher energies (above approximately 1 MeV) than those used in this work, therefore this process will not be addressed any further in this work.

The attenuation coefficients depend on energy and, since X-ray tubes produce a polychro-

matic X-ray spectrum (1.2.1.1), the effective energy, which is the energy of the equivalent mono-energetic beam, has to be considered. Therefore, the effective attenuation coefficient can be considered, μ_{eff}. The intensity, I, measured at the detector reflects the X-ray attenuation along its path, named line integral and written as follows [8]:

$$I = I_0 e^{-\int \mu(x,y,E_{eff})dx} \tag{1.3}$$

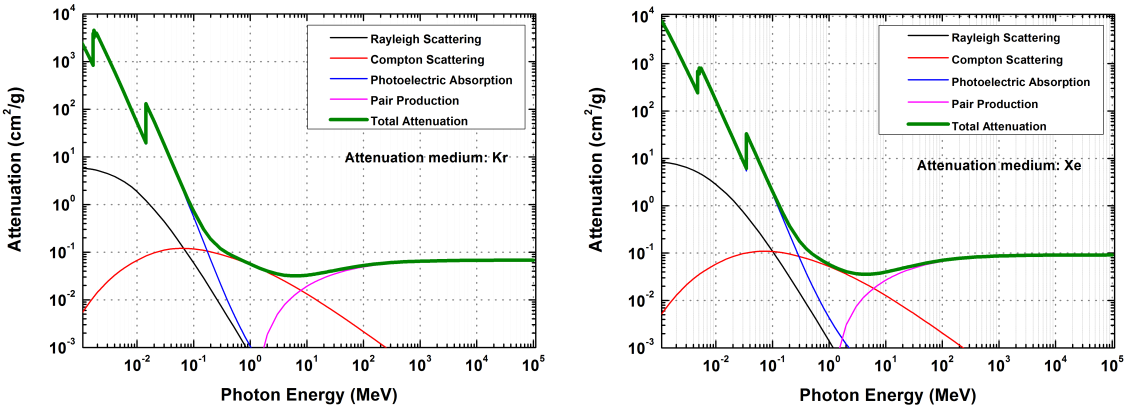

Figure 1.2: Attenuation for Kr (left) and Xe (right) as a function of the photon energy, showing the different processes that contribute for the attenuation [9].

1.1.1 Rayleigh Scattering

The Rayleigh scattering, also known as coherent or classical scattering, relates to the interaction of a photon with the atom (both nucleus and shell electrons). It occurs mainly for low energy photons, specially in mammography which uses between 15 and 30 keV, and for higher atomic number materials. In Rayleigh scattering, the atom electrons oscillate in phase due to the electric field of the photon's electromagnetic wave. The cloud of electrons radiates energy, emitting a photon with the same energy as the incident photon and a slightly different direction (Figure 1.3). The angle between the incident and the emitted photon increases for lower energies. In this physical process no excitation or ionization occurs. [4, 5, 7, 10] In medical imaging, this process decreases image quality if the ejected photon is detected. [4]

1.1.2 Compton Scattering

Compton scattering, also known as inelastic or non-classic scattering, refers to an interaction between the incident photon and an electron of an outer shell in which atom ionization occurs. The electron, named recoil electron, is ejected from the atom and the photon is deflected by an angle θ with lower energy (Figure 1.4). [4, 5, 7, 10] The kinetic energy of the ejected electron,

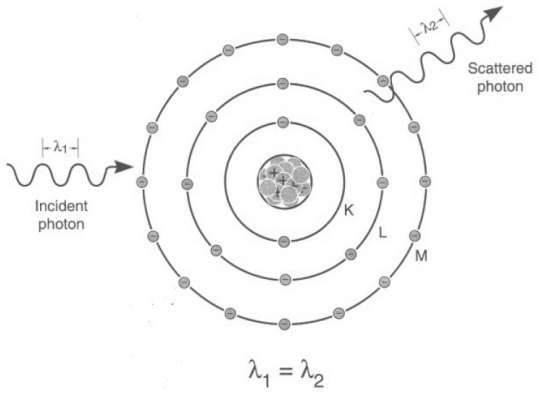

Figure 1.3: Illustration of the Rayleigh scattering effect, showing the interaction between the incident photon and the electrons of the atom. The incident and emitted photons have the same energy [adapted from [4]].

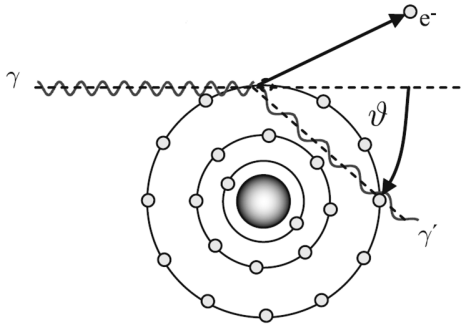

Figure 1.4: Compton scattering in which the incident photon interacts with the outer shell electron and a photon with lower energy is emitted [adapted from [3]].

$E_{c_{e^-}}$, is equal to the difference of the incident photon energy, E_{inc}, and the scattered photon energy, E_{sc} [4, 10]:

$$E_{c_{e^-}} = E_{inc} - E_{sc} \tag{1.4}$$

As the binding energy of the electron is small comparatively to the inner shell electrons, it can be ignored [4], however, for a Compton scattering to take place, the energy of the incident photon has to be higher than the electron binding energy. The probability of Compton interaction increases with the increase of incident photon energy (when compared to Rayleigh scattering or photoelectric effect) and linearly with the atomic number, since it depends on the number of electrons in the tissue/material. [4, 5, 10]

Compton scattering predominates on the diagnostic energy range for soft tissue. The scattered photons that are detected reduce the image contrast, contributing to a degradation of image quality. [4]

1.1.3 Photoelectric Effect

The photoelectric effect occurs when an inner shell electron is ejected (photoelectron) from the atom due to a total transfer of the incident photon energy (Figure 1.5) [4, 5, 7, 10]. The

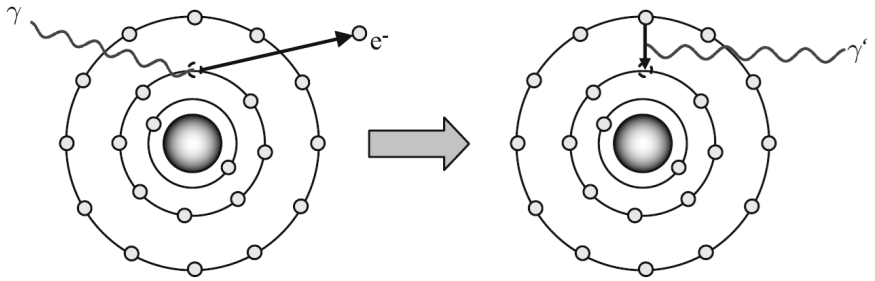

Figure 1.5: Scheme of photoelectric effect. The incident photon interacts with an inner shell electron, that is ejected from the atom. Then, an electron from an outer shell fills the vacancy and a characteristic photon is emitted [adapted from [3]]

photoelectric absorption occurs only if the energy of the incident photon is equal to or greater than the binding energy of the electron. The more probable ejected electron is the one with binding energy closer to, but smaller than, the incident photon energy. The kinetic energy of the ejected electron, $E_{c_{e^-}}$, is equal to the difference between the incident photon energy, E_{inc}, and the electron binding energy, E_b [4, 5, 10]:

$$E_{c_{e^-}} = E_{inc} - E_b \tag{1.5}$$

Once the inner electron is ejected, a vacancy in the shell is created. This hole can be filled through capture of a free electron from the medium or by an electron from an outer shell. If the latter occurs, another vacancy is created and the process is repeated. Since the energy of each shell is characteristic of the atomic element, the energy difference between the shells is converted into characteristic X-rays or Auger electrons (ejected orbital electron). As the characteristic X-ray emission probability decreases for lower atomic numbers of the absorber material, it will not be predominant in soft tissue in the diagnostic energy range. [4, 5, 10]

The photoelectric effect is predominant for low energy photons in high atomic number materials, being proportional to $\frac{Z^3}{E^3}$, with Z being the atomic number and E the incident photon energy. In general, the photoelectric absorption probability decreases as the energy increases and, in part, this explains the image contrast reduction when higher energies are used. However, as seen in Figure 1.2, taking the example of Kr, the probability increases suddenly when the energy of the incident photon is high enough to ionize an inner shell (approximately 1.9 keV and 14.3 keV, corresponding to L and K shells), and then starts to decrease again, which translates into sharp edges in the attenuation spectrum (absorption edges). [4]

For energies up to 50 keV, photoelectric absorption is very important in the study of soft tissues. The photoelectric effect can be used to improve image contrast by amplifying differences between tissues with slightly different atomic numbers. In mammography, this differential absorption is used choosing the target material and filters of the X-ray tube to shape the spectrum. The energy that optimizes the contrast is monoenergetic radiation between 15 and 25 keV, thus, molybdenum or rhodium can be used as anode material. The filter is made of the same material as the anode to reduce the lower and higher energies of the respective k-edges. [4]

1.2 X-ray Production

X-ray production can be made with a device that produces high energy electrons and induces their interaction with matter. The electrons are accelerated and when they interact with matter, their kinetic energy is converted into electromagnetic radiation. This can be achieved using, for example, an X-ray tube or a cyclotron. [4] An X-ray tube was used in the work described in this thesis and, therefore, its components and working principle will be described.

1.2.1 X-ray Tube

Essentially, an X-ray tube, shown in Figure 1.6, is composed by a vacuum chamber, a tungsten filament (cathode), a target (anode) and an X-ray transparent window, since the chamber is shielded to radiation. [4, 7]

By heating the filament (cathode) to approximately 2400 K, electrons are released from the filament by thermionic emission. The free electrons are accelerated towards the anode, by applying to it a positive voltage relative to the cathode [3, 4, 7].

The current applied to the filament determines its temperature and, hence, the rate of thermionic emission. If there is no voltage between the cathode and anode, the released electrons stay near the filament forming an electron cloud, also named space charge cloud. When a voltage is applied, the electrons flow towards the target, producing a current, in which the applied voltage determines the kinetic energy reached by the electrons. The space charge cloud creates a shield to the electric field (for applied voltages up to 40 kVp) and only a fraction of the released electrons flow to the anode, being limited by the space charge effect. Above 40 kVp the tube current is limited by the liberation of electrons from the filament. The tube current increases for higher applied voltages using the same filament current. However, above a specific kVp, there is a saturation and the increase of kVp does not increase significantly the tube current. [4]

The anode is a metal with a positive applied potential relative to the cathode. Most of the electrons' energy is converted in heat and only a small fraction emitted as X-rays [3, 4].

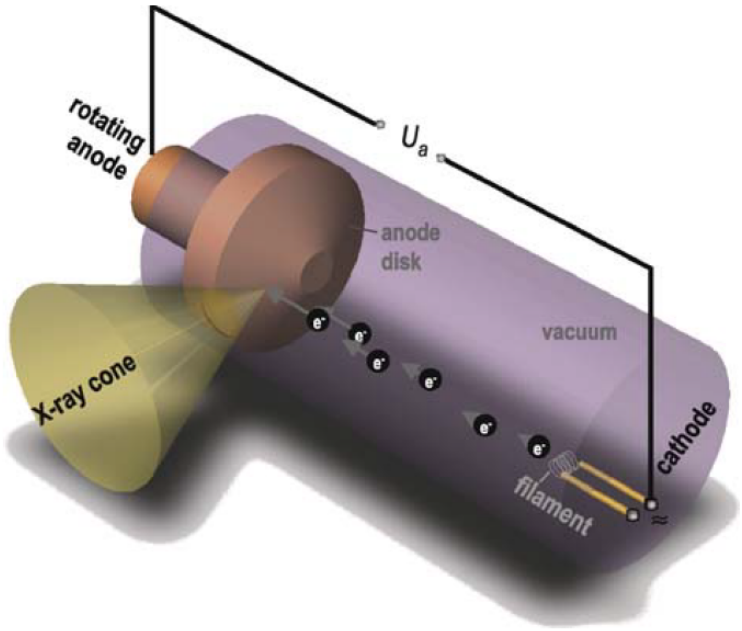

Figure 1.6: X-ray tube sketch showing the electrons released from the cathode being accelerated towards the anode where they are decelerated and X-rays are produced [adapted from [3]].

Tungsten has a high melting point and high atomic number, which provides good resistance to the heating and a good X-ray production. Therefore, due to its characteristics, it is widely used as anode X-ray tube. For mammography, the useful X-ray energy range is lower than in other X-ray production applications (such as CT) and anode materials such as molybdenum or rhodium have to be used. [4]

The anode can be stationary or rotative. In stationary configuration, the anode material is inserted in a copper block that will dissipate the heat. Rotative anode is more complex and consists on the rotation of the metal target during operation. This allows the X-ray tube to have a more effective heat dissipation, due to the higher area where the electrons impinge and, consequently, a greater X-ray flux is possible. This configuration also increases the anode useful life time. Typically, the target disk is supported by a rotor of a motor inside the chamber and can achieve 3000 to 10000 revolutions per minute. [4]

1.2.1.1 X-ray Spectra

A typical X-ray spectrum, produced by an X-ray tube, is shown in Figure 1.7. [3, 4, 7]

When an accelerated electron approaches the positively charged nucleus, the Coulombic forces decelerate it, resulting in a loss of its kinetic energy. The lost kinetic energy is converted in an X-ray photon with the same energy. This is called the bremsstrahlung radiation (Figure 1.7 (a) and (c)). [3–5, 7, 10] The distance between the incident electron and the atomic

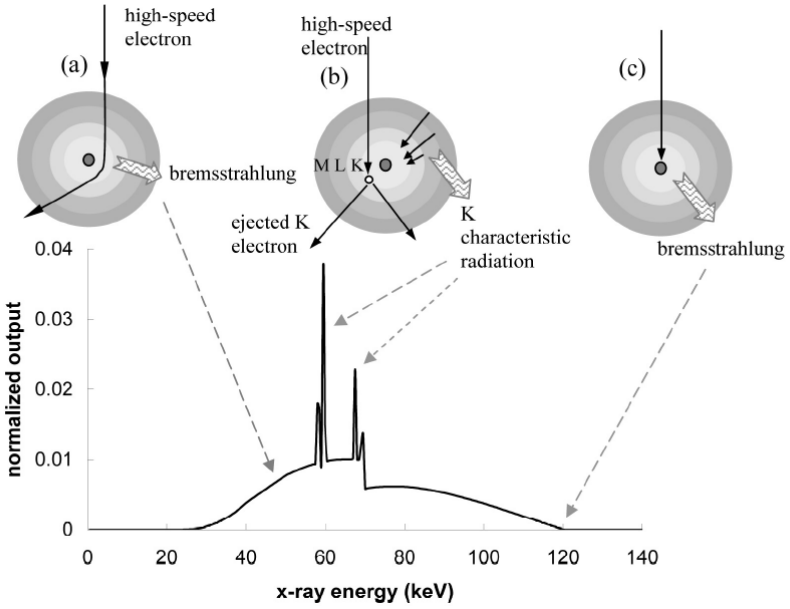

Figure 1.7: Typical X-ray spectrum of an X-ray tube showing the interactions of the incident electrons with the tungsten target and the removal of low energy photons due to additional filtration [adapted from [1]].

nucleus determines the electron energy loss: the Coulombic force is inversely proportional to the square of the distance. In this way, for interactions close to the atomic nucleus, high energy X-rays are produced (Figure 1.7 (c)), while for higher distances to the nucleus, lower energy X-rays are produced. If the electron impinges directly on the nucleus, the generated X-rays have the maximum possible energy (Figure 1.7 (c)). [3, 4] These interactions originate a continuous X-ray spectrum, as shown in Figure 1.7. [3–5, 10]

To the continuous spectrum, characteristic components are added, generated by the interaction of the incident electrons with the inner shell electrons of the target. In this interaction an electron of the inner shells is ejected and the atom becomes ionized. Then, an electron of the outer shells fills the vacancy and an X-ray photon (with energy corresponding to the difference of the binding energies) is emitted. Since binding energies are characteristic of each element, the generated X-rays are characteristic of the target material and originate sharp and discrete lines in the X-ray spectrum (Figure 1.7). [3–5, 7, 10]

Since the lower X-ray energies, usually, are not useful for X-ray imaging and just increase the exposure dose, a filtration (i.e the removal of X-rays by absorption when passing through a certain material) is performed. Usually the X-ray tube window has a flat metal filter with a few millimetres attached, to filtrate the low energy X-rays. [3, 4, 7]

1.3 Computed Tomography

The first concept of CT emerged in the 1920s with tomosynthesis. The word tomography derives from two Greek words: "tomos" (section) and "graphein" (to write), referring to a technique used to obtain images of a single slice eliminating the structures of other planes. This definition illustrates the overcoming of the limitations of conventional radiography: non-superposition of structures of other planes leading to a reduction of spatial information and consequently reduction in image low-contrast resolution. [3, 1]

1.3.1 Evolution of Computed Tomography

CT has evolved significantly since its first concept until the CT known today. Some stages can be considered: tomosynthesis, rotation-translation of a pencil-beam, rotation-translation of a narrow fan beam, rotation of a wide aperture fan beam, Fan Beam Rotation - Fixed Detector Ring, electron beam CT, helical CT, rotation in cone-beam geometry and micro-CT. [3, 1]

The classification of CT generations is not generalized and depends on the author. Hence, here a more descriptive option was preferred to explain the different CT evolution stages.

1.3.1.1 Tomosynthesis

Tomosynthesis, also known as conventional CT, appears to overcome the superposition of structures and the consequent poor low-contrast resolution. It is a radiography of a body section. [3, 1]

Conventional tomography was first developed by A. E. M. Bocage in 1921. [1] In this first concept, the image is acquired by moving, synchronously, the X-ray and detector linearly in opposite directions. In this way, only the structures in the plane of the rotation centre are well defined, while the structures above and below this plane are blurred; the higher the distance to the rotation centre plane the more blurred the structures appear. [3, 1] The focal plane is obtained by defining the distance between the X-ray focal point and detector proportional to their distances to the focal plane (Figure 1.8) . For different positions of the X-ray tube - detector system, points inside the focal plane are superimposed in the detector, contributing to an enhancement of the contrast, while points out of the focal plane are projected in different positions in the detector, thus reducing the contrast since they are distributed for a larger area. [1] This can be called "blurring tomography" and when digital post-processing of the projection images is applied, it is named "tomosynthesis". [3, 1]

Since the information above and below the centre of rotation plane is superimposed on the well defined image but it does not disappear, a significant reduction of image contrast is verified. However, compared to a conventional radiography a better image quality is achieved. With the increase of electronic X-ray detectors availability, tomosynthesis is becoming again in use since the images are stored digitally which allows the posterior image reconstruction

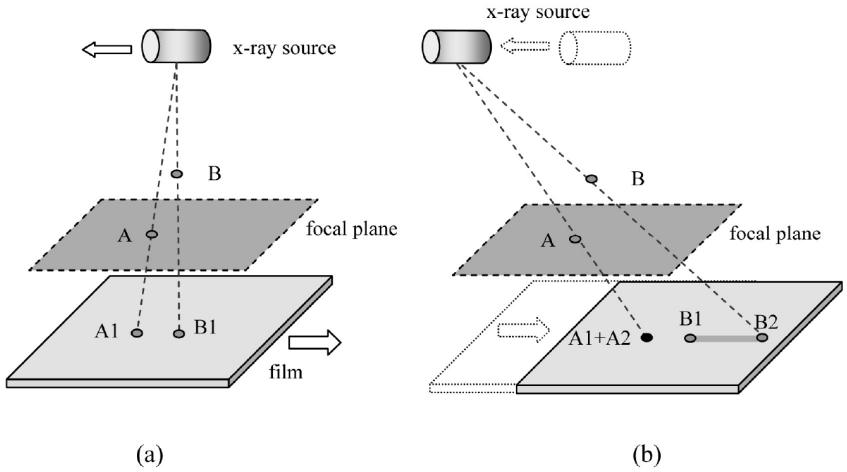

Figure 1.8: Conventional tomography principle [adapted from [1]].

getting an image quality better than the analog acquisition. [3, 1]

Nowadays, orthopantomography, an application of tomosynthesis, is widespread in dental care. It allows acquiring a panoramic view of the teeth rows of a curved image plane (according to the jaw curvature). [3]

The term "tomography" is also referring to other imaging modalities as MRI or Positron Emission Tomography (PET), but it is most commonly associated with CT. [3]

1.3.1.2 Rotation - Translation of a Pencil Beam

The first concept of CT evolved to its first stage based on a very thin X-ray beam collimated from a fan beam using a pin-hole collimator. The X-ray beam is 3 mm wide and 13 mm long and the detection is made with a single detector. To cover all the measuring field, the X-ray tube and detector are moved synchronously, with a linear translation. This linear displacement is repeated for each view (projection image in each angular position of the object). At the end of each scan field the X-ray tube and detector are rotated 1° to perform the acquisition in another angular position (Figure 1.9). [3, 4, 1, 7]

The intensity of the attenuated X-ray beam is measured by the detector and digitally stored. For each angular position of the object relatively to the X-ray tube - detector, a view is stored. In order to determine the distribution of the tissue attenuation coefficients, the object is imaged through 180°, since it is not possible to calculate the attenuation coefficients from only one view. [3] The first clinical CT scanner was built in 1972 in *Electric and Musical Industries Ltd* by Godfrey N. Hounsfield. Godfrey N. Hounsfield and Allen M. Cormack won the Medicine Nobel Prize in 1979 for their pioneering work in CT. [3, 1] The first 2D reconstruction took 9 days. Although this is an unacceptable time for clinical practice, for the first time a 2D image was obtained without averaging or blurring information. [3, 1]

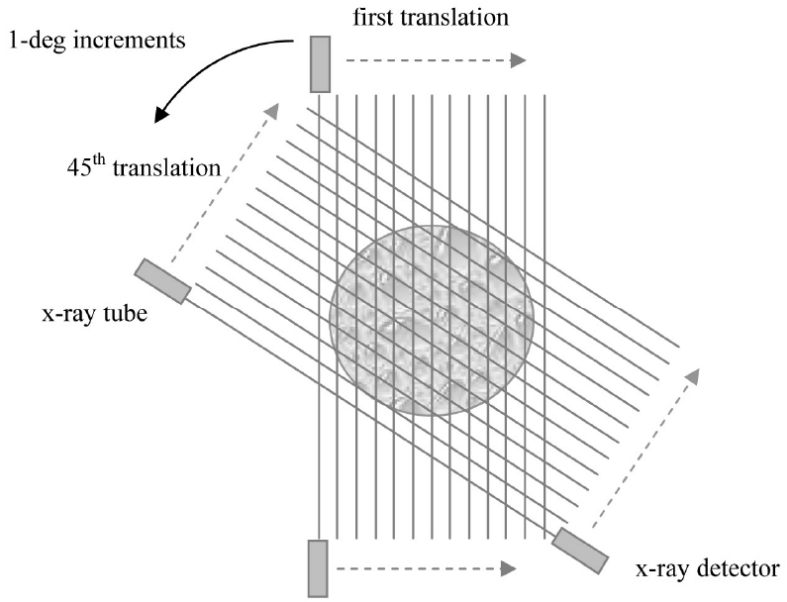

Figure 1.9: First CT system with a pencil beam and detection element. It measures one integral line at any instant, being translated to cover all the object and then rotated 1° to a acquire a new projection image. [adapted from [1]]

Concerning the rejection of scattered radiation, this geometry was the best: since it had only one detector, scattered radiation was practically not measured [4].

The image reconstruction is a very complex mathematical process and Johann Radon's method from 1917 was the only one available for half a century, but a practical solution was only possible with the computer advent. The mathematical processes used for modern CT geometries are based on the method implemented for pencil-beam. [3, 1]

1.3.1.3 Rotation - Translation of a Narrow Fan Beam

The next generation of CT has a narrow X-ray fan beam and a detector array (small when compared with the most recent). Although the X-ray beam has a wider aperture (about 10°) it is still small and a linear translation of X-ray tube and detector array is still needed. In this way, the X-ray tube and detector array are linearly translated to image all the measuring field and then rotated for a new projection, as shown in Figure 1.10. [3, 1, 4, 7]

Since the CT scanner has a wider X-ray beam and a small detector array, the acquisition time was reduced to a few minutes per slice, but the measuring field was still small. For this reason, these scanners were only used to acquire head images. In this way, taking into account the high acquisition times, the head could be fixed on a proper support inside the gantry eliminating the possibility of movements during acquisition time. In case of thorax and abdomen, their intrinsic movements would not allow acquiring images without motion artefacts in these conditions, even if the measuring field was large enough. [3]

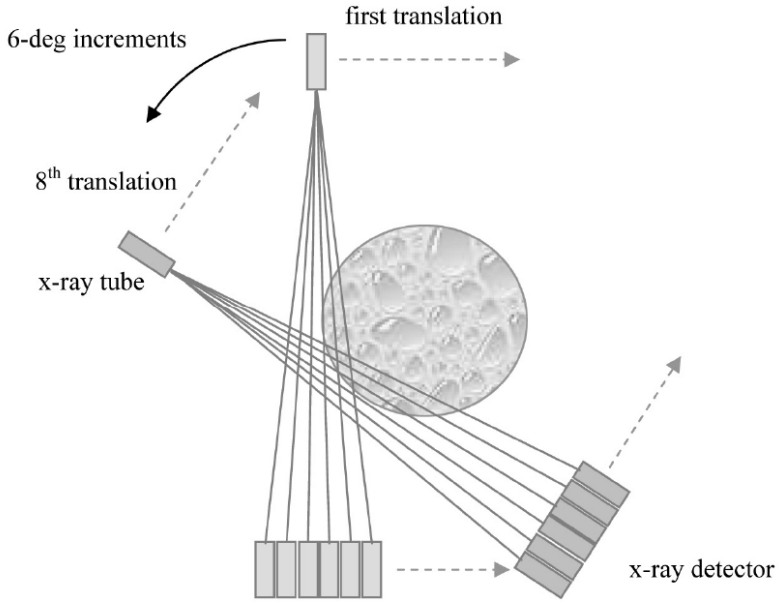

Figure 1.10: CT system with a narrow fan beam and a small detector array performing rotation after translation of X-ray tube and detector system [adapted from [1]].

The subsequent development of CT scanners took into account the goals of reducing acquisition time, X-ray exposure and cost. [3]

1.3.1.4 Rotation of a Fan Beam and Detector Array

The reduction of exposure and acquisition time was achieved using a large fan beam capable of imaging all the measuring field in each angular position. An acquisition time of 20 s was intended to image the abdomen with breath hold of the patient, reducing the motion artefacts. Using a wider X-ray beam, a longer detector array is also needed. Therefore, an arc of detectors was placed concentrically to the X-ray source (Figure 1.11). [3, 1, 4, 7] Nowadays the fan beam has an angle between 40° and 60° and the detector array has usually 400 to 1000 elements [3, 4]. Due to this implementation (higher number of detector elements) the cost of these scanners increased substantially [4]. In this configuration, the entire measuring field, including an area large enough for the torso, is imaged without the need to linearly translate the X-ray tube and detector array, with the system (X-ray tube and detector) being constantly rotated. Therefore, the acquisition time reduced significantly. [3, 1]

The majority of CT scanners used nowadays have this configuration. A common problem of this CT generation is the "ring artefact" caused by a defective single picture element (pixel) of the detector array. Only one poorly functioning pixel (defective or incorrectly calibrated) can cause an image artefact similar to a ring because that detection element corresponds to an angular distance from the rotation centre. In the next generation of CT scanners this kind of artefact was completely removed. [3, 4]

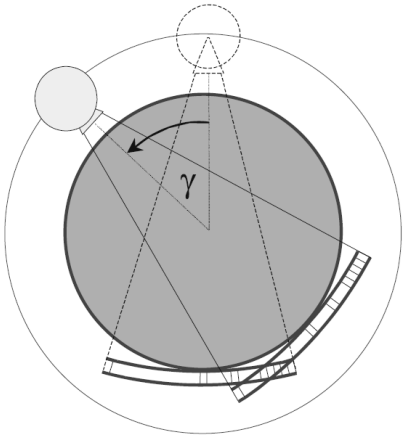

Figure 1.11: CT system with a fan beam and detector arc rotating constantly (without translation) [adapted from [3]].

1.3.1.5 Fan Beam Rotation - Fixed Detector Ring

In this generation, the X-ray tube still has a wide aperture and rotates continuously, however the detector array was replaced by a fixed full detector ring (360°), as shown in Figure 1.12, with about 5000 single elements that overcome the ring artifact. This is due to the fact that in this configuration the fan is inverted (the fan is centred in the detector element instead of on the X-ray tube), for which it can also be named detector fan. [3, 1, 4, 7]

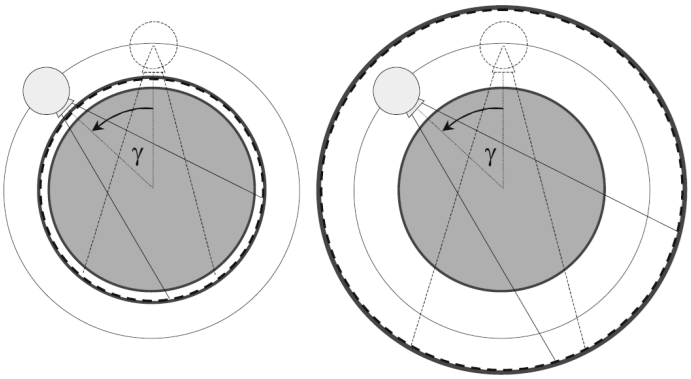

Figure 1.12: CT system with a detector ring. The X-ray tube can rotate outside or inside the detector ring [adapted from [3]].

The X-ray tube can rotate inside or outside of the detector ring. In case of being outside, the detector elements are dynamically tilted from the X-ray tube path in order to prevent the irradiation of the patient through the detector ring and its electronics. [3] Otherwise, if the X-ray tube is inside the detector ring the entrance skin dose is higher, and for this reason, usually it is preferred to have the X-ray beam outside the detector ring.

1.3.1.6 Electron Beam CT

The Electron Beam CT is a new concept that reduces acquisition time. This is important for applications with a very reduced acquisition time requirement, such as cardiac imaging. In this configuration the X-rays are produced by carefully designed coils that focus an accelerated electron beam onto a wolfram target ring, instead of having an X-ray tube. [3, 1] The fan shape of the X-ray beam is obtained by the sweeping motion of the electron beam. The X-ray intensity is measured with a stationary detector ring, similarly to the previous generation. The components of this kind of system are shown in Figure 1.13 [3, 1]

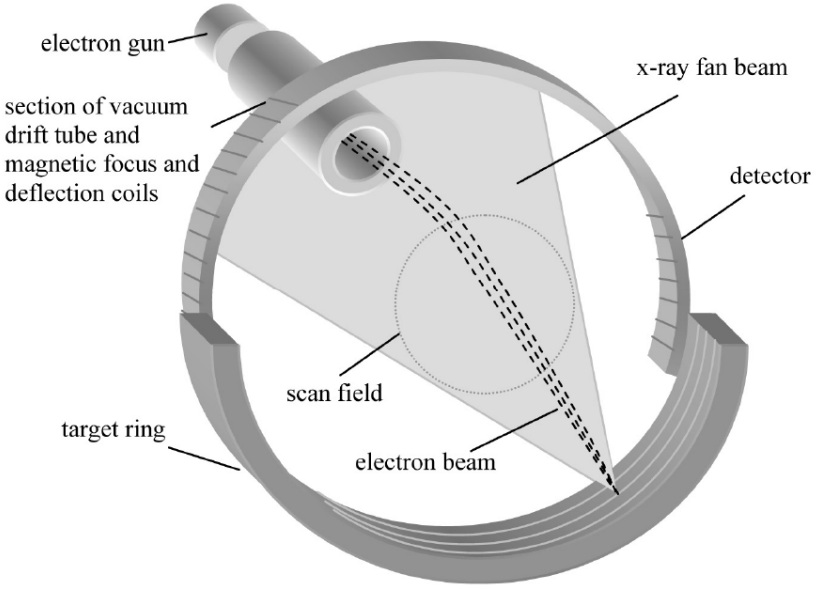

Figure 1.13: Electron Beam CT system showing its components - electron gun, focusing and deflection unit, target ring and detector [adapted from [1]].

The first Electron Beam CT was built between 1980 and 1984 [1]. For cardiac imaging, a complete set of measurements should be acquired within 20 to 50 ms which is achievable using this technology. [3, 1, 4]

1.3.1.7 Helical CT

In the previous configurations, the rotation of the X-ray tube was limited by the electric cables. At the end of each turn the cables were uncoiled by bringing the X-ray tube and detector to the initial position. Although data acquisition could be performed in both directions of rotation, the velocity of the X-ray tube - detector system was limited, making the reduction of acquisition time difficult. [3, 1, 4]

To overcome this limitation, the slip ring technology was introduced, making it possible to perform the intended turns without stopping. The sliding contacts allow the X-ray tube and detector array (in case of using a detector arc) to rotate continuously, becoming possible

two rotations per second. [3, 1, 4]

With the advent of slip ring technology, a new method of data acquisition, performed with the patient table moving continuously, became possible. In this way, the data is acquired in helical path, giving the name to the acquisition technique (Figure 1.14). The first prototype was developed in the middle of 1980s. [3]

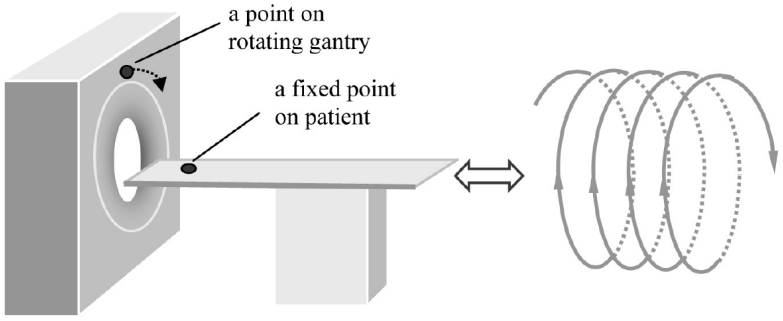

Figure 1.14: Helical scan geometry. X-ray tube and detector are rotating constantly and the table is moving forward until acquisition is complete, making a helical path [adapted from [1]].

1.3.1.8 Cone-Beam CT

The heat produced by the X-ray tube limits the using time. In order to use more effectively the X-ray production, an X-ray cone beam is used, taking advantage of which is already produced. The pencil, narrow and fan beams, described above, are produced using appropriate collimators, re-shaping the original X-ray beam and reducing the efficiency. [3]

This configuration implies the introduction of a flat panel, replacing the line or multi-line detector arrays (Figure 1.15). Another significant change is the high amount of data received in a short time that needs to be transferred to the data processing unit (image reconstruction computer), requiring a high bandwidth. [3, 7]

In this case, the image reconstruction is also different, requiring a more sophisticated mathematical method when compared to the previous CT generations. [3]

1.3.1.9 MicroCT

A microCT scanner represents a miniaturized CT scanner with specific application to small animal imaging, material testing and analysis. In human body it can be applied to the study of trabecular structures. [3]

MicroCT scanners can be completely shielded against primary and secondary X radiation having an entrance to insert the object or animal on a rotating support, which is controlled by a stepper motor. [3]

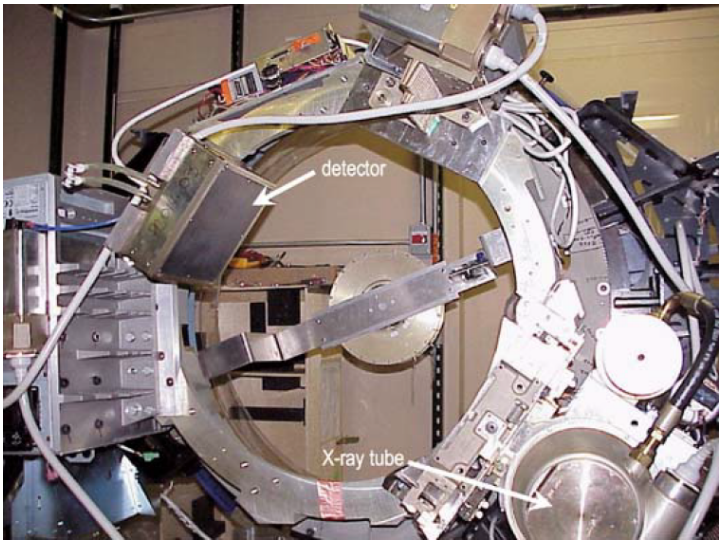

Figure 1.15: Cone Beam gantry showing the X-ray tube and flat panel detector [adapted from [3]].

The applications of this setup usually demand a very high spatial resolution. Therefore, there are two crucial elements in these systems: the X-ray tube and the detector. Since it is needed to achieve a spatial resolution at the µm scale, the focus size and the size of the detector elements are crucial, together with the mechanical alignment of the system. 10 µm is the desirable X-ray focus size and for this reason the current is usually less than 100 µA. The size of the detector element should be about 10 µm. These specifications allow achieving a spatial resolution of about 10 µm. [3]

Figure 1.16 shows two images of a tooth, in the left acquired with a MicroCT scanner and in the right with a clinical CT. The left image shows more details such as fissures that are not visible in the image obtained with the clinical scanner. [3]

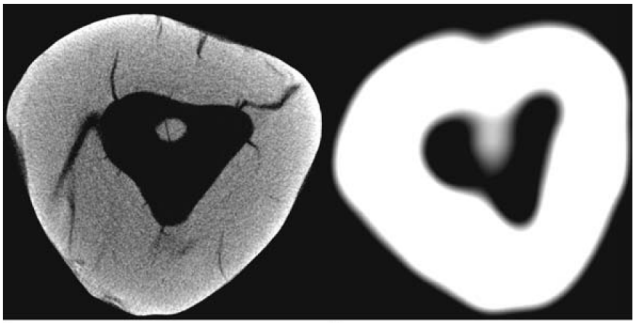

Figure 1.16: Tooth images acquired with a MicroCT (left) and a clinical scanner (right) [adapted from [3]].

The evolution of CT through all these years is obvious. Figure 1.17 shows two head

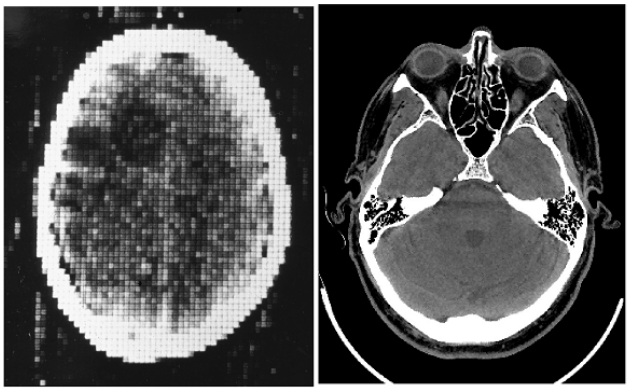

Figure 1.17: Two head images performed with the first CT scanner (left) and with a recent one (right) [adapted from [1]].

scans, at the left the first head scan and at the right an image that can be acquired with recent equipments. The image quality improved substantially since the first image, in terms of spatial and contrast image resolution. Also the acquisition time today is very short when compared with the first scans. [1]

1.3.2 Energy Resolving Detectors in Computed Tomography Systems

CT systems evolved significantly during time and the most significant evolutions were done essentially in the X-ray production and mechanical subsystems to optimize the dose. Nowadays, the production of X-rays in these systems is very stable and much more efficient than in the initial developments of CT and due to the restrictions in the dose, and consequently in the acquisition times, there is a limit in the signal-to-noise ratio (SNR). Therefore, strong efforts are now being done to improve the detector subsystems, providing more efficiency and more capabilities.

Gaseous detectors were the first used in CT systems, primarily by applying a Geiger-Müller counter in the first generations of CT scanners and in the scanner with rotation of a fanbeam and detector array, detector arrays of high pressure gas-filled chambers. Some are still used nowadays. [3, 11–14] This kind of detectors was replaced by solid state detectors with the improvement of CT scanners requiring a more rapid response, with ultra fast ceramic materials being installed [12–14].

Presently, almost all the clinical CT systems have scintillator detectors [3, 13]. Some materials are usual in this kind of detectors: caesium iodide, bismuth germanate, cadmium tungstate or ceramic materials such as gadolinium oxysulphide. However, detector technology is in constant evolution and recently spectroscopic detectors were introduced in some CT detection subsystems. Nowadays, single photon counting and energy discrimination, commonly used in single photon emission computed tomography (SPECT)/PET, is becoming available, and many tests indicate that it can provide other kinds of information. These detectors are

not yet completely developed for medical imaging use, notwithstanding, they can present a solution to make a more efficient use of the dose or to reduce it. [12]

In a conventional CT scanner, the X-ray flux is above $10^8 s^{-1} mm^{-2}$ using a source-to-detector distance (SDD) of 1 m and high power. The high X-ray flux in CT leads the detector to work in integrating mode, i.e., integrates all the deposited energy in the detector during the acquisition time. In this way, the information of the incident photons boils down to their accumulated energy. Counting single photons with this kind of X-ray flux is a challenge. In photon-counting detectors the count rates are in the order of $10^6 Hz\, mm^{-2}$, considering the pulse shaping and pulse height discrimination. For count rates such as the ones in medical imaging systems ($10^8 s^{-1} mm^{-2}$) ultra fast electronics is needed for photon-counting operation. [8, 15, 16]

Some kind of differentiation between materials based on their energy-related attenuation characteristics is presently possible by using two X-ray sources with different applied voltages (and two detector arrays) or only one X-ray tube varying rapidly its X-ray tube voltage, usually named dual-energy CT. [17–20] In the scope of this work it matters only the CT systems that derive energy information using spectroscopic detectors. Thus, in the following sections, a revision of the CT systems providing some kind of photon counting and/or energy information is done, classifying them according to their base detector. MPGDs, used in this work, are also a type of detectors that can work in single photon counting mode with energy resolving capabilities, and will be addressed in the next chapter.

1.3.2.1 Si Detector

One of the first CT systems with some kind of energy information used a silicon (Si) sensor layer with the Medipix1 chip. In this system, the X-ray tube and detector were fixed while the object was rotating. [8]

Medipix1 is a hybrid detector having 64×64 pixels with a size of $170 \times 170\, \mu m^2$ each and a Si conversion layer. This detector has photon counting capability and the possibility to define a threshold in which only photons with higher energy than this value are stored; and has a spatial resolution limited by its pixel size. [8, 21] Medipix1 was applied to CT acquisitions of a poly(methyl methacrylate) (PMMA) phantom (described in [8]) with different thresholds (11.5 keV, 16.5 keV and 23.6 keV) in order to evaluate the effect in the reconstructed image. Although a contrast reduction is verified, this system can distinguish structures with 0.2 mm. [8]

Figure 1.18 shows three images, one for each threshold. An image contrast reduction with the energy threshold increase is visible (from 2.0 to 1.47 between Teflon and PMMA and from -0.113 to -0.082 between Polyacrylamide and PMMA, for the 11.5 keV and 23.6 keV images, respectively). This shows the variation in the X-ray absorption with a different energy. The images with higher thresholds have also a reduced image quality due to the pixels with a very

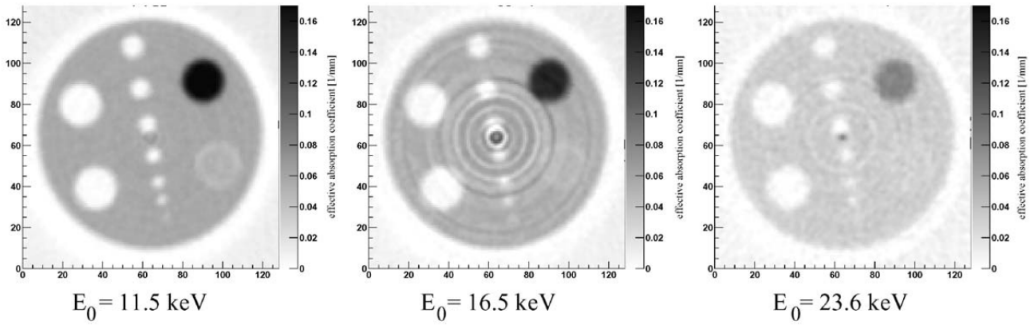

Figure 1.18: Each image corresponds to an acquisition with different energy threshold (E_0). The gray scale is similar for all the images, which allows verifying a contrast reduction as the energy threshold increases [8].

different response from the neighbour pixels and increased noise. [8]

Another solution using a Si detector was proposed by Xu et al. [16].

In this CT system, a 500 µm Si detector in edge-on configuration is used, taking advantage of the 30 mm detector, increasing the detection efficiency, essentially for higher energy photons. The pixel size is $0.4\times0.5\,\mathrm{mm}^2$. The detector has several readout strips to deal with the high X-ray flux of medical CT systems. An application specific integrated circuit (ASIC) processes the pulses and is able to count the photons using eight different energy thresholds. A pulse frequency of about 10 MHz is allowed, enabling an energy resolution of about 16.5% for 22 keV photons). [16, 22–25]

A 500 µm Si detector (Amptek XR-100CR) was also employed in the CT system developed in Ref. [26].

This system uses the Si detector with an energy resolution of 0.15 keV measured at the full width at half maximum (FWHM) of the 5.9 keV of ^{55}Fe emission [26, 27]. The projection images are obtained by translating and rotating the object, similarly to a first generation CT scanner. The source-to-object distance (SOD) is 1 m and the SDD 1045 mm using a 3 mm long collimator with 0.7 mm of diameter to reduce scattering. The X-ray tube has a focal size of 100 µm, the tube current and voltage were set to 0.4 mA and 52 keV, respectively. [26]

Images of iodine and cerium k-edges were obtained, using the photons beyond the k-edges energies. Acquisitions with different translation and rotation steps were performed, showing better spatial resolution when lower steps were applied. [26]

A charge-coupled device (CCD) based hyperspectral detector, the Color X-ray Camera, that determines the deposited energy in each pixel during a specific time, is also part of a CT system [28].

The detector, with a Si sensor layer of 450 µm, has a detection area of 264×264 pixels

with 48 µm^2 each, allowing a spatial resolution close to the sampling limit and an energy resolution of approximately 150 eV measured at the FWHM of the Mn kα. The count rate allowed by this system is limited to 8 Hz per pixel to keep the linear relationship between the input and output count rates. [28–30]

180 projection images with 20 min each, were acquired in a 360° range using a SDD of 900 mm and a tube voltage of 40 kV. A comparison between 3D integrating images and others obtained by subtracting images of energy ranges is done, showing the advantages and the applicability of a spectral detector in CT. [28]

1.3.2.2 MCP Detector

A CT system in a multislit multislice (MSMS) helical geometry using a microchannel plate (MCP) in an edge-on position was proposed by Shikhaliev et al., for breast imaging. MCP detectors have some interesting characteristics, such as photon counting and direct conversion capabilities, very good spatial and temporal resolutions and the possibility of eliminating noise. [31, 32]

A serpentine delay line is used to determine the interaction position, in which the total charge is divided and the time difference between the output pulses at each end of the delay line is proportional to the coordinate of the avalanche centre. This readout enables a spatial resolution of about 28 µm measured at FWHM and a threshold allows rejecting electronic noise. The drawback of the delay line is the count rate limitation to 2×10^5Hz for the entire field-of-view (FOV) due to the Analogue to Digital Converter (ADC) dead time (about 1 µs). [31, 33]

The CT system presented by Shikhaliev et al. provides the rotation of the detector, collimators and X-ray tube around the object. At the same time, the detector is shifted and tilted to cover all the FOV and focus with the X-ray beam, while the focal spot of the X-ray tube remains static (Figure 1.19). In this system, 750 pixels were used with a pixel size of 80 µm^2 covering 60 mm of FOV, however in some projections pixel sizes of 160 or 320 µm^2 were used. A SDD of 50 cm and a SOD of 45.5 cm was defined. [31, 33]

For CT acquisitions, 300 views per rotation (1.2° minimum step) with 1 s of acquisition time per view were acquired. As shown in Figure 1.20, CT images, with a slice thickness of 0.3 mm, of a PMMA phantom (described in [31]) were reconstructed using the filtered backprojection (FBP) with Shepp-Logan filter. [31] Images of a post-mortem rat were also acquired and can be seen in [31]. A spatial resolution of about 80 µm and 200 µm (FWHM) for 40 kVp and 90 kVp, respectively, can be achieved in this configuration.

The images in Figure 1.20 show a good image quality, and larger pixel sizes (160 µm and 320 µm) are also adequate for the aim of the study (breast imaging). [31] Therefore, MCP shows applicability in MSMS CT using photon counting capability also with good radiation scatter rejection, despite the limited count rate, that can be overcome with proper

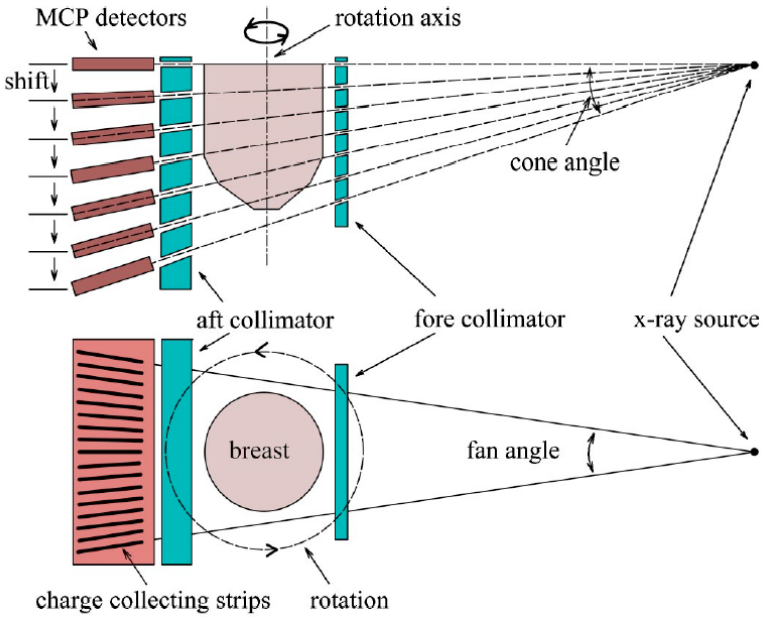

Figure 1.19: MSMS CT system with helical cone beam geometry and using detectors in edge-on configuration (top - front view; bottom - top view). Detector, collimators and X-ray tube rotate around the object. To acquire data in cone beam geometry, detector and collimators are shifted down, keeping the X-ray tube fixed [31].

modifications.

1.3.2.3 CZT Detector

Shikhaliev et al. proposed a CT system for breast imaging using a photon counting cadmium zinc telluride (CZT) detector, which allows high count rates (about 2×10^6Hz/pixel) and energy resolution between 4% and 10%, measured at the FWHM in the range of 20 to 120 keV. [34–36]

In CZT CT system, 8 modules of pixelated CZT crystals, each with $0.9 \times 0.9\,\mathrm{mm}^2$ pixel size and 1 mm pitch, with two pixel rows, were used. The active area is $2 \times 128\,\mathrm{mm}^2$. [34, 37]

A sketch of the system can be seen in Figure 1.21. The X-ray tube (with a fan beam) and detector are motionless and the object is rotated using a stepper motor, with the SDD being 860 mm and the SOD 760 mm. An adaptive filter to equalize the incident X-ray flux was used, to obtain a more uniform detector response and eliminate cupping artefact due to beam hardening. 230 views of a PMMA phantom (described in [34]) were acquired with 100 ms of acquisition time per view and the images were reconstructed using FBP with Shepp-Logan filter. [34]

The interacting photons are classified according to its energy in five different energy bins. This means that the energy of each single photon is not known, but depending on its amplitude, it is classified in a bin. The five bins are sufficient to achieve a contrast-to-noise

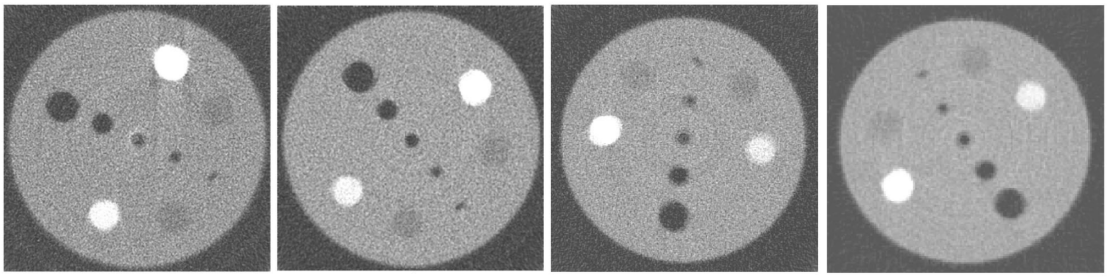

Figure 1.20: CT images from the PMMA phantom acquired with MCP detector using different parameters. From left to right: first and second images acquired with 50 kVp and 80 kVp, respectively, using a pixel size of 80 µm; third and fourth images acquired using 80 kVp but with different pixel sizes, 160 µm and 320 µm, respectively. [31]

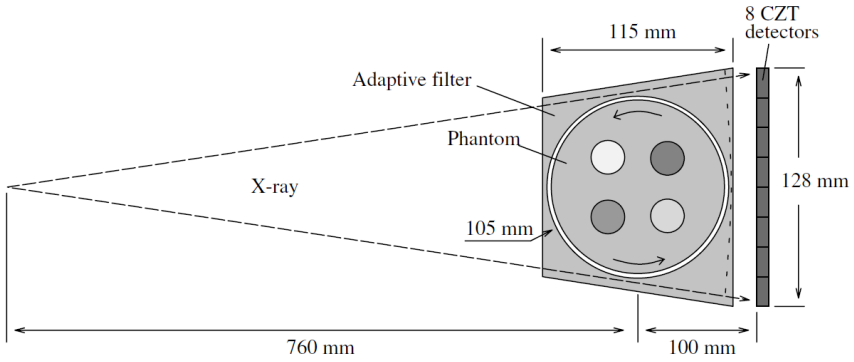

Figure 1.21: Sketch of the CT system used to Shikhaliev et al., showing the main components: X-ray fan beam, adaptative filter, phantom and detector [34].

ratio (CNR) improvement, as shown in section 2.4.4, with the energy weighting technique (EWT) being applied using a weighting factor calculated for the average energies. [34]

Figure 1.22 shows integrating and EWT images which reveal a contrast improvement, analysed in the line profile marked on Figure 1.22. A CNR improvement of 1.40 was achieved from the integrating to the EWT image in the $CaCO_3$ region. The image CNR was improved in iodine and wax by 1.63 and 1.13 factors, respectively. [34]

Shikhaliev et al. also performed weighting in energy and then image subtraction (low and high energies) of the projections (before reconstructing the CT image). The CNR was also improved by a factor of 1.57 and 1.46 in $CaCO_3$ and iodine regions, respectively (between integrating and EWT images). [34]

Another CT system also presented by Shikhaliev et al. with a CZT detector was developed for breast imaging and compared with a commercial conventional scanner (Siemens Sensation 16). [38] A CZT detector with 2×256 pixels each with a size of 1 mm^2, covers an area

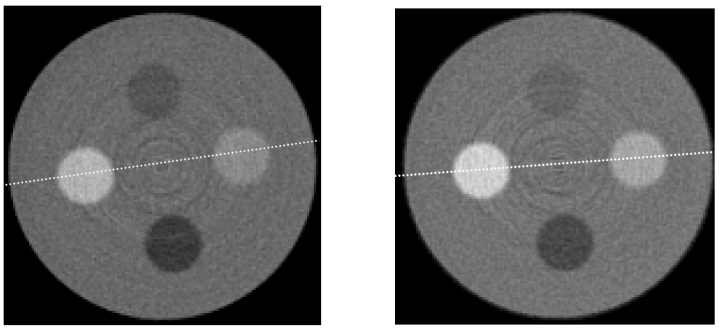

Figure 1.22: Integrating (left) and EWT (right) CT images obtained with the system proposed by Shikhaliev et al. using a CZT detector [34].

of $2\times25.6\,cm^2$. This detector represents an extension of the previous detector. [34, 38, 37] A count rate of 30×10^3Hz/pixel was used, however, the detector allows 2×10^6Hz/pixel. Similarly to the previous system, 5 energy bins are available to classify the incident photons according to their energy. [38]

This system includes a stationary gantry with a SDD and a SOD of 85 cm and 53 cm, respectively, allowing a magnification factor of 1.61. A FOV of 15.9 cm can be used. Like in the previous system, an adaptive filter was used. The objects were rotated using a stepper motor that allows acquiring up to 5000 views in 360°. For CT acquisitions, a 360° scan of 800 views with 50 ms each of the PMMA phantoms (described in [38]) was acquired. [38]

Energy resolutions of 25% and 17% for 59.6 keV and 122 keV (measured at the FWHM) are achieved and taking advantage of the magnification, this system provides a spatial resolution of about 0.63 mm (measured at the FWHM). Different types of images were reconstructed, such as multi-energy, photon counting, EWT and material decomposed images. Figure 1.23 shows an example of material decomposed images, in which some based materials are removed, which shows good image quality, the advantages and the applicability of the system in CT. [38] Other images can be seen in ref [38] such as the results of the comparison of the two systems, that revealed comparable performances.

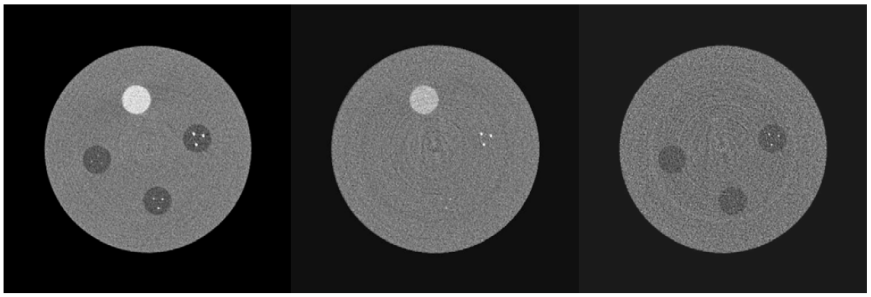

Figure 1.23: CT image of the resolution phantom (left), tissue canceled image (centre) and $CaCO_3$ image (right) [38].

1.3.2.4 CdTe Detector

A pre-clinical CT system providing energy information of the incident photons using a cadmium telluride (CdTe) detector was proposed by Schlomka et al. [15]. The detector consists of a single-line CdTe array with 1024 pixels, with an active area of 0.38 mm × 1.6 mm each. Six energy bins, with adjustable thresholds, are available to classify the incident photons, according to its energy. It allows a count rate of about 3×10^5Hz/pixel, without significant pile-up, a spatial resolution of approximately 250 µm and an energy resolution of about 20% for 25 keV (FWHM). [15]

This system, shown in Figure 1.24, uses a rotating gantry, rotated by a motor synchronized with the PC-based data acquisition. The SDD and SOD were set to 600 mm and 300 mm, respectively, allowing a magnification factor of about 2. A FOV of 200 mm can be used. [15]

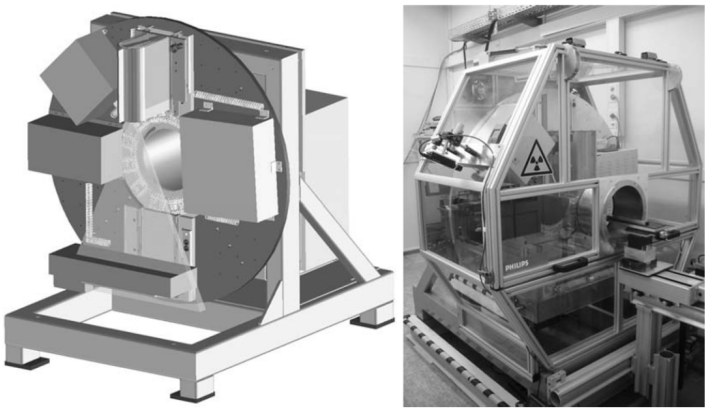

Figure 1.24: Sketch (left) and picture (right) of the CT system proposed by Schlomka et al. [15].

For CT acquisitions, 450 projection images of a PMMA phantom (described in [15]) were acquired with an acquisition time per image of 250 ms. Image reconstruction using energy ranges (Figure 1.25) and material decomposition images (Figure 1.26) was performed. [15]

Iodine contrasts and Calcium-hydroxyapatite show higher attenuation in lower energy bin images, which decreases for higher energy bin images. On the other hand, gadolinium attenuation increases as the energy increases. The images show only slight differences between water and PMMA, due to their similar atomic number. [15]

Images of iodine-based and gadolinium-based materials could be reconstructed, showing good material decomposition and achieving concentration values in accordance with the expected values. [15]

This system was applied in preclinical studies to obtain images from a mouse, as described in Ref. [39], in a high resolution configuration achieving a spatial resolution of about 100 µm.

A system using also a CdTe detector is proposed in [40].

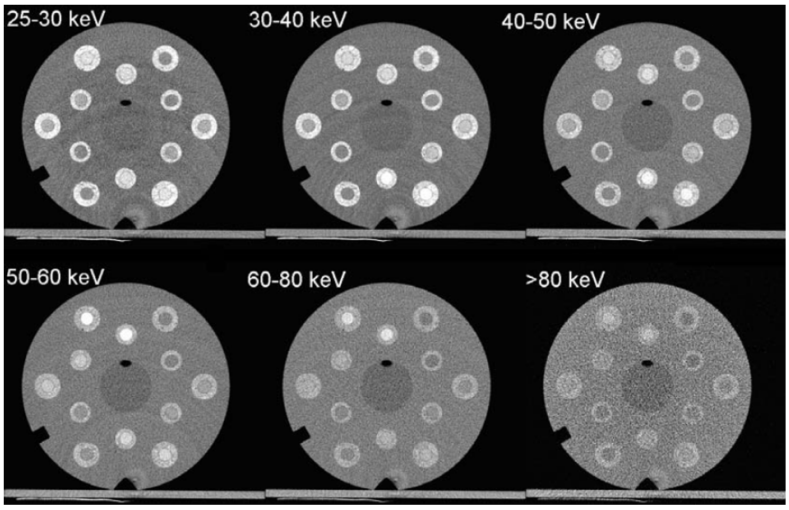

Figure 1.25: Cross-sectional images reconstructed using the energy bins applied for data acquisition [15].

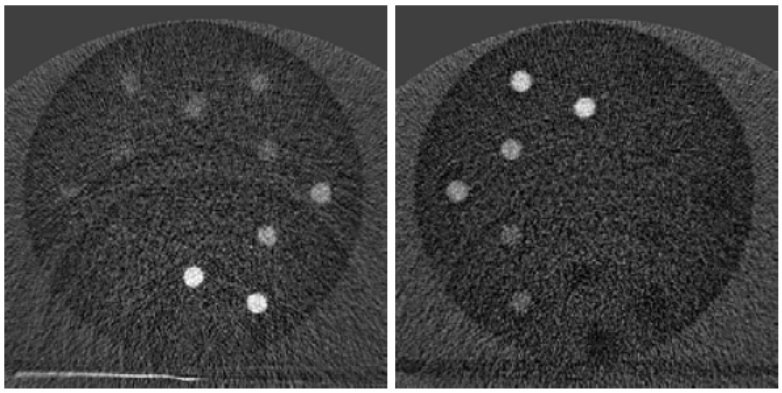

Figure 1.26: Images of material decomposition showing the iodine (left) and gadolinium-based (right) materials decomposed in two different images [15].

The detector, with 64 pixels, each with a size of $1\times0.5\,\mathrm{mm}^2$, is able to count the number of photons above a specific threshold and five different energy thresholds are used. An energy resolution of 10 keV at 122 keV (^{57}Co) measured at the FWHM is registered and it allows a count rate of 2×10^6Hz/pixel. [40]

SDD and SOD are 577.5 mm and 462.5 mm, respectively, allowing a magnification factor of approximately 1.2. For CT acquisitions, 90 projection images of PMMA phantoms (described in [40]) over 360° were acquired. Figure 1.27 shows CT images reconstructed with different energy ranges, clearly showing a reduction of the beam hardening effect for higher energy window images. [40] Photon counting images were also reconstructed and can be seen in [40].

A CdTe detector for a GE Light Speed VCT scanner ([41]) was also developed in [42, 43]. A single detector array has 16×16 pixels with a pitch of 1 mm. An energy resolution of

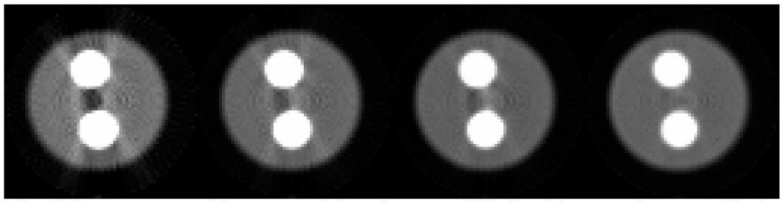

Figure 1.27: CT images of the phantom with water and iodinated water in the holes reconstructed with different energy ranges. From left to right: 30-39 keV; 40-49 keV; 50-59 keV and 60-69 keV [40].

4.75% (FWHM) was measured with ^{57}Co (122 keV). In the CT system, two detector arrays were used and a count rate of about 3×10^6Hz can be used. [42]

Cross-sectional images reconstructed with different energy bins can be seen in Figure 1.28, showing the intensity dependence of the iodinated left internal carotid with the energy. [42]

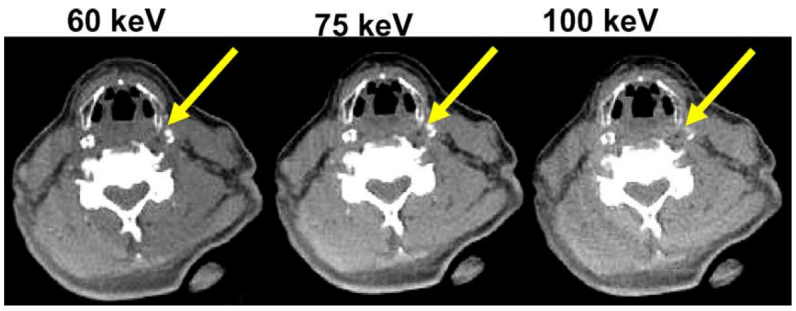

Figure 1.28: CT images acquired at the neck level reconstructed with different energy bins: 60 keV; 75 keV and 100 keV [42, 43].

1.3.2.5 Yttrium and gadolinium oxysulfide Detector

Philips developed a new CT scanner, the IQon Spectral CT, with a spectroscopic detector. [44–47]

The system is composed by two sensor layers, the first, a NanoPanel Prism detector, based on a Yttrium-based scintillator that does not absorb high energy photons; and the second layer, made of gadolinium oxysulfide, that absorbs high energy photons (99.5%). [47]

The detection of the energy levels of the incoming photons provides information of the tissue composition and allows its characterization. Quantification of calcium content and kidney stones and characterization of plaques is possible with this system. Besides, the reconstruction of an integrating (conventional) image is also possible. [44, 45, 47]

As a result the cross-sectional image can be displayed in a gray scale for anatomical information and in colour scale for the visible anatomy composition, as can be seen in Figure

1.29 [47].

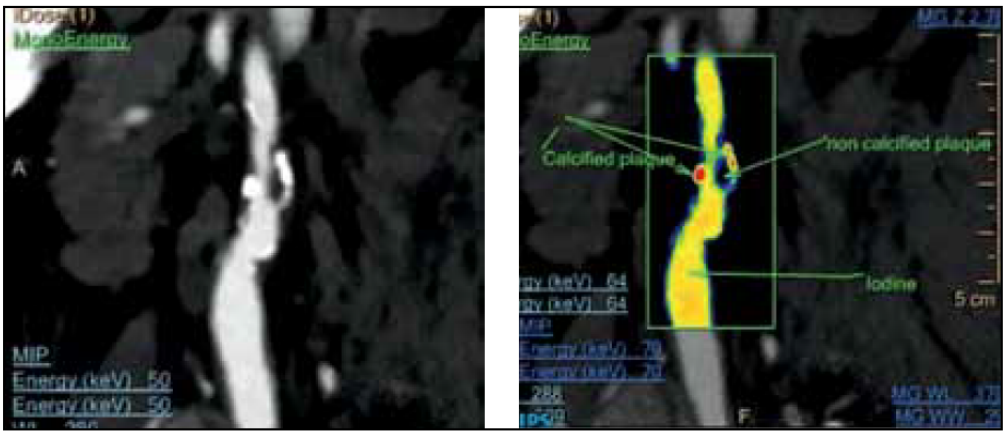

Figure 1.29: Integrating cross-sectional image of the carotid (left) and image showing also the spectral information (right), in which calcified (red) and non-calcified (black) plaques can be identified [47].

Detectors with spectroscopic capabilities are the next generation of commercial CT scanners, being nowadays a field in continuous development, to improve the performance of CT scanners. The possibilities opened by using this kind of detector are wide and present several advantages. The image quality can be improved even reducing the administrated dose.

A direct comparison between a spectral CT and a commercial CT scanner from Siemens ([38]) show that both can have a similar performance, however the energy information can be applied to get further images (with different informations) and CNR improvement with a single scan. The information of each photon energy allows the reconstruction of images using only part of the energy spectrum, which can show different map intensities and enhance different structures. It was also shown that images obtained by energy subtraction are possible and can enhance specific structures. The application of an adequate energy weighting factor allows improving CNR and/or reducing the dose up to a factor of 2.5. Counting images present already enhanced image quality, and on EWT images this improvement is maximized. Another possibility is the reconstruction of material decomposition images, in which images showing only base materials can be obtained, separating a specific base material in single images. Finally, in the IQon CT scanner, anatomical information can be joined with its composition, allowing tissue characterization.

As seen, solid state detectors are the main kind of detectors used for spectroscopic CT. These present an excellent spatial resolution, some in the order of dozens of µm and good

energy resolution. On the other hand, in the systems presented, the electronics included a dedicated readout for each pixel, which makes them substantially more expensive than a solution using resistive lines applied in the MPGDs, addressed in the next chapter, which also allows achieving a good energy resolution and a spatial resolution in the order of the hundreds of µm. MCP was an exception, using delay lines that allow counting the number of photons above a certain threshold, however it does not give the energy information of the incident photons.

CHAPTER

2

GASEOUS DETECTORS

The oldest radiation detectors are based on the interactions of charged particles with a gas medium. Several aspects concerning gaseous detectors, such as physical interactions of the radiation with the gas medium, types of detectors, general properties or working modes, will be referred to in the following subsections. [5, 48]

2.1 Basic Principles

In a simplified concept, a gaseous detector consists of a chamber with two electrodes inside and a gas medium. The majority of gaseous detectors senses an ionization created by the incident radiation, generating electron-ion pairs where the cations are attracted to the negative electrode and the electrons to the positive electrode (Figure 2.1), originating an electronic output signal. [4, 5, 49, 50]

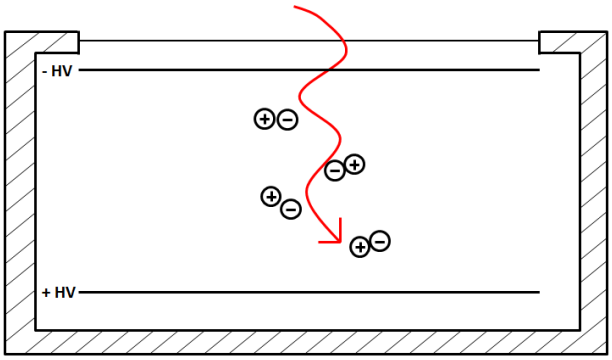

Figure 2.1: Sketch of a simplified concept of a gaseous detector.

Independently from the type of process that originates the electron-ion pair, the important information is the total number of pairs originated along the track of the radiation. [5, 49, 50]

For an ionization to occur, the radiation must transfer at least the amount of energy equal to the ionization energy of the gas molecule. However, the incident radiation can lose energy without ionizing the gas molecule, for example, through the process of excitation. In this way, the average energy lost by the incident radiation per electron-ion pair formed is greater than the ionization energy. The average energy lost by the incident radiation per ion pair is named W-value and depends on the gas medium, radiation type and energy. The typical values of W-value for noble gases vary between 22 eV for Xe and 46 eV for He. [5, 49, 50]

For a certain incident radiation energy, the number of created electron-ion pairs would ideally be exactly the same if all the energy was used to create electron-ion pairs, for the same quantity of energy required to form an electron-ion pair. However, some statistical fluctuations are observed in the number of electron-ion pairs created. These fluctuations limit the maximum energy resolution achieved by any detector based on the collection of electron-ion pairs. The formation of each electron-ion pair is considered a Poisson process,

therefore it is characterized by a standard deviation, σ, proportional to the square root of the average number of electron-ion pairs formed, N [5, 50]:

$$\sigma \propto \sqrt{N} \tag{2.1}$$

2.1.1 Diffusion, Charge transfer and Recombination

The mean free path of the gas atoms or molecules for typical gases under standard conditions is about $10^{-6} - 10^{-8}$ m. During the movement of the charge carriers, several types of collisions can occur: charge transfer, electron attachment, recombination or diffusion, as represented in Figure 2.2. [5, 49, 50]

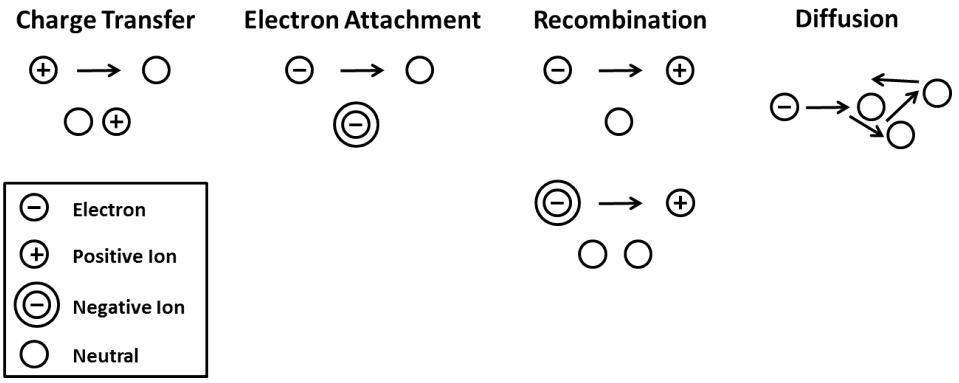

Figure 2.2: Possible collisions during the ion pair movement.

Charge transfer collision may occur when a positive ion meets a neutral molecule and an electron is transferred to the positive ion. In this way the molecule becomes a positive ion and the ion becomes neutral. [5]

The attachment consists of electron capture by a neutral molecule during its diffusion. Then, a negative ion with properties similar to a positive ion (with opposite charge) is formed. Oxygen has a high attachment coefficient in which free electrons are readily attached and converted into negative ions. On the other hand noble gases have a relatively low electron attachment which means that free electrons can migrate easily in these gases, opposite to what occurs in Oxygen. [5, 49]

Recombination can also occur as a result of a collision between a positive ion and a free electron or a negative ion. In the first case, the electron is captured by the positive ion and becomes a neutral molecule; in the second case, the electron (conferring the negative charge) is transferred to the positive ion creating a neutral molecule. In both cases the charge of the original pair is lost and is not added to the signal in detectors based on the collection of the ionization charge. [5]

2.1.2 Charge Migration

Charge separation and collection shall be as rapid as possible to minimize recombination. This can be accomplished by applying high electric fields. Applying an electrical field in a region with ions or electrons will make them migrating away from their point of origin. Concerning the drift movement, positive ions move in the direction of the electric field vector and electrons move in the opposite direction. The drift velocity, v, of ions in a gas medium can be determined using:

$$v = \frac{\mu * \xi}{p} \tag{2.2}$$

μ being the mobility, ξ the electric field strength and p the gas pressure values. μ tends to be constant over a wide range of electric field and gas pressure. Based on tabulated mobility values, the time that an ion takes to move a centimetre (for typical detector dimensions) is about 10 ms, which is a long time for most standards. [5, 50]

Free electrons have lower mass, therefore their drift velocity is much greater, and their mobility is typically 1000 times higher than that of ions. To collect electrons takes a time in the order of microseconds instead of milliseconds. The distance of diffusion during the few microseconds might be in the order of a millimetre, which is very important in position sensitive detectors, since it influences the achieved position resolution. In this kind of detectors, the position of interaction (of the incident radiation with the gas medium) is determined using the arrival position of the electrons at the detector anode or measuring the electron drift time. [5, 49, 50]

Irradiating a gas detector constantly, the rate of formed electron-ion pairs is constant and will be determined by the rate of electron-ion pairs lost by recombination, diffusion or migration in the gas. The drift of charges forms an electric current, and is an accurate measure of the created electron-ion pairs. Measuring this ionization current, collected at the electrodes, is the basic principle of many detectors. [5, 49]

As shown in Figure 2.3, increasing the electric field will increase the primary charge measured at the electrodes due to a more rapid separation of the electron-ion pairs, diminishing recombination and collecting all the charges created in the ionization. At this point, a higher applied voltage will not increase the current since all the produced charges are already measured. This is called the ion saturation. Reaching the saturation current can be influenced by some factors, such as recombination. Recombination is more significant for high rates of detector irradiation. With low incident radiation rate, the density of positive ions and electrons is low and the recombination rate is less significant than at high irradiation rates. [5, 50]

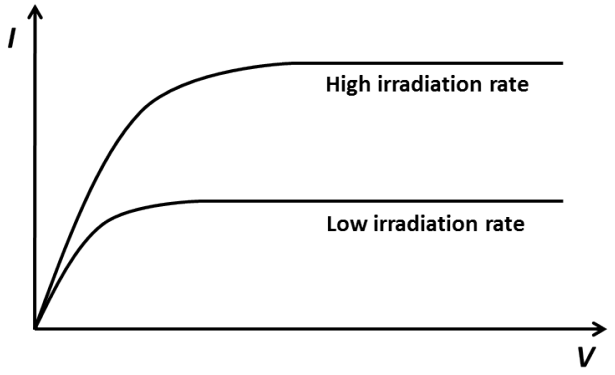

Figure 2.3: Primary charge current measured versus the applied voltage. Increasing the applied voltage reduces recombination and the collected charge increases until a saturation in which recombination is negligible and the total charge produced is measured. Therefore, increasing more the applied voltage does not increase the collected charge.

2.2 Avalanche Detectors

2.2.1 Gas multiplication and avalanche formation

Proportional counters can be used to detect low energy X-rays. Radiation with this energy produces photoelectrons with energies in the range of a few keV or less, and for the usual W-values, the corresponding charge is too low to be distinguished from the electronic noise, which means that gas amplification is needed to enhance the SNR of the measured pulses. [5]

Gas amplification is achieved inducing charge multiplication in the gas by applying a sufficiently high electric field within the detector. In these conditions, free electrons are accelerated, acquiring high kinetic energy, and colliding with other particles in the gas, instead of simply drifting to the electrodes as explained in Section 2.1.2. The higher the electric field, the higher the average energy of an electron between collisions. Secondary ionizations will occur only above a threshold value of the electric field. [5, 49, 50]

The secondary electron is also susceptible to the electric field, becoming also accelerated. During its path it suffers collisions with other neutral gas molecules, generating more ionizations. The released electron creates another ionization and so on where each free electron can generate more free electrons. Therefore a charge multiplication occurs in the form of a cascade, known as Townsend avalanche, whose equation describes the fractional increase in the number of electrons per unit path length [5, 49, 50]:

$$\frac{dn}{n} = \alpha dx \tag{2.3}$$

where α is the first Townsend coefficient for the gas medium, being zero when the electric

field is below the threshold and, above this point, increases for higher electric fields. In case of a parallel geometry, the electric field is spatially uniform and α becomes a constant (with the position) in Equation 2.3, and the density of free electrons grows exponentially with distance during the avalanche process [5, 50]:

$$n(x) = n(0)e^{\alpha x} \tag{2.4}$$

The collection of all free electrons in the respective electrode (anode) ends the avalanche and, using adequate conditions, the total charge collected is proportional to the number of primary electron-ion pairs generated in the interaction of the radiation with the gas medium. [5, 49, 50]

2.2.2 Regions of Detector Operation

The regime in which a gas counter is operating depends on the applied voltage to the detector that will define the electric field, as shown in Figure 2.4. In case of a very low electric field, recombination occurs and the collected charge is lower than that represented by the primary charge. By increasing the electric field in order to suppress recombination, the normal mode of operation of ionization chambers, ion saturation region, is achieved. Further increasing the applied voltage, and thus, the electric field, above the threshold value, will allow starting the gas multiplication process. In a specific electric field range, named proportionality region, the collected charge will be proportional to the primary charge, corresponding to the conventional proportional counters. For higher applied voltages, non-linear effects can be introduced, that may be related with the positive ions created in the secondary processes [4, 5, 49, 51, 50]. This situation will not be addressed since it is not of interest to this work. Further informations can be found in references [4, 5, 49, 51, 50].

2.2.3 Detector Geometry and Fill Gas

An uniform charge multiplication needs to be assured, to ensure a total charge proportional to the primary charge. Therefore, the detector should be designed properly in order to confine the charge multiplication to a small region, applying high electric fields in the electrodes vicinity. The electrons will be generated in the drift region, migrate to the multiplication region and suffer charge multiplication. This means that the electrons will be amplified for the same factor and independently from the interaction region. [5, 51]

After ionization, the produced photoeletron can travel in the gas before its interaction. Thus, the distance travelled will determine the place where the charge avalanche starts, which means that the place where the primary charge is collected can be shifted relative to the interaction position of the X-ray photon with the gas medium. Since the centre-of-gravity of the charge spatial distribution is usually used to determine the interaction position, this

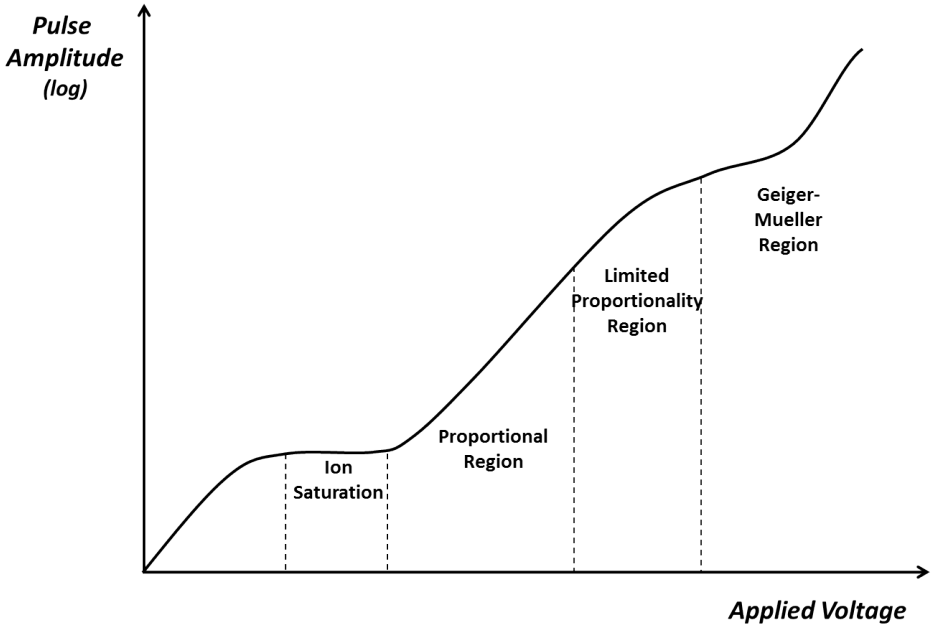

Figure 2.4: Pulse amplitude (in logarithm scale) versus the applied voltage to the detector, defining the operation regions.

can contribute to a degradation of the spatial resolution. Spatial resolution decreases as the photoelectron range increases. In addition, other physical processes can contribute to the spatial resolution degradation, such as Auger emission or the interaction of fluorescence photons within the detector volume. Furthermore, excitation can occur instead of secondary ionizations (not contributing for charge multiplication) and its de-excitation results in the emission of a visible or ultraviolet photon. The emitted photon can interact with less tightly bound electrons by photoelectric effect or produce electrons when interacting with the detector wall, leading to a loss of proportionality in the multiplication charge and/or spurious pulses. [48, 51, 52]

All these processes will spread the charge spatial distribution, limiting the position resolution. The photoelectron range can be reduced using heavier gases and, to prevent the other interactions, polyatomic gases are added to absorb the photons and stop further ionizations. This stabilizing additive is named quench gas. [5, 48, 49, 52, 50]

Adding a small amount of another gas to the principal component can change significantly the properties of the main filling gas, such as W-value, drift and diffusion characteristics. [5, 50]

Noble gases have adequate characteristics to be used as detection medium in ionization detectors. They are inert at normal temperature and pressure, require lower electric field for avalanche formation and can be easily purified. Also, and most importantly, they have a high stopping power and the ability to absorb nuclear radiation. For example, Xe has a

high atomic number (Z = 54), being excellent as radiation detection medium essentially in the energy range in which photoeletric effect predominates. [48, 53, 54, 50]

The gas container must be designed in such a way that the gas purity is maintained during time. In this way, the detectors can be sealed or work in a continuous gas flow. In a sealed detector, the fill gas can be purified using a purifier that removes oxygen and other electronegative impurities. In detectors working in a continuous gas flow, a gas supply and exhausting system is needed. In continuous gas flow mode, it is easier to keep the gas purity, and choose/change the filling gas. [5]

The detector window will also absorb some of the X-rays with low energies, thus it should be thin enough to transmit the maximum amount of X-rays possible and at the same time sufficiently resistant to support the pressure difference between the detector volume and external environment, as well as gas-tight and optically opaque (to prevent the emission of free electrons from the gas medium due to visible or ultraviolet radiation). [5]

2.3 Detector Characteristics

Radiation detectors, independently from the type, have common characteristics that will be described in the following subsections. It will be considered that the generated current flows at the same time of the charge collection and also that the incident radiation occurs at a sufficiently low rate to distinguish each interaction.

2.3.1 Detector Operation Modes

It is possible to distinguish three types of operation modes in detectors: current mode, pulse mode and mean square voltage (MSV) mode. These operation modes have a common dependence on the sequence of current pulses, being operationally distinct and usually used for different applications. [5, 51] During this work only the pulse operation mode was used and will be addressed. The other operation modes are explained in reference [5].

Pulse Mode

Pulse operation mode allows storing information about each radiation quantum that interacts with the detector. The total charge, Q, is determined calculating the time integral of each current signal. Since Q is proportional to the deposited energy in the detector, timing and energy of each radiation interaction is known. Once information of each quantum is available, this can be classified as radiation spectroscopy. [5, 51]

The circuit to which the detector is connected influences the obtained signal, and thus it is needed to take into account resistance and capacitance (of both the circuit and detector). This will define the time constant of the circuit, $\tau = RC$, that in turn will influence the signal voltage, $V(t)$. As shown in Figure 2.5 b), if τ is much smaller than the charge collection time

of the detector, $V(t)$ has a shape similar to the time dependence of the current because the current flows through R practically at the same time as it flows in the detector. A low τ is usually used in applications with high event rate. Considering the opposite case, shown in Figure 2.5 c), in which τ is much greater than the charge collection time of the detector, the current flowing through R is much smaller and the current accumulates on the capacitor with capacitance C. C will then discharge through R and $V(t)$ returns to zero. In this case, high τ, the time in which the signal pulse reaches its maximum depends only on the charge collection time of the detector, and the external circuit does not influence its rise time; the necessary time to restore $V(t)$ to zero is influenced by τ; the maximum amplitude of $V(t)$ is determined by $\frac{Q}{C}$ and since C is normally constant, the amplitude of the signal pulse is directly proportional to the generated charge. Operation mode with high τ is the most commonly used. [5]

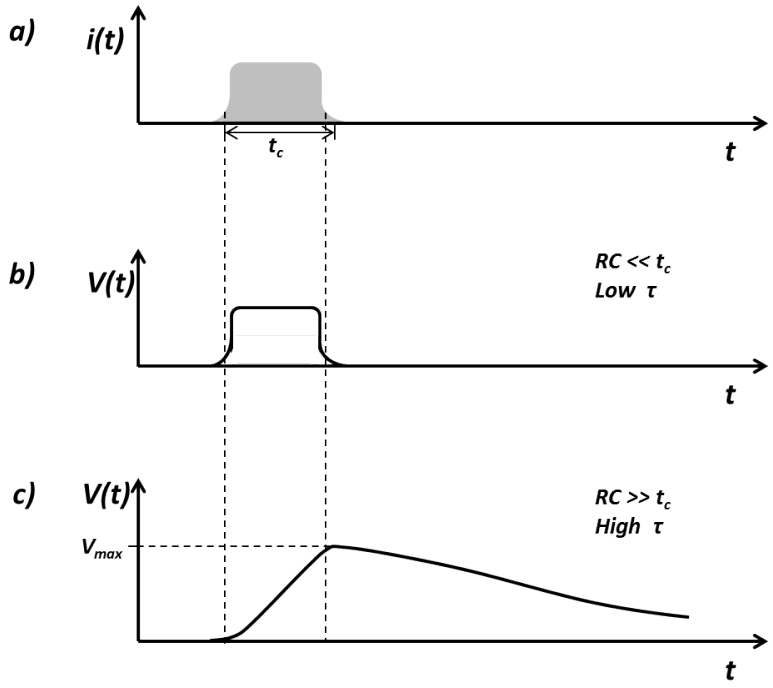

Figure 2.5: Detector operating in pulse mode. a) Current measured at the detector output; b) Case of low τ, in which the signal voltage, $V(t)$, has a similar shape of the measured current; c) Case of high τ, in which the signal voltage, $V(t)$, reaches its maximum after the charge collection time, t_c and then discharges through the resistance R.

2.3.2 Energy Resolution

An important characteristic under the scope of this work is the detector energy resolution.

Energy resolution can be studied irradiating the detector with a monoenergetic source and measuring its response function. A peak shall be recorded, since a monoenergetic source

is irradiating the detector. A more accurate response origins a thinner peak, otherwise a poorer response origins a larger (wider) peak. [5, 51, 50]

An accurate measurement of the detector energy resolution can be obtained by determining the relation between the FWHM of the response function and the peak centroid. Energy resolution can be expressed in percentage and, in this case, is dimensionless. The smaller the energy resolution value, the better the detector is able to resolve radiations with close energies. The detector should be able to resolve two energies that are separated by more than one value of the detector FWHM [5, 51, 50].

Energy resolution limitation can be due to some factors: instabilities of the detector operation during the measurements, random noise sources in the detector or associated electronics and statistical noise due to the discrete nature of the signal. Even if the operating characteristics of the detector remain stable and no random noise is present in the system, energy resolution is always limited by the statistical noise. [5, 51, 50]

2.4 MicroPattern Gaseous Detectors

MPGDs are produced based on photo-lithography, selective etching and laser machining to generate devices with components or readout stages in the order of the micrometers. MPGDs present some general capabilities that make them very interesting for imaging applications, such as [5, 51]:

- Possibility of setting a threshold level to reject electronic noise,
- High count rate capability,
- Good position resolution (in the micrometer range),
- Room temperature operation,
- Absence of dead areas,
- Possibility of using large areas,
- Low cost,
- Low complexity,
- Versatility,
- Portability.

The MPGDs used in this work were MHSP and THCOBRA. These detectors work in the proportional region with single photon counting capability, energy resolution and interaction position discrimination. Their properties and operation principle will be described in the next sections.

2.4.1 MicroHole and Strip Plate

The MHSP, proposed by J. F. C. A. Veloso in 2000, is a hybrid microstructure that derives from two other structures, the Micro Strip Plate (MSP) and the GEM [55].

The MSP consists of conducting micro-strips (series of cathodes and anodes) fixed on a glass substrate. This pattern is obtained by photolithography and its anode strips are typically 10 µm wide. [5, 56, 57, 51] This microstructure was created in 1986 by A. Oed to overcome the Multiwire Proportional Counter (MWPC) limitations and improve the charge amplification gaseous detectors. With MSP was possible to achieve better position resolution when compared with MWPC and high gains (above 10^4). [5, 56, 57, 51]

GEM was introduced in 1996 by F. Sauli and consists of a 50 µm insulating polymer foil coated with 5 µm of Cu on both sides [5, 58, 51]. In order to improve dielectric resistivity, a pattern of biconical holes with a diameter of typically 50-100 µm distanced 100-200 µm between each other is etched by photolithography process in this polymer [5, 58–60, 51]. GEM has high rate capability (above 1 MHz), gains in the order of 10^5 and promotes a good collection efficiency. [5, 59, 60]

MHSP merges the two structures described above. It consists of a 50 µm kapton^{TM} insulating substrate coated on both sides with a 5 µm Cu conductor layer. On the bottom face, series of anode and cathode strips are etched by photolithography, similarly to the MSP. Then, the structure is etched with biconical holes centered with the cathode strips, similarly to a GEM. [55, 61–64, 51] Also, the top face is structured in strips orthogonal to the bottom strips [63]. The holes are etched in a hexagonal pattern and have an inner diameter of 50 µm and an external diameter of 60 µm; cathode and anode strips are 100 µm and 20 µm wide, respectively, with a pitch of 200 µm. Two resistive lines connect the top and anode strips, respectively. [63] A photography of the MHSP structure can be seen in Figure 2.6.

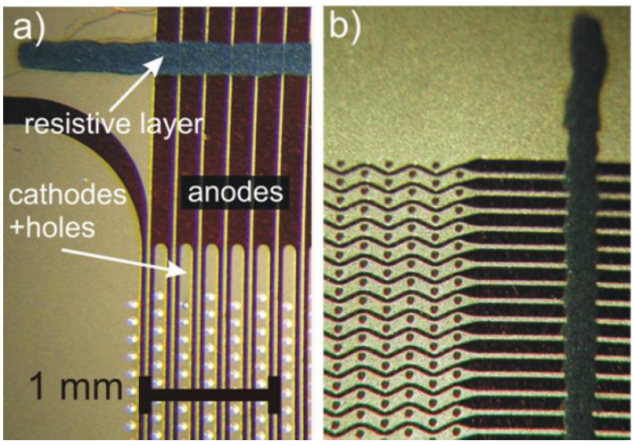

Figure 2.6: MHSP photos: a) Bottom face showing the cathode and anode strips with the holes positioned at the centre of the cathode strips; b) Top face showing the holes centred with the top strips.

As shown in Figure 2.7, the MHSP can achieve gains of about 10^4 when operating in pure Xe and the detector being irradiated with 5.9 keV X-rays. Figure 2.7 also shows an improvement of energy resolution as the gain increases, due to a SNR improvement. [65] The MHSP can work at high rates up to $5 \times 10^5 \mathrm{Hz/mm^2}$ when high gains are applied, having good gain stability (Figure 2.8). [66]

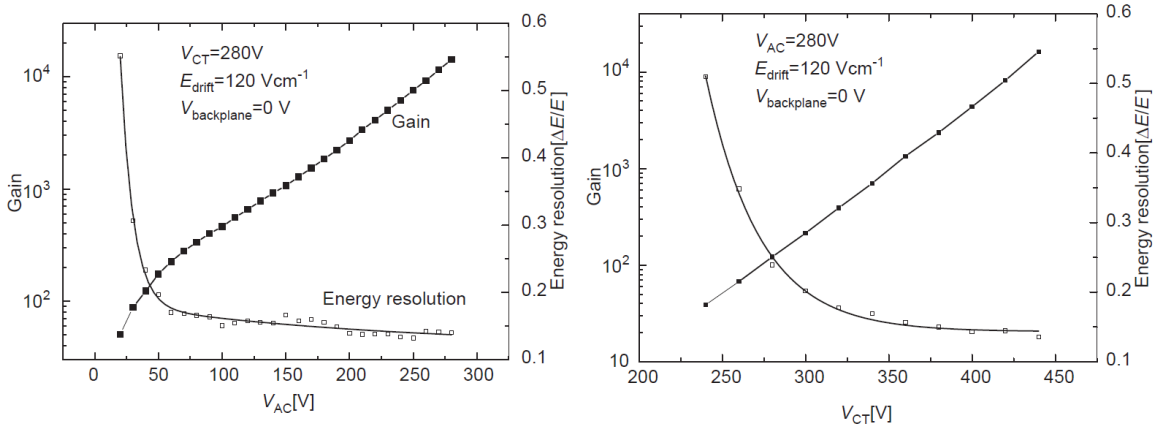

Figure 2.7: MHSP gain and energy resolution as a function of the applied voltage between anode and cathode strips (V_{AC}) (Left) and the applied voltage between top and cathode strips (V_{CT}) (Right) with the detector being irradiated with 5.9 keV X-rays [65].

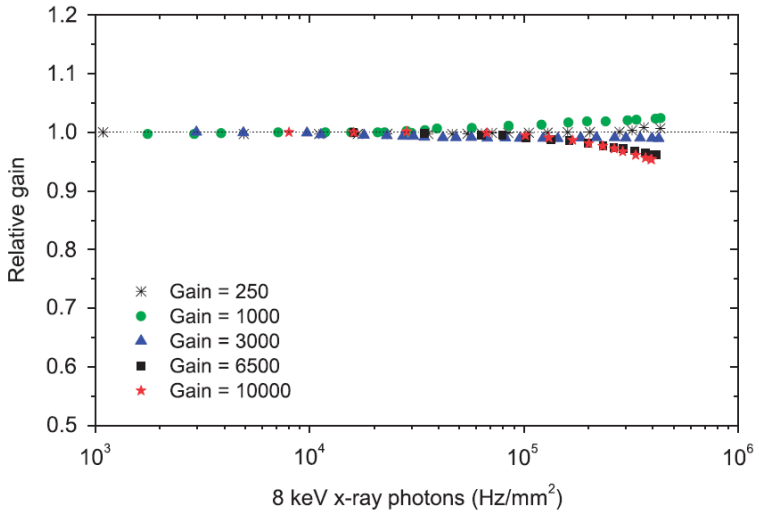

Figure 2.8: MHSP count rate for different applied voltages (gains) with the detector being irradiated with 8 keV X-rays [66].

A scheme of the MHSP operation mode can be seen in Figure 2.9. The application of an adequate potential difference between the top and cathode electrodes, focuses the free electrons generated by ionization above the structure towards the holes, where a charge

multiplication occurs. Another applied voltage between the cathode and anode strips induces a second charge avalanche. Therefore, with this structure it is possible to achieve, in one single plate, two charge multiplication avalanches. [67, 55]

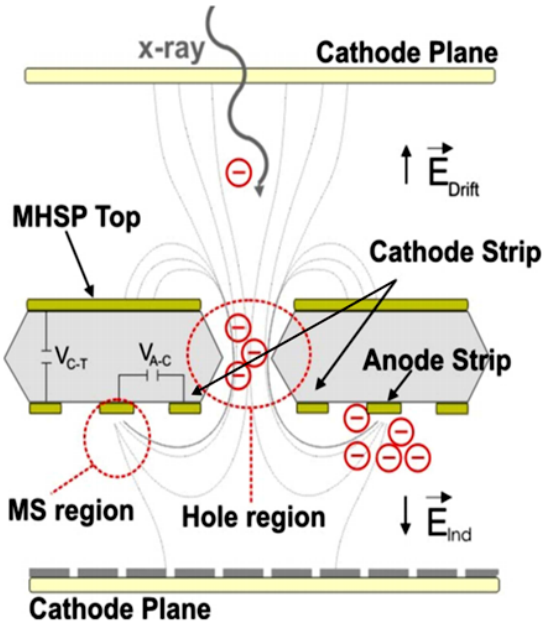

Figure 2.9: MHSP operation principle. The electrons generated due to the X-ray interaction are focused towards the MHSP holes where they suffer a charge multiplication due to the high electric fields. After exiting the holes, the electrons are targeted to the anode strips where they suffer a new charge multiplication [67].

The total charge produced is finally collected at the anode strips and conducted to the resistive line where it is split. The amount of charge that goes to each end of the resistive line depends on the interaction position. The charge is then collected at both ends of the resistive line by two pre-amplifiers, one at each end (Figure 2.13). [68]

2.4.2 Thick-COBRA

THCOBRA is based on two other structures: THGEM and MHSP.

THGEM is similar to GEM but with a more robust structure. It is made of a 0.4-3.2 mm printed circuit board (PCB) (e.g. G-10 or FR-4) coated with a Cu layer on both sides with a rim of 0-0.12 mm between the sub-millimetre to millimetre hole and the Cu layer. [69–71] The holes can have a pitch varying between 0.7 and 4 mm and the rim helps to reduce edge discharges, allowing to achieve a gain 10-fold higher than that without the rim (about 10^4 with rim) [70–72]. Relatively to the GEM, in THGEM no photon-mediated secondary process occurs, the structure is more robust, the electrons are better focused to the holes and high gains are possible, however it has a worst position resolution. [71, 73] Figure 2.10 shows a sketch of this structure.

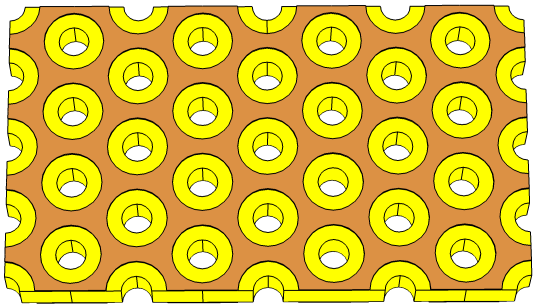

Figure 2.10: Sketch of a THGEM structure, showing its holes and rim. (Image drawn using COMSOL software [74])

THCOBRA, shown in Figure 2.11, is similar to a thicker and more robust MHSP, combining the advantages of the MHSP and THGEM. It also has a top strip pattern, series of circular anodes and cathode strips on the bottom face like MHSP and a hole pattern as THGEM. [2]

More specifically, THCOBRA consists of a G10 plate with a thickness of 0.4 mm coated with a 50 µm Cu layer on both sides. The structure is perforated with 0.3 mm diameter holes with a rim of 0.08 mm etched on both sides to reduce the discharge probability. The anode and cathode strips of the bottom face are 200 µm wide, with a pitch of 1 mm. [2, 75] In a further stage of development, the THCOBRA structure was produced with thinner anode strips, 40 µm, to increase its performance. Similarly to MHSP, THCOBRA has two resistive lines, one connecting the anode strips and the other connecting the top strips. [2, 75]

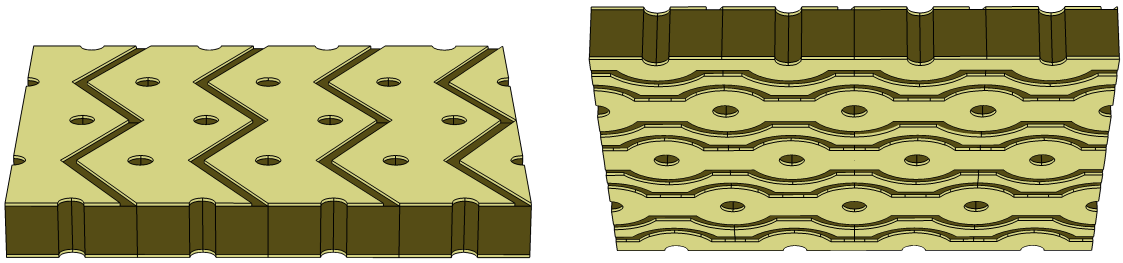

(a) Top (b) Bottom

Figure 2.11: THCOBRA structure showing the top pattern on the left and the bottom pattern on the right. (Image drawn using COMSOL software [74])

Its operation principle is similar to the MHSP, as shown in Figure 2.12, the primary electrons are focused towards the structure holes and suffer a charge multiplication due to the applied voltage. Another charge multiplication occurs in the anodes vicinity by applying another suitable voltage. [2]

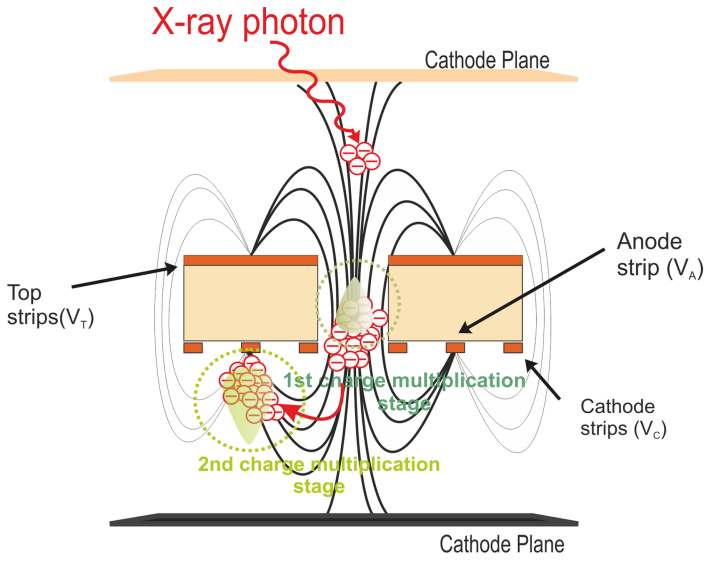

Figure 2.12: THCOBRA operation principle. Similarly to the MHSP, two charge avalanches occur inside the holes and in the anodes vicinity.

2.4.3 Position and Energy Discrimination

As shown in Figure 2.13, the two resistive lines connect the top and anode strips, respectively, and allow having 2D position discrimination, producing a 2D-MHSP and a 2D-THCOBRA. The typical resistance value is about 150 Ω between anode strips in 2D-MHSP, to keep the linearity in the position determination and the SNR of the pulses high enough [62]. In 2D-THCOBRA the resistance is about $50\,\Omega\,\mathrm{mm}^{-1}$. [75]

After converting and shaping the signals measured by the pre-amplifiers (Figure 2.13), the interaction position in one direction, x, is determined using the principle of charge division applying the following equation:

$$x = k\frac{X_A}{X_A + X_B} \tag{2.5}$$

where k is a calibration constant and X_A and X_B are the pulse amplitudes measured at each end of the resistive line. The other coordinate is determined in the same way, using the amplitudes measured at the ends of the other resistive line. Therefore, to determine the interaction position only four pre-amplifiers are needed, which is a very simple and low-cost solution. [50, 63] A position resolution of about 130 µm and 250 µm was achieved for x and y directions (corresponding to anodes and tops directions, respectively), operating 2D-MHSP in pure Xe at 1 bar. [68]

Using 2D-MHSP and 2D-THCOBRA, it is also possible to determine the energy of each single photon that interacts with the detector, by summing up the pulse amplitudes of one resistive line, as in the following equation:

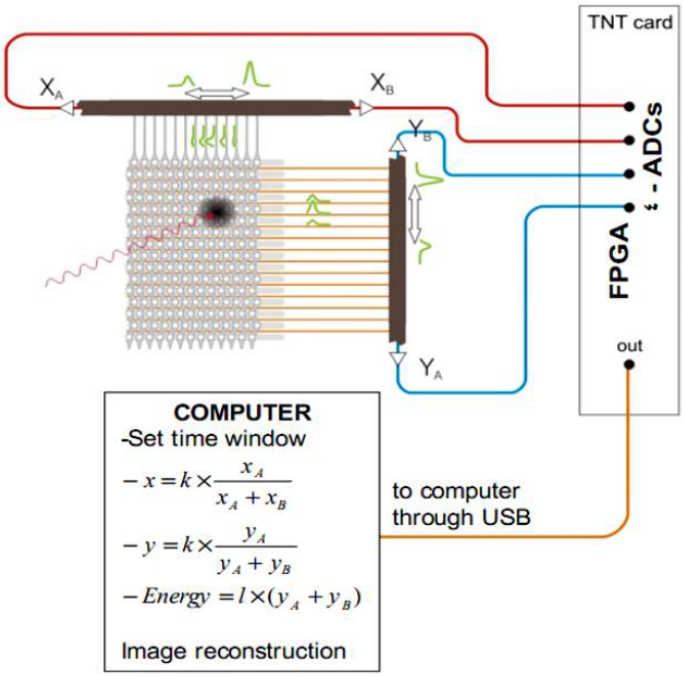

Figure 2.13: 2D-MHSP and 2D-THCOBRA photon position interaction and energy determination using two resistive lines orthogonal to each other.

$$E = k(X_A + X_B) \tag{2.6}$$

Since the signals on the 2D-MHSP and 2D-THCOBRA tops are induced by the anodes charge, their amplitude is much lower, about 35-45% of the anode signals, therefore, its SNR is consequently lower and the anode signals are the ones usually used to determine the incident photon energy. [63, 68] For 2D-MHSP an energy resolution of about 13.5% at 5.9 keV was achieved operating in pure Xe (at 1 bar) and at gains of about 10^4 (Figure 2.14). [65]

2.4.4 Energy Weighting Technique

In conventional X-ray detectors, widely used in medical imaging, the total energy is integrated. Therefore, the intensity distribution of the image is the result of the sum of the charge deposited for all the photons that interact with the corresponding pixels.

An energy resolving detector allows discriminating the photons according to the deposited energy, by measuring the signal amplitudes, which enables constructing an amplitude spectrum, i.e., an energy spectrum for each acquisition. The number of photons with a specific energy is registered (counted) in the respective energy bin:

$$E = E_0 + i\Delta E \tag{2.7}$$

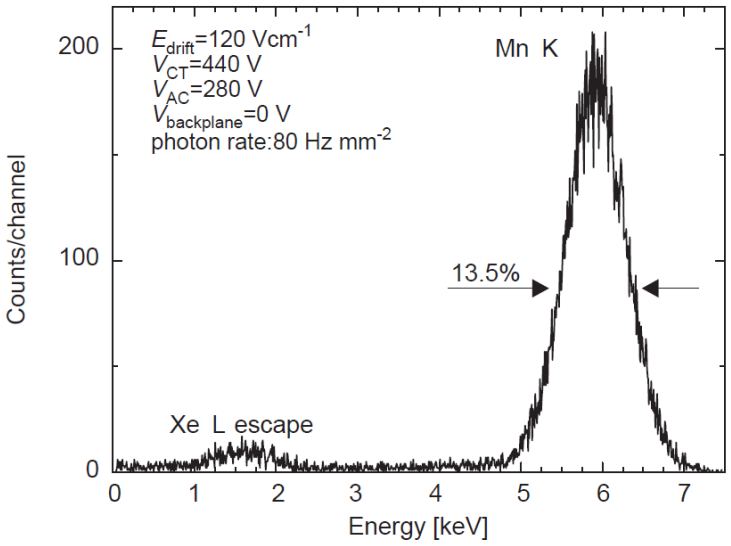

Figure 2.14: Pulse height distribution for 5.9 keV using MHSP where it was possible to determine an energy resolution of about 13.5%.

with ΔE the energy bin, i the running index, E_0 the energy threshold and E the total energy after irradiation. [76]

In this way, the information relating the intensity within a certain energy bin is available, being the intensity per energy channel, I_i, obtained by:

$$\langle I_i \rangle = T_i \times \langle n_i \rangle \tag{2.8}$$

T_i being the object transmittance and n_i the expectation of the number of incoming photons. [76, 77]

Considering an object with two different absorption coefficient regions, and consequently two distinct transmittances, T_i' and T_i, irradiated with a parallel X-ray flux, the signal per energy bin, S_i is given by [76]:

$$S_i = (T_i' - T_i)\langle n_i \rangle \tag{2.9}$$

The total signal can be obtained by summing up the signals of all energy bins. If the signal of each channel is multiplied by a certain factor before summing, this means that the signal is weighted according to its energy, $\widetilde{S}$, and can be obtained using:

$$\widetilde{S} = \sum_i S_i w_i \tag{2.10}$$

where w_i is the weighting factor. This weighting factor allows attributing more importance to certain signals than others. [76, 35]

To evaluate the influence of energy weighting in image quality, SNR can be measured for different weighting factors. SNR can be calculated using:

$$SNR = \frac{\widetilde{S}}{\sigma_S} \tag{2.11}$$

with σ_S the total noise for all the energy bins. Concerning the noise (with Poisson distribution), it can be calculated for each energy bin, which is the noise sum of the higher and lower attenuation coefficient regions, as in Equation 2.14 [76].

$$\begin{aligned} \sigma_{S_i}^2 &= \sigma_{I_i'}^2 + \sigma_{I_i}^2 && (2.12)\\ &\langle n_i \rangle T_i' + \langle n_i \rangle T_i && (2.13)\\ &\langle n_i \rangle (T_i' + T_i) && (2.14) \end{aligned}$$

Then, summing up the noise of each channel, the total noise, σ_S^2, is obtained using [76]:

$$\sigma_S^2 = \langle n_i \rangle (T_i' + T_i) w_i^2 \tag{2.15}$$

Therefore, a measure of SNR can be calculated using [76, 77, 35]:

$$SNR^2 = \frac{(\sum_i \langle n_i \rangle (T_i - T_i') w_i)^2}{\sum_i \langle n_i \rangle (T_i + T_i') w_i^2} \tag{2.16}$$

Using a weighting factor proportional to the photon energy, an integrating image is obtained, since the total charge, proportional to the energy, is summed. This is the case referred in the beginning of this section. The weighting factor can also be a constant, therefore, the number of photons that interact with the detector are summed up and a counting image is obtained (the case of counting detectors). However, it is of interest to determine the weighting factor that maximizes SNR. Using mathematical operations described in [76] or [35], it is found that the weighting factor is equal to [76, 77, 35, 36]:

$$w_i = k \frac{T_i - T_i'}{T_i + T_i'} \tag{2.17}$$

In case of having a low difference between two high transmittances, w_i will be small, because the intensities are high but similar, leading to low and noisy signal, consequently, low SNR [76]. As transmittance depends on the attenuation coefficient of the material, the optimum weighting factor depends also on it. Therefore, each material has an optimum weighting factor. [77, 35] The attenuation coefficient has a component dependent on energy, due to photoelectric effect, being proportional to E^{-3} and a constant component responsible for the Compton effect [35]. Figure 2.15 shows the weighting functions determined for breast tissue to breast calcification and breast tissue to adipose breast tissue in the 10 to 100 keV

energy range. [76]

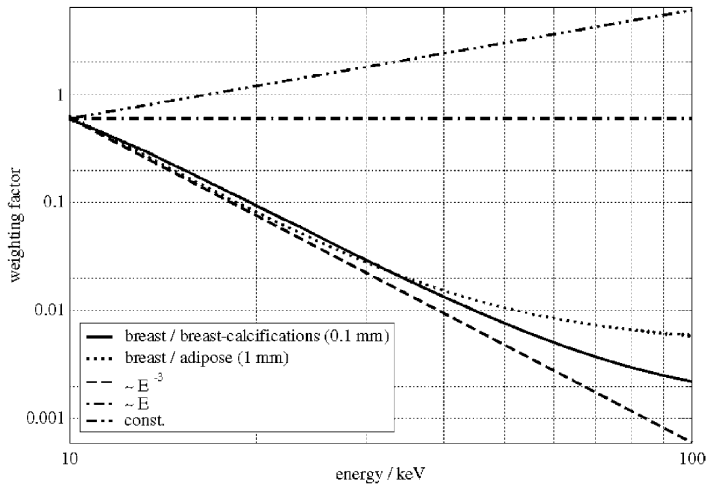

Figure 2.15: Two weighting functions for different material combinations (breast-breast calcifications and breast-adipose tissues) and the plot of three other functions: $\frac{1}{E^3}$, $\propto E$ (case of integrating detectors) and a constant (case of counting detectors) [adapted from [76]].

From Figure 2.15 it is possible to see that, up to 40 keV, the weighting factor is practically independent from the material composition and is proportional to E^{-3}, where photoelectric effect predominates. [76, 77]

Some examples showing the influence of applying this weighting factor in CT images using simulation results are shown in [76]. These examples include two phantoms, with low and high contrast, in a simple X-ray situation and a CT simulation with a phantom with different objects. In order to verify the influence of applying the three different weighting factors on image quality, distinct regions of interest in the image were analysed to calculate the SNR. Then, the SNR improvement was determined by calculating the ratio between the SNR of the weighted and the integrating images. A maximum SNR improvement of 50%, 20% and 90% was achieved in the low contrast phantom, high contrast phantom and CT simulations, respectively. [76, 78] Other simulation results were presented in [35] where a breast phantom was simulated in a cone beam system. In this case CNR improvements between 16% to 36% were achieved [35]. Equivalent studies were presented in [36] showing also a SNR enhancement comprised between 14% and 42% in the images [36]. An improvement of SNR in the projection images will result in the corresponding enhancement in the CT image. Energy weighting increases SNR in the projection images, corresponding to an improvement of CNR independently from interpolation and reconstruction techniques. [35]

Another option using spectroscopic detectors, since weighting results in better image quality, can be the reduction of dose in the X-ray acquisition [76, 77]. Giersch et al. showed also that the same SNR can be achieved with 2.5 times less dose than when using integrating detectors [76].

In a practical application, scattered radiation has to be taken into account and weighting function needs to be adapted. Scattered radiation increases for lower energies, being an additional noise, therefore, for lower energies, the weighting factors have to be smaller. Figure 2.16 shows the adapted function in case of having scattered radiation [77]

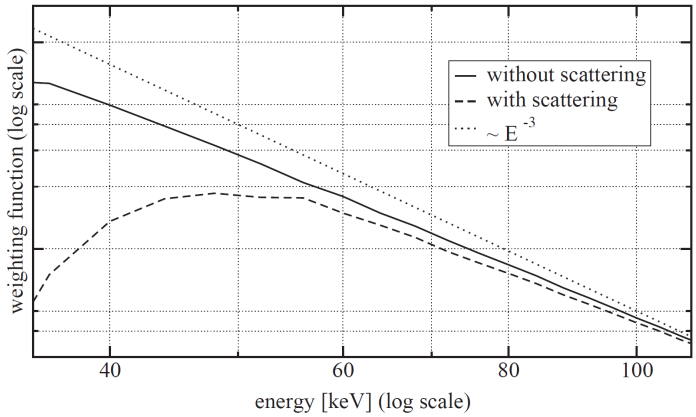

Figure 2.16: Weighting functions in the absence and presence of scattered radiation and the $\frac{1}{E^3}$ plot for comparison [adapted from [77]].

The bin size influences the SNR improvement when applying the EWT, as shown in [77] and [35]. SNR improvement is higher for lower size of energy bins, however there is always an improvement of SNR, even for higher energy bin sizes. [77, 35]

Part II

EXPERIMENTAL SYSTEM

CHAPTER

3

CT SYSTEM WITH MPGDS

3.1 Experimental Assembly

For CT measurements, a third generation CT scanner was built. The system is composed by a planar detector and the rotation was performed by the object (instead of the X-ray tube and detector) using a stepper motor. The SDD was high enough to consider a parallel X-ray beam geometry. A general sketch of the configuration of the X-ray tube, object, stepper motor and detector is shown in Figure 3.1. The X-ray beam is represented by the gray region.

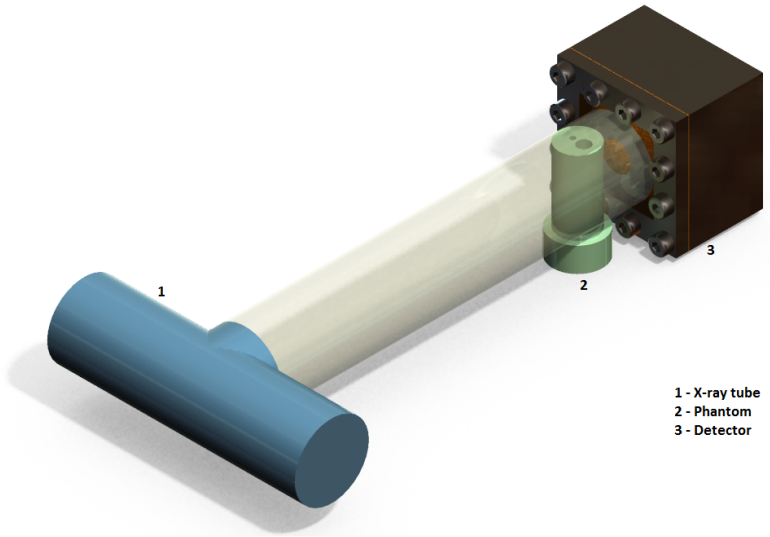

Figure 3.1: General sketch of the detector-object-tube arrangement. The grey region represents the parallel X-ray beam.

In CT the alignment of the system components is very important in order to obtain an image free of artefacts due to misalignments [79–83]. Therefore, the X-ray tube, the centre of rotation of the stepper motor and the detector centre have to be perfectly aligned.

3.1.1 X-ray tube

An X-ray tube from Oxford, series 5000 Apogee was used to produce the X-ray photons. It has a focal spot of 35 µm, a molybdenum anode with a maximum voltage and current of 50 kV and 1 mA, respectively. It was used continuously until the end of acquisitions and a controller allowed defining the exposure conditions: voltage and current. The exposure time is controlled by the user by turning the X-ray tube on and off.

3.1.2 Stepper Motor and Alignment System

For this work it is crucial to control exactly the object position to define parameters for acquisition and for the image reconstruction process. In this way, a very precise movement control and information about the angular position of the object relative to the X-ray tube and

detector must be available at each moment. Therefore, two stepper motors with a minimum step of 1.8° and 0.9° were used to promote the object rotation with precise movements. [84–86]

Two configurations to control stepper motors were used. The first was already implemented and is based on ULN2003 chip. A Labview application, shown in Figure 3.2, was developed to control motor parameters, such as rotation time, stop time at each position, angular step and number of turns. The other configuration allows controlling the motor using an Arduino UNO and an Arduino Motor Shield [87, 88].

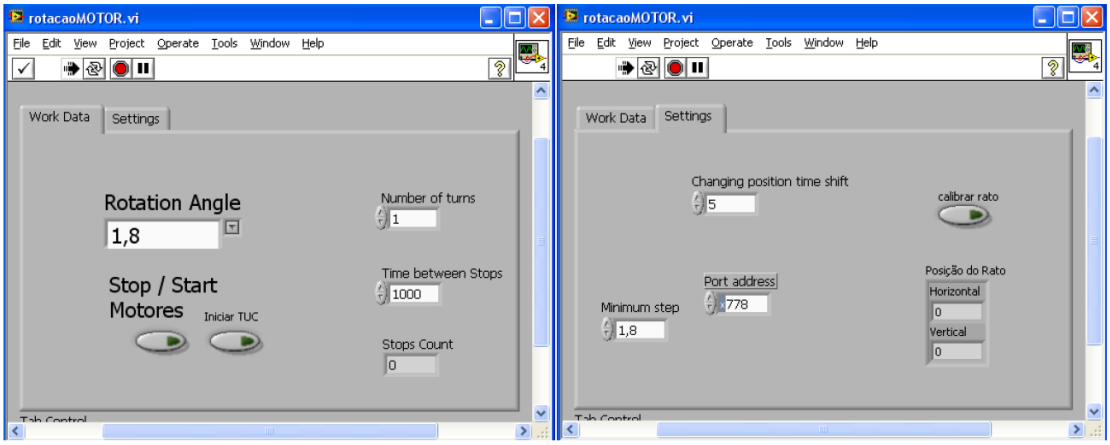

Figure 3.2: Labview graphical user interface (GUI) used to control the stepper motor.

Arduino UNO is a microcontroller board with in/out pins that communicates with the computer through Universal Serial Bus (USB) [87]. Arduino Motor Shield is a driver, based on the L298 integrated circuit, that powers the motor windings with the adequate current, allowing controlling the speed and direction of the motor [88, 89]. An external power supply was used to power up the system. Two programs, one developed in the Arduino integrated development environment (IDE) and another in Matlab® were written to control the motor and acquisition parameters. A Matlab® graphical user interface (GUI), shown in Figure 3.3, was developed to connect with Arduino through serial communication, sending and receiving data from it. The intended parameters for the motor rotation and data acquisition should be inserted in the GUI and sent to the Arduino UNO micro-controller by clicking on the "Send Motor & Gate Parameters". The type of stepper motor (with 0.9° or 1.8° of minimum step), the number of turns, the acquisition time of each view, the motor velocity and the step (that will define the number of views) will be sent to control the motor and consequently the acquisition parameters (acquisition time and number of views). The "Start Acquisition & Motor" button allows starting the stepper motor and acquisition program simultaneously, which is essential to obtain synchronized data. This will allow discarding the data stored during the motor motion and process the remain.

At the same time, an Arduino firmware program was developed to receive all this infor-

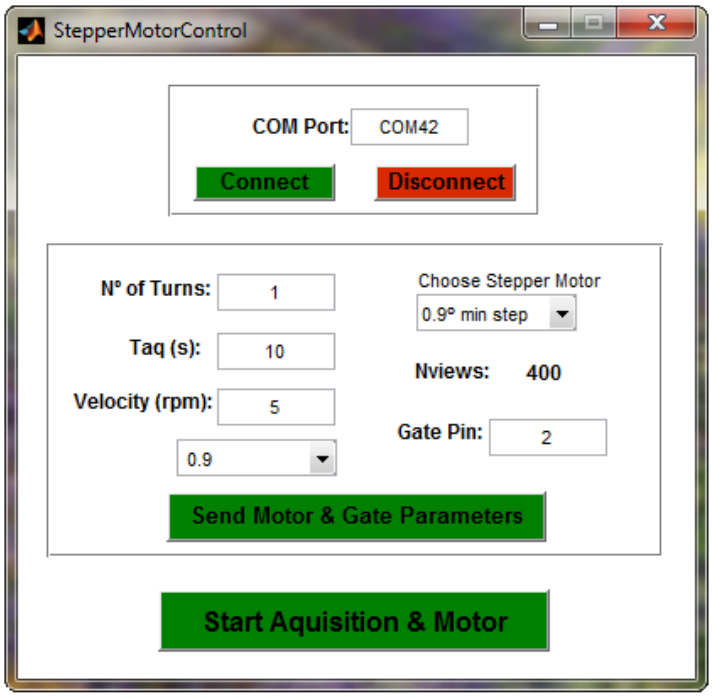

Figure 3.3: Matlab® GUI used to control the stepper motor.

mation and control the motor in accordance. The set of parameters are initialized and, after receiving the defined values through serial communication using Matlab®, they are defined. To assure that the data were received and interpreted correctly by the Arduino UNO, the values are sent back to the computer (to the Matlab® GUI) together with a message confirming the successful communication ("Motor and Gate Parameters Successfully Uploaded"), and shown in a dialogue box allowing the user to check everything. After this point, the Arduino UNO waits for the "order" to start the motor rotation. When the user clicks on the "Start Acquisition & Motor", the character "s" (of start) is sent to the Arduino UNO and both the stepper motor rotation and acquisition program start to save data simultaneously. During the acquisition, the number of the view is sent from the Arduino UNO to the computer and automatically refreshed, being shown in the bottom right corner of the Matlab® GUI.

For the first acquisitions (using 2D-MHSP), the X-ray tube, stepper motor and detector were placed on a table and aligned as best as possible by visual inspection. For the ensuing acquisitions (using 2D-THCOBRA based detectors) the stepper motor, X-ray tube and detector were placed in an optical bench, shown in Figure 3.4, in which the accessory supports allow moving the detector and stepper motor in three dimensions (x, y and z) and the X-ray tube in two directions (x and z). Other supports were projected and built to hold the detector, X-ray tube and stepper motor in the accessories of the optical bench. A base (in which the object is placed) was designed to be fixed to the stepper motor rotor. An interesting point is that the support of the detector was designed in such a way that it easily allows sustaining detectors with different configurations and dimensions.

Also, the X-ray tube support was designed to hold two laser lines centred with the X-ray focal spot centre. This allows aligning the centres of all the system's components with the focal spot X-ray tube centre. In Figure 3.4 a picture of the experimental setup, showing the considered system coordinates, is visible.

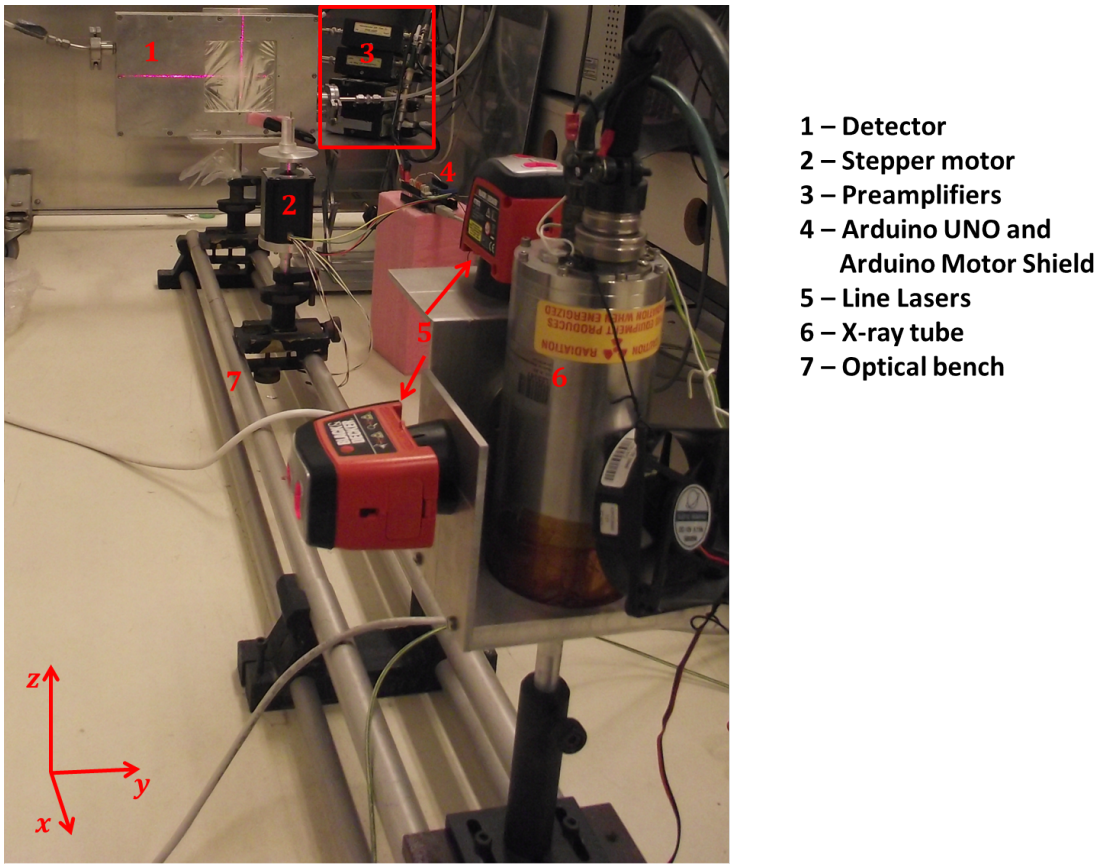

Figure 3.4: Photo of the CT system showing its main components: optical bench, support accessories, X-ray tube, line lasers, stepper motor, PMMA phantom, Arduino UNO, Arduino Motor Shield, 2D-THCOBRA based detector and pre-amplifiers.

3.1.3 PMMA Phantom and Other Scanned Objects

During this work, several objects were imaged. A PMMA phantom, already designed by the *Deteção de Radiação e Imagiologia Médica* - Radiation Detection and Medical Imaging (DRIM) group, was systematically used for acquisitions.

The CT phantom is a cylinder with 15 mm of diameter and 30 mm of height, made of PMMA. Its basis is larger with a diameter of 20 mm and a height of 10 mm. Two cylindrical holes were drilled with their longitudinal axes parallel to the longitudinal axis of the phantom. One of them has a diameter of 2 mm and the other 5 mm; their configuration is shown in Figure 3.5. In these holes a variety of different materials can be inserted, such as chalk, brass or aluminium rods. For the acquisitions, the phantom was fixed on the rotational system

controlled by the stepper motor. [90]

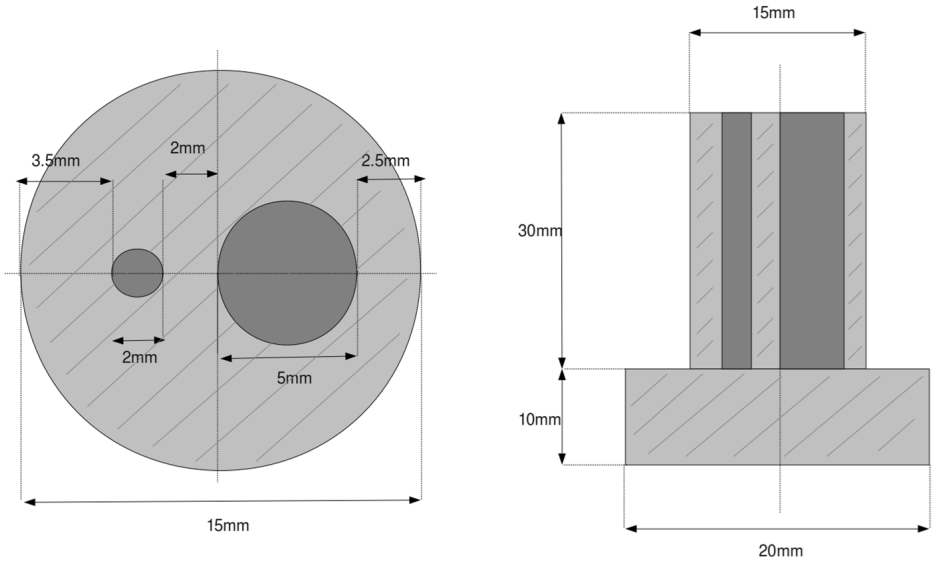

Figure 3.5: Sketch of the PMMA phantom designed for the acquisitions, showing its top (Left) and lateral (Right) view [90].

Other objects such as a sea snail, a butterfly, a subscriber identity module (SIM) card and an operational amplifier were imaged.

3.1.4 Detectors

Four detectors were used for this specific application using two types of microstructures: 2D-MHSP and 2D-THCOBRA. The structures used in this work and their working principle were described in Section 2.4.

3.1.4.1 2D-MHSP

The 2D-MHSP based detector (Figure 3.6 - top) has an active area of $2.8 \times 2.8\,\mathrm{cm}^2$, with the microstructure placed 3 mm apart from the detector window. A sketch of the detector configuration can be visualized in Figure 3.6 (bottom). This detector has a 75 µm kapton® window with an area of $3{\times}3\,\mathrm{cm}^2$ and a thin aluminium layer, deposited by evaporation, on the inside, working also as drift cathode. An electric field of about $330\,\mathrm{V\,cm}^{-1}$ was applied in the drift region. The detector chamber was filled with pure Xe (purity of 99.998%) at 1 bar working in sealed mode. No purifying system was used, thus the gas was changed every two days to keep position and energy resolutions good enough for measurements.

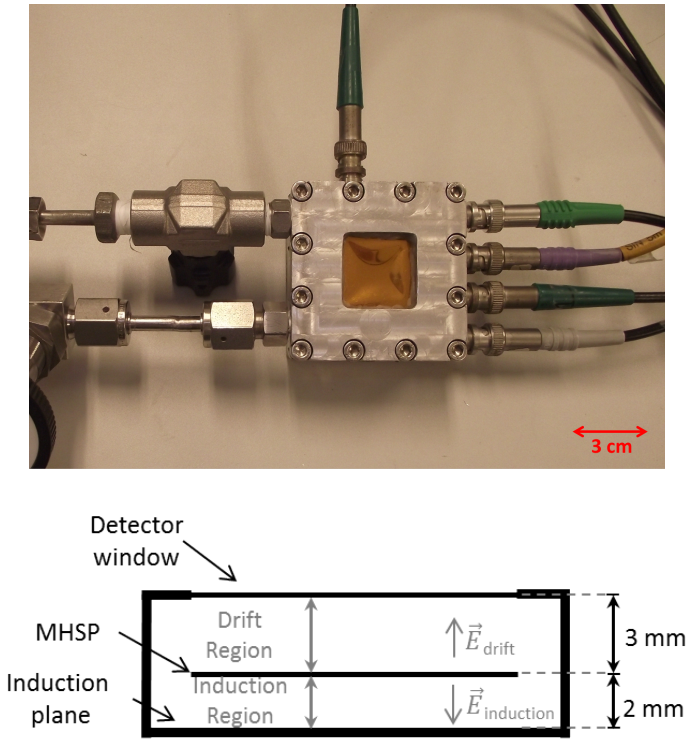

Figure 3.6: Top: Photo of the 2D-MHSP detector. Bottom: Detector configuration.

3.1.4.2 2D-THCOBRA

10 × 10 cm^2 active area with a THGEM pre-amplification stage

The first detector developed using a 2D-THCOBRA had an active area of 10 × 10 cm^2 and a charge pre-amplification stage performed by a THGEM. The drift plane is 0.7 cm apart from the detector window and 1 cm apart from the THGEM structure. The transfer region (between THGEM and 2D-THCOBRA) has 2 mm and the 2D-THCOBRA structure is 1.3 cm apart from the induction plane (detector bottom). The detector window is made of a 25 µm thick Mylar foil. This detector was operating in Ne/CH_4 (95/5) at 1 bar, working in a continuous gas flow mode of 25 mL/h. A sketch of this detector is shown in Figure 3.7. The drift and transfer fields were set to 450 V cm^{-1} and 1440 V cm^{-1}, respectively. This configuration was more complex than the one presently working at DRIM laboratory. A simpler configuration could be achieved due to a modification in the 2D-THCOBRA development and manufacture, as explained in the following detector configuration.

10 × 10 cm^2 active area

Further improvements in 2D-THCOBRA development allowed designing a structure with thinner anode strips, with a thickness of 40 µm. This improvement induces a concentration of field lines near the anode electrodes, increasing consequently the multiplication of the charge and the final charge gain. With this achievement, a simpler detector could be developed, using

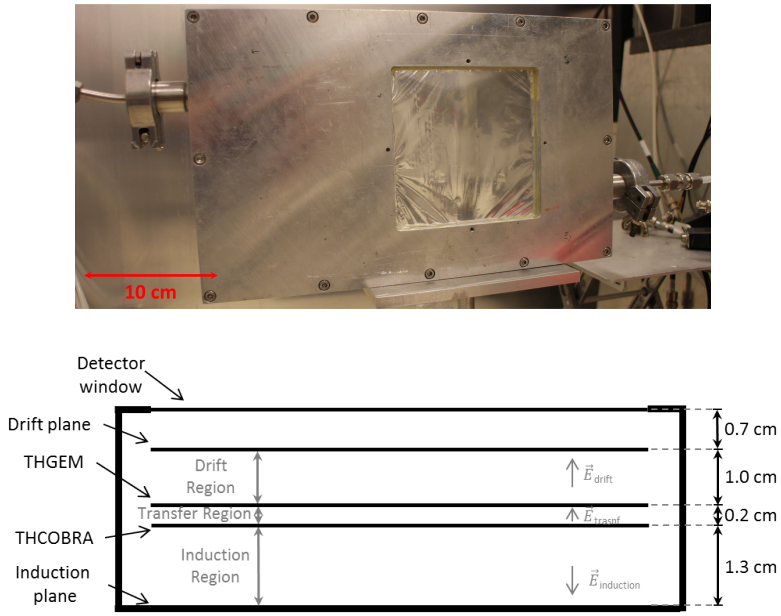

Figure 3.7: Top: Photo of the $10 \times 10\,\mathrm{cm}^2$ 2D-THCOBRA detector working in continuous gas flow. Bottom: Detector configuration using a drift plane, a THGEM as a pre-amplification stage and a 2D-THCOBRA structure.

a drift plane and a singe 2D-THCOBRA. The detector body and window were the same as the previous description. The new developed detector has a sensitive area of $10 \times 10\,\mathrm{cm}^2$ and its configuration is shown in Figure 3.8. The drift plane was placed 1.0 cm apart from the detector window and 1.0 cm above the structure, allowing the application of negative voltages. An electric field of about $350\,\mathrm{V\,cm^{-1}}$ was defined in the drift region. This detector was also filled with Ne/CH_4 (95/5) at 1 bar, working in a continuous gas flow mode of 25 mL/h.

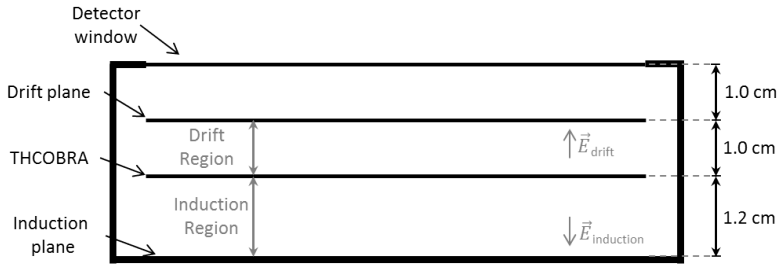

Figure 3.8: Detector configuration using a drift plane and a 2D-THCOBRA structure.

$2.8 \times 2.8\ \mathrm{cm}^2$ active area

The other detector, shown in Figure 3.9 on the left, was designed and developed during this work. It was filled with pure Kr (99.999% of purity), working in sealed mode, with the gas being purified by a sintered porous getter St 172 HI/7.5-7, kept at 225 °C, after being previously activated at 450 °C. This detector has a structure with an active area of

$2.8 \times 2.8\,\mathrm{cm}^2$. The upper part of the detector body was designed to allow the fixation of the

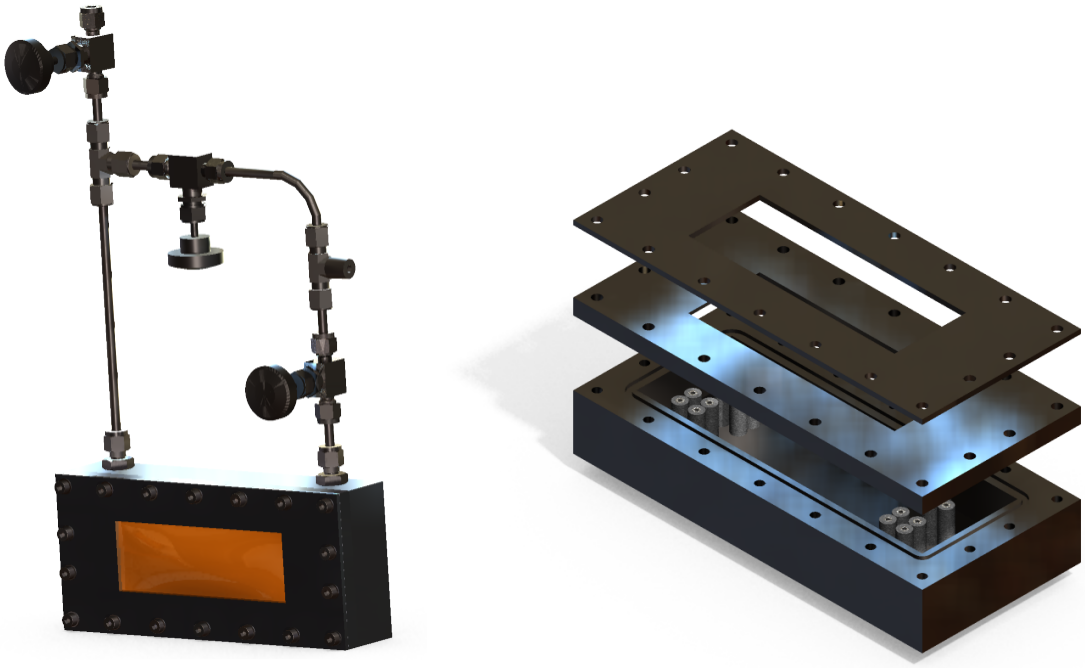

Figure 3.9: Left: Sketch of the detector with a $2.8 \times 2.8\,\mathrm{cm}^2$ THCOBRA with a getter inside. The tubing and valves to perform vacuum and fill the detector with gas are also visible. Right: Sketch of the detector body constituents, stainless steel feed-through and KETRON® PEEK-1000 insulators.

detector window, being 45 mm wide and 130 mm large. A middle frame was also created to increase the absorption region and to help to keep the window fixed. Figure 3.9 on the right shows an image of the detector body components. Duraluminium was chosen as material of the detector body since it is easier to machine than stainless steel.

The electric connections between the structure and the outside (Figure 3.10 (a)) were performed through stainless steel feed-troughs placed on the detector base. To insulate the feed-through from the detector body, insulators were designed and made of KETRON® polyetheretherketone (PEEK)-1000 [91], shown in Figure 3.10 (c) and (d).

The holes in the detector top allow fixing the upper parts with screws (Figure 3.10 (a) and (b)). Two threaded holes were created in the lateral wall in order to connect the gas system. Also an o-ring gland can be seen to insert a Viton® o-ring that will allow a complete sealing of the indoor environment from the outside by o-ring crushing (Figure 3.10 (c) and (d)).

The detector window was made of 125 µm DuPont™ Kapton® sheet with a thin aluminium layer deposited in the inner part by evaporation in order to work as drift cathode. The 1 cm drift region is located between the detector window and the structure and an electric field of about $600\,\mathrm{V\,cm}^{-1}$ was defined.

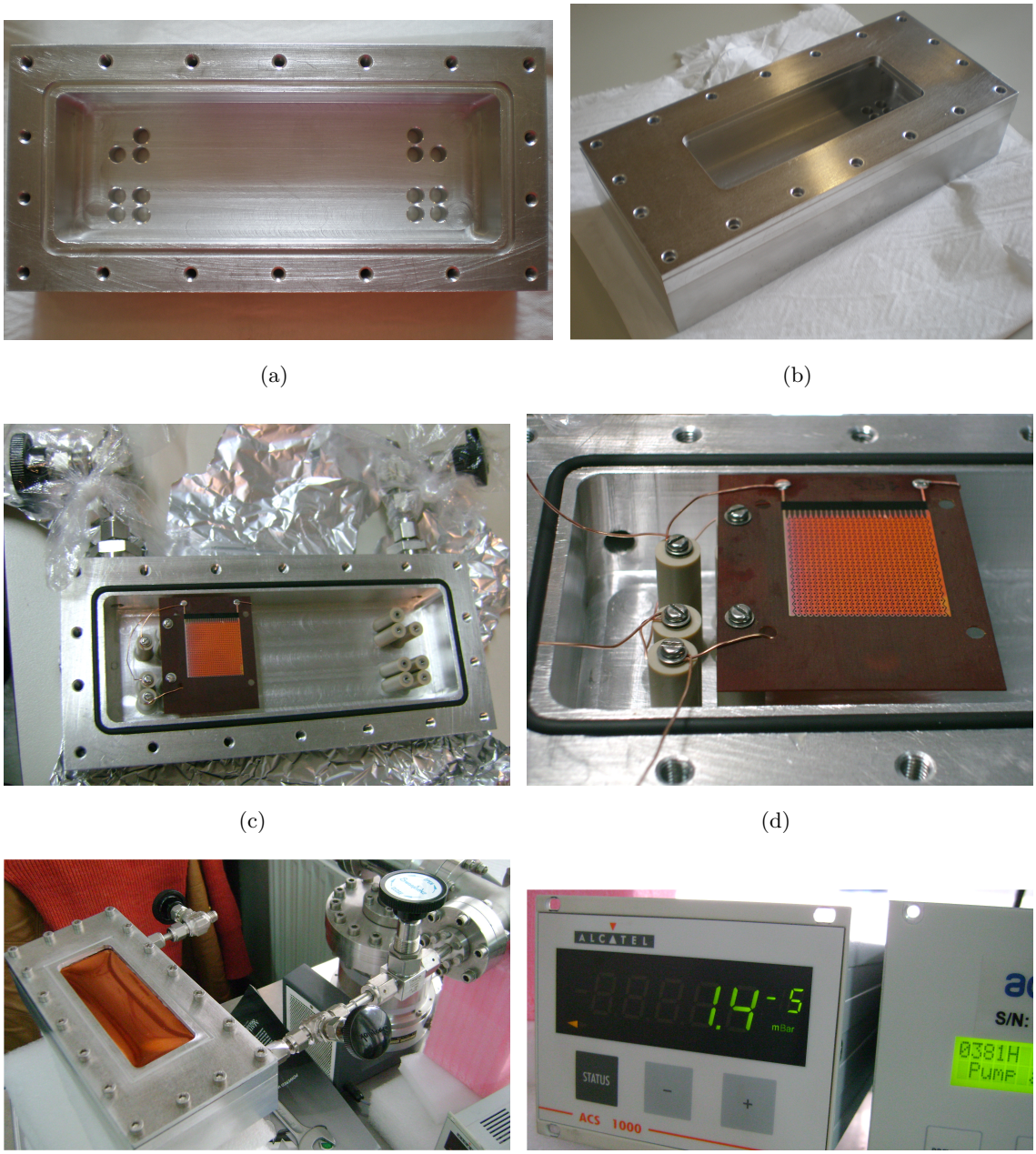

(a) (b)

(c) (d)

(e) (f)

Figure 3.10: Detector construction. Top: Detector body; Middle: THCOBRA structure connected to feed-through; Bottom: Detector vacuum system.

Before the assembly, all the detector components were cleaned to remove impurities in order to reduce gas contamination. The cleaning process consists of washing the detector with dish-washing detergent and water followed by a deionized water bath, isopropyl alcohol bath and, finally, acetone bath. After the bath, the pieces were placed in the oven at 50 °C for approximately 30 min to ensure a good drying. The feed-through and the insulating PEEK were glued to each other and then glued to the holes of the bottom part of the detector with

a low out-gassing epoxy: Tra-bond 2116 [92].

The $2.8 \times 2.8\,\mathrm{cm}^2$ 2D-THCOBRA structure was placed inside the detector and the connections electrodes-feed-through were done using screws and/or wire (Figure 3.10 (c) and (d)). The wires were soldered using pure Tin to avoid impurities from the commercial Tin solder. Finally, a sintered porous getter St 172 HI/7.5-7 [93], was also fixed to two feed-through of the opposite side. The detector was closed and connected to a vacuum pump. A pressure of 1.4×10^{-5}mbar was achieved during vacuum (Figure 3.10 (e) and (f)). Then the detector was filled with the chosen gas. A power source was connected to the getter feed-through and a current of 1.85 A was applied in order to activate the getter. For gas purifying purposes the temperature was kept at 225 °C.

The external parts of the feed-through were connected to a PCB designed for this application. It is connected to the high voltage power supply and to the readout electronics, having four pre-amplifiers (CREMAT CR-110) connected to the N1728B nuclear instrumentation module (NIM) digitizer.

3.1.5 Electronic Instrumentation

The detector bias was provided by the CAEN N471A high voltage power supply through the pre-amplifier for both 2D-MHSP and $10 \times 10\,\mathrm{cm}^2$ 2D-THCOBRA based detectors. For the $2.8 \times 2.8\,\mathrm{cm}^2$ 2D-THCOBRA detector the CAEN N1470 power supply was used.

Four pre-amplifiers were connected to the resistive lines of the detectors, one pre-amplifier at each end of the resistive lines. The charge is integrated in the pre-amplifier and a voltage pulse proportional to the charge pulse is produced. [5] In the 2D-MHSP and in the $10 \times 10\,\mathrm{cm}^2$ 2D-THCOBRA based detectors, four CANBERRA 2006 pre-amplifiers were used, while in the 2D-THCOBRA sealed detector four CR-110 pre-amplifiers from CREMAT were applied.

Following the pre-amplifiers, an ADC, CAEN N1728B with 14 bits, 100 MHz and four channels, was used to digitize the signals.

Each channel of the ADC collects the signal recording the amplitude and the time stamp. An event is translated into four signals within a certain time window. Therefore, after storing the pulses information, a Matlab® computer routine allows determining the coincident signals from four different channels within the specific time validation window, allowing the determination of the energy and position interaction of each event, as described in Section 2.4.1.

3.2 Image reconstruction for CT operation

Following the image acquisition, a data preprocessing is done. The events stored during the change of position of the stepper motor are discarded and the remaining events are correlated and organized in order to allow image construction. The non-coincident events

are discarded and the coincident ones are stored and processed to obtain sectional images, faithfully representing the imaged object.

The interaction position and energy of each single photon (of the correlated signals) are calculated using Equations 2.5 and 2.6, respectively, in Section 2.4.1. After calculation, the data is stored in three different cell arrays x, y and en:

$$
\begin{array}{cccccc}
\text{View} & 1 & & 2 & \ldots & \text{nviews} \\
x & \left\{\begin{array}{c} x_{1,1} \\ x_{2,1} \\ \ldots \\ x_{nevent_1,1} \end{array}\right\} & & \left\{\begin{array}{c} x_{1,2} \\ x_{2,2} \\ \ldots \\ x_{nevent_2,2} \end{array}\right\} & \ldots & \left\{\begin{array}{c} x_{1,nview} \\ x_{2,nview} \\ \ldots \\ x_{nevent_{nview},nview} \end{array}\right\} \\
y & \left\{\begin{array}{c} y_{1,1} \\ y_{2,1} \\ \ldots \\ y_{nevent_1,1} \end{array}\right\} & & \left\{\begin{array}{c} y_{1,2} \\ y_{2,2} \\ \ldots \\ y_{nevent_2,2} \end{array}\right\} & \ldots & \left\{\begin{array}{c} y_{1,nview} \\ y_{2,nview} \\ \ldots \\ y_{nevent_{nview},nview} \end{array}\right\} \\
en & \left\{\begin{array}{c} en_{1,1} \\ en_{2,1} \\ \ldots \\ en_{nevent_1,1} \end{array}\right\} & & \left\{\begin{array}{c} en_{1,2} \\ en_{2,2} \\ \ldots \\ en_{nevent_2,2} \end{array}\right\} & \ldots & \left\{\begin{array}{c} en_{1,nview} \\ en_{2,nview} \\ \ldots \\ en_{nevent_{nview},nview} \end{array}\right\}
\end{array}
$$

referring to the interaction position in x direction, the interaction position in y direction and the energy. The number of cells of each cell array is equal to the number of acquired views and in each cell the events are stored in a vector. The number of events of the three cell arrays (x, y and en) is the same for the same vector (corresponding to the same view), although it can be different, as probably is, between vectors corresponding to distinct views. Once the events are stored according to the time stamp, an event n of any vector corresponds to the n^{th} coincident event measured during the corresponding view.

This information allows reconstructing projection images: for the pixel corresponding to a specific position of interaction, the energy of the photon is summed, counted or weighted by $\frac{1}{E^3}$, depending if an integrating, counting or EWT image is intended, respectively, as described in Section 2.4.4.

Equation 1.3 shows the exponential dependency of X-ray attenuation. The intensity of reference, I_0, needs to be taken into account for a part of the data preprocessing. I_0 is measured from a non-attenuated part of the beam (that just crossed air) and then used as reference. Thus, the logarithm of the relation between the intensity measured after crossing the object and the intensity of reference is calculated [4, 1, 94]:

$$\log\left(\frac{I_0}{I}\right) = \mu x \tag{3.1}$$

The input parameters of the reconstruction algorithm are based on these calculated values [1].

Equation 1.3 also refers to the intensity measured in the detector after a polychromatic X-ray beam crossed a tissue (composed by several materials), named line integral (Figure 3.11). As suggested by the name, the line integral is the integral of an object parameter along a line, in this case, it represents the total X-ray beam attenuation when travelling in a straight line through an object. In practice, the mapping of attenuation coefficients is done using discrete values, since CT sampling is also discrete. The set of line integrals acquired in a specific position X-ray-tube-object-detector is called projection or view. In each angular position of the object, relative to the X-ray tube-detector, a projection is acquired. This means that in a single measurement it is not possible to determine all the attenuation coefficients that contribute to the total attenuation. [3, 94, 95]

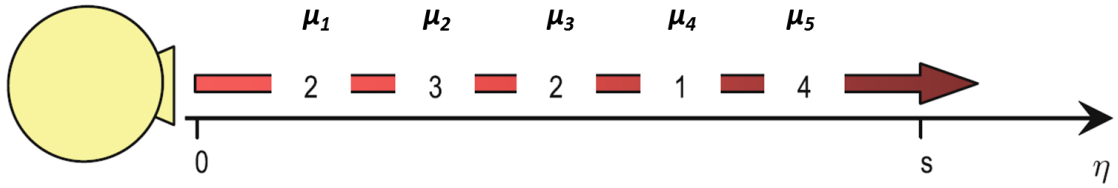

Figure 3.11: X-ray attenuation along a straight line through a tissue [adapted from [3]].

When an X-ray tube and detector rotation occurs, the referential is not fixed, however for image reconstruction purpose, a fixed referential (x,y) needs to be considered. In Figure 3.12, the fixed referential is defined as (x,y) and the rotating as (θ, p). Then, both referential have to be mathematically related, as shown in Figure 3.12, in which a line (parallel to q) inside the region of interest (ROI) can be written as [96, 95]:

$$p = x\cos\theta + y\sin\theta \tag{3.2}$$

Using the referential relation and a delta function, a projection can be written as [95]:

$$P_\theta(p) = \int_{-\infty}^{\infty}\int_{-\infty}^{\infty} f(x,y)\delta(x\cos\theta + y\sin\theta - p)dxdy \tag{3.3}$$

This is the Radon transform of the $f(x,y)$ function [95], in which the 2D projections define the corresponding line integrals [96]. [96, 94, 95]

Before image reconstruction the projections are organized in a sinogram, which is a graphical representation of the ray intensity emerged from the object as a function of the radial,

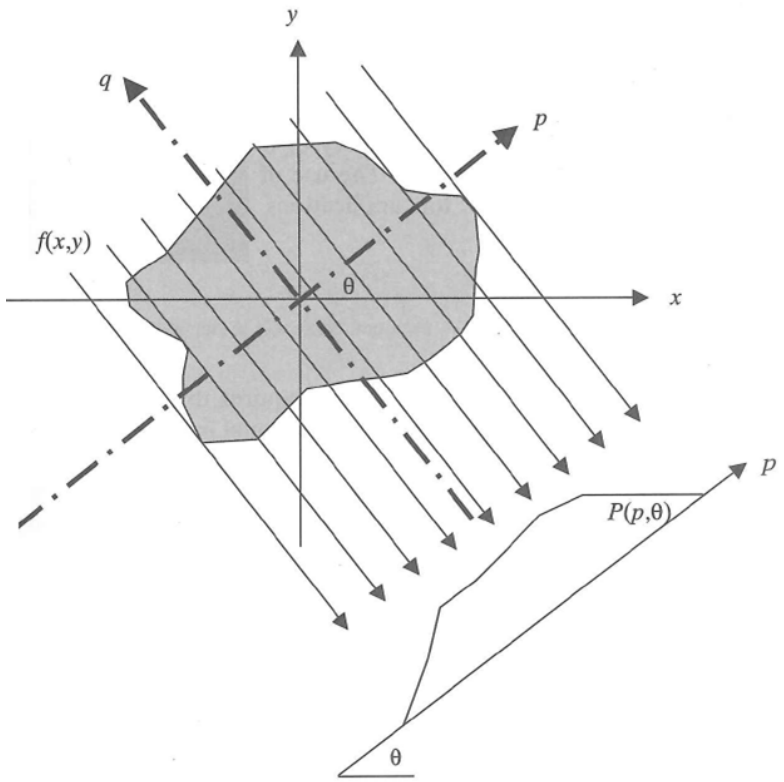

Figure 3.12: Object, $f(x, y)$, and its projection, $P_\theta(p)$, at an angle θ relative to the fixed referential (x,y) [adapted from [96]].

p, and angular,θ, coordinates. The sinogram is the Radon transform of all the imaged object points. [4, 94]

Different sinograms can be obtained, according to the weighting performed in projections. The sinogram is the basis for the image reconstruction algorithm. Cross-sectional images are reconstructed using a FBP algorithm, which encompasses filtering the projections and then their backprojection. The filtering part can be seen as weighting each projection in the frequency domain and the backprojection as simply dividing the attenuation measurements evenly along the ray path in the space domain. Since the filtering is required in the frequency domain, a Fourier transform (FT) is applied to the projections in order to multiply by the chosen filter. Otherwise, the backprojection is done in the space domain, therefore the inverse Fourier transform (IFT) is performed prior to this part. [95, 97]

This process can be summarized as follows:

- Create sinogram
- Perform the FT of the projections
- Apply ramp filter to the projections in the frequency domain
- Perform the IFT of the filtered projections

- Backproject the filtered projections in the space domain

In this work, for the cross-sectional image reconstruction a solution already built-in in Matlab® was used. Image processing toolbox allows the use of the *iradon* function, which is essentially the inverse Radon Transform, and allows reconstructing an image from parallel projections. The input parameters of this function are the sinogram and a vector with the angular position of each view. Besides, a choice between different filters is available. [98]

Image reconstruction steps are illustrated in the flowing chart of Figure 3.13.

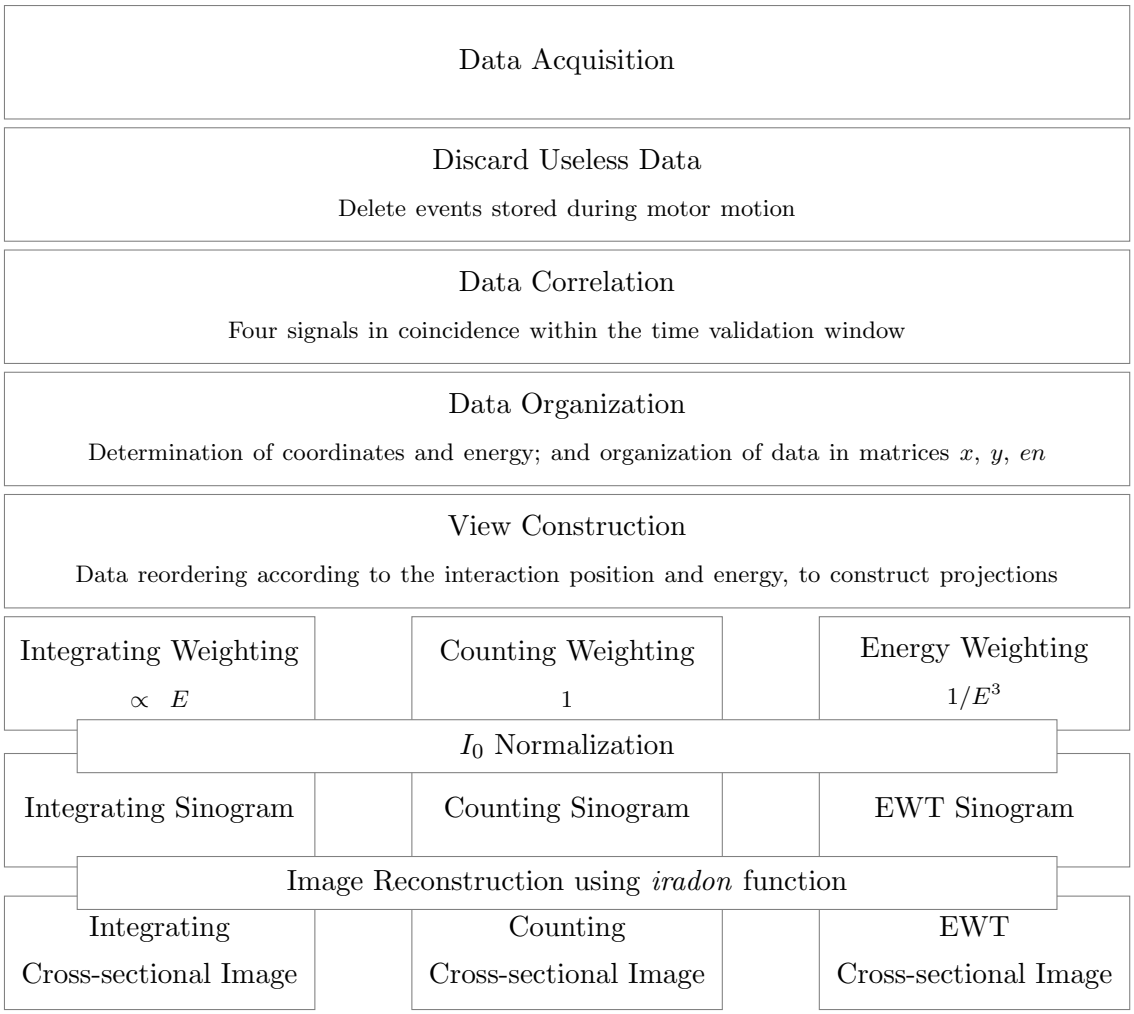

Figure 3.13: Flow diagram of image reconstruction process.

3.2.1 CTRADIX and RADIX

CTRADIX and RADIX, Matlab® based programs using GUIs, were developed by the DRIM group to read the files from the acquisition program and reconstruct the images.

RADIX was developed for projection images construction and visualization, having also the fluoRADIX mode to work with fluorescence imaging, while CTRADIX is dedicated to

CT imaging. A set of input parameters can be defined in RADIX and CTRADIX for event correlation and image construction, such as the time validation window, number of pixels, reconstruction technique (integrating, counting or EWT), image offset and multiplication factors for each coordinate and gains of each channel. CTRADIX has other input parameters essential for the image reconstruction process: acquisition time of each view, the time the stepper motor takes to change position, number of views, the total angle performed by the stepper motor and the number of slices to reconstruct.

CTRADIX was changed to include the reconstruction technique (integrating, counting or EWT), the I_0 normalization, flat field correction, energy correction, multi-slice and 3D reconstruction and visualization and to allow other functionalities, as for example the construction of projection images, measurement of the mean, standard deviation and SNR in an image ROI, marking the image centre and correcting misalignments of the rotation centre in the acquisition process.

I_0 Normalization

I_0 normalization is done by selecting an area without any object projection in all the views. Therefore, in the acquisition process, careful attention was paid to have a region with no object in which the X-ray crossed just air in all the views (for all the angular positions of the object relative to the X-ray tube and detector).

SNR of a ROI

The SNR of the image ROI is calculated by the CTRADIX program as explained in Section 4.2. The area marked for measurements can be easily removed using the appropriate tool also developed.

Correction of misaligned components

The misalignment of the system components, visible in the sinogram, was corrected doing an intuitive evaluation. A metric evaluation can be also used, measuring the SNR in an image contour. The tool was developed in the form of GUI executed using a button in CTRADIX. The tool allows defining the minimum and maximum shifts and the steps, in pixels, with which the program will test the reconstruction. For example, if the user selects a minimum shift of -5 and a maximum shift of 5 with a step of 2, a set of sinograms is created with their centre shifted by -5, -3, -1, 1, 3 and 5 pixels relatively to the original sinogram; if the step is 1, 10 sinograms will be constructed with the centre shifted from -5 to 5 continuously. For each sinogram a cross-sectional image is reconstructed and the user can evaluate the image quality visually. An assistant tool was developed to help on the evaluation of the resulting images: a region of the image where a contour is present should be selected to measure the SNR, and the better the contour definitions, the worst the SNR. Therefore, a thoughtful evaluation should be done using both visual and SNR appreciations.

Flat Field Correction

MPGDs do not have an uniform amplitude response, varying along its resistive area. If a flat field image is available, the flat field correction can be included in the image pre-processing step by activating the respective check box. The main objective is to correct the non-uniformities of the detector response. [99, 100] A flat field acquisition, in which the detector is irradiated with poly-energetic radiation from the X-ray tube (without any object between the detector and X-ray tube), is required. Whenever the Flat Field Correction check box is activated in the main CTRADIX GUI, the file with the flat field acquisition data can be selected. Then, the mean intensity is calculated and divided by the flat field image, allowing to determine a matrix with a correction factor for each pixel. In this way, the pixels with an intensity (response) lower than the mean intensity, will have a correction factor higher than 1, otherwise in the case of having an intensity higher than the mean intensity, their correction factor will be lower than 1. These obtained correction factors are multiplied by the respective pixel of the transmission image in order to normalize the detector response. [99, 100] In CT, this procedure is applied in all the projection images before reconstructing the cross-sectional image.

Energy Correction

The energy correction method described in Ref. [101] was implemented on CTRADIX to correct the intensity non-uniformities due to variations on the amplitude response in the projection images. A flood image needs to be acquired and can be used to apply this correction method by activating the respective check box. A flood acquisition is performed by irradiating the detector uniformly with a monochromatic radiation, as for example fluorescence k-lines of Cu. The flood image is divided into small element-areas and their pulse height and respective centroid are determined. The centroids mean is calculated and divided for each centroid element-area to determine a matrix containing the correction factors for each element-area. Then, the pulse amplitude of each element-area is multiplied by their correction factor. [101] Similarly to flat field correction, this correction is implemented in the projection images before cross-sectional image reconstruction.

Multi-slice and 3D Reconstruction

Multi-slice reconstruction was also implemented in the CTRADIX GUI. The user defines the intended number of slices and the projection images are divided accordingly. For each section, a sinogram is constructed and the corresponding cross-sectional image is reconstructed. A slider bar allows to "travelling" between slices of the object.

Using the slices from the multi-slice reconstruction, 3D reconstruction was also implemented. Similarly to the correction of misalignments of the rotation centre, this tool is available in a form of a GUI which can be executed by pressing a button in the main CTRADIX GUI. The cross-sectional images are stacked up in a 3D graphic. A window of values repre-

sentative of a specific surface can be defined and the corresponding iso-surface represented.

Part III

RESULTS

CHAPTER

4

CT SYSTEM USING A 2D-MHSP DETECTOR

4.1 Energy Window Image Reconstruction

Since energy resolved single photon counting is possible with 2D-MHSP, the spectral distribution is available. Therefore, using this information, image reconstruction using partial energy ranges of the spectrum is possible. The acquisitions were performed with 30 kVp, 340 µA and an additional X-ray tube filtering of 2 mm of Al to remove lower energy contributions. 200 views were acquired in a full rotation with a SDD of 150 cm and the object placed as close to the detector as possible. Since the beam divergence was very low (about 0.7°), it was considered that the X-ray beam had a parallel geometry. The acquisition time of each view was 2 s and the motion time of the stepper motor was 5 ms. A slit, with $0.5 \times 25\,\mathrm{mm}^2$, was placed in front of the detector window to collimate the beam. Cross-sectional images were reconstructed with 90×90 pixels using sinograms with 128 rays and 200 pixels. The number of defined pixels allowed achieving a good compromise between the image SNR and the contours definition, since a higher number of pixels will not improve spatial resolution (limited by the detector response) and will degrade the SNR. This is valid for all the studies done with the 2D-MHSP based detector. [90]

Depending on the selected range, different objects with distinct attenuation coefficients are more evident. Figures 4.1 and 4.2 show examples of energy range image reconstructions. In the first case, an acquisition of the PMMA phantom with chalk and air was done and in the second case the phantom was filled with chalk and brass on the 5 mm and 2 mm holes, respectively. In both cases three images were reconstructed with the integrating method using the low, medium and high energy windows.

In the case of the PMMA phantom with chalk and air, shown in Figure 4.1, the low energy image was reconstructed using the energies between the ADC channels 150 and 600 corresponding to 2.5 keV and 11 keV. The medium energy image used the energy range between 11 keV and 19 keV (ADC channel 900). The remaining photons of the spectrum, with energies between 19 keV and 30 keV, were used to reconstruct the high energy image.

In the case of the PMMA phantom with chalk and brass, shown in Figure 4.2 the low energy image was reconstructed using the photons with energies up to 13.3 keV (channel 400). The medium energy image was obtained with the photons with energies between 13.3 keV and 20.8 keV (channel 400 to 625) and the high energy image was reconstructed using the photons with energies from 18.3 keV up to the maximum (from channel 550).

Due to the different attenuation coefficients of the materials, different structures are evidenced depending on the energy range selected to reconstruct the image. In both cases, the PMMA phantom is more evident in the low energy images. The medium energy image shows the chalk rod better than the other two images. The brass rod is also evidenced in the medium energy image, in the case of PMMA phantom with chalk and brass. However, the brass rod is the component best visualized in the high energy image. The high energy

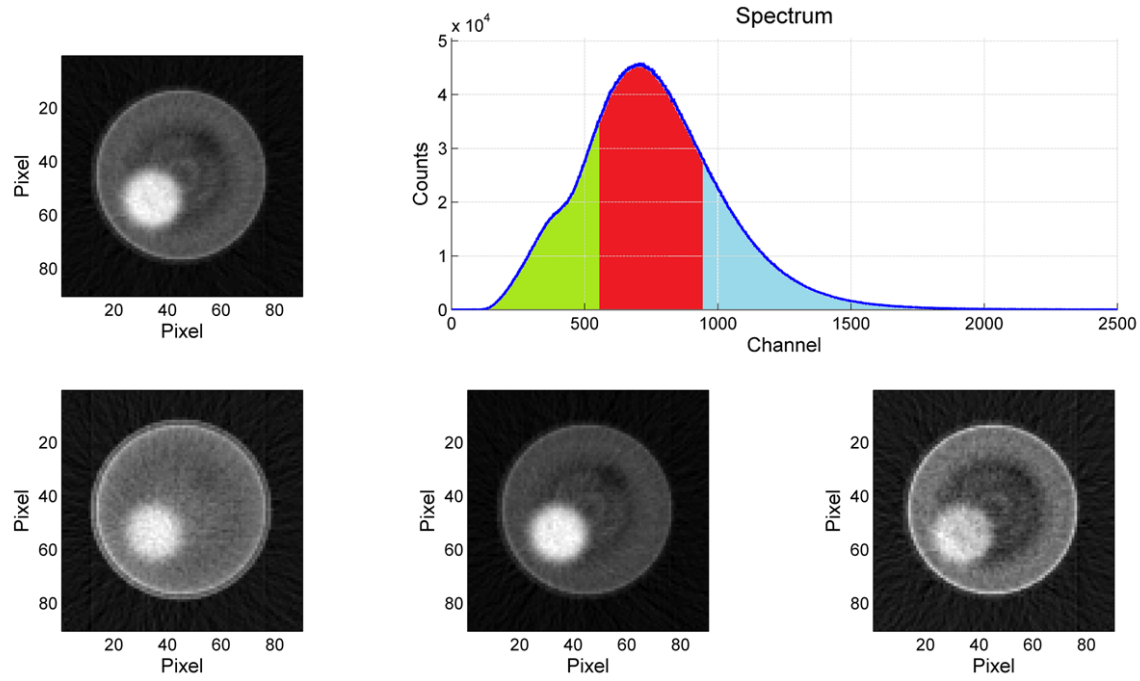

Figure 4.1: Energy range image reconstruction of an acquisition of the phantom with chalk and air done with MHSP detector (30 kVp; 340 µA and 2 mm of filtering). Top - Left: Cross-sectional image reconstructed using the full spectrum. Top - Right: The spectrum with the ranges used for image reconstruction marked with different colours: green corresponds to the low energy range; red to the medium energy range and blue to the high energy range. Cross-sectional images of the phantom with chalk and air reconstructed using low (Bottom - Left); medium (Bottom - Middle) and high (Bottom - Right) energy ranges [90].

images show some artefacts, similar to a cupping artefact, that can be due to the non-uniform response of the detector for the different energies.

The presented CT images show some artefacts due to beam hardening, visible as white strikes in several images. For the different combinations of objects in the PMMA phantom, the cross-sectional images show also good definition of contours of all objects, truthfully representing the imaged object.

4.2 Energy Weighting Technique

EWT was also applied to the data acquired with 2D-MHSP in the acquisition made with the phantom filled with chalk and air. The acquisition parameters were the same described previously (Section 4.1). The three types of images, integrating, counting and EWT, were reconstructed with 90×90 pixels using a sinogram with 128 rays and 200 views. Figure 4.3 shows the obtained images, as well as the acquisition spectrum with the energy range used for

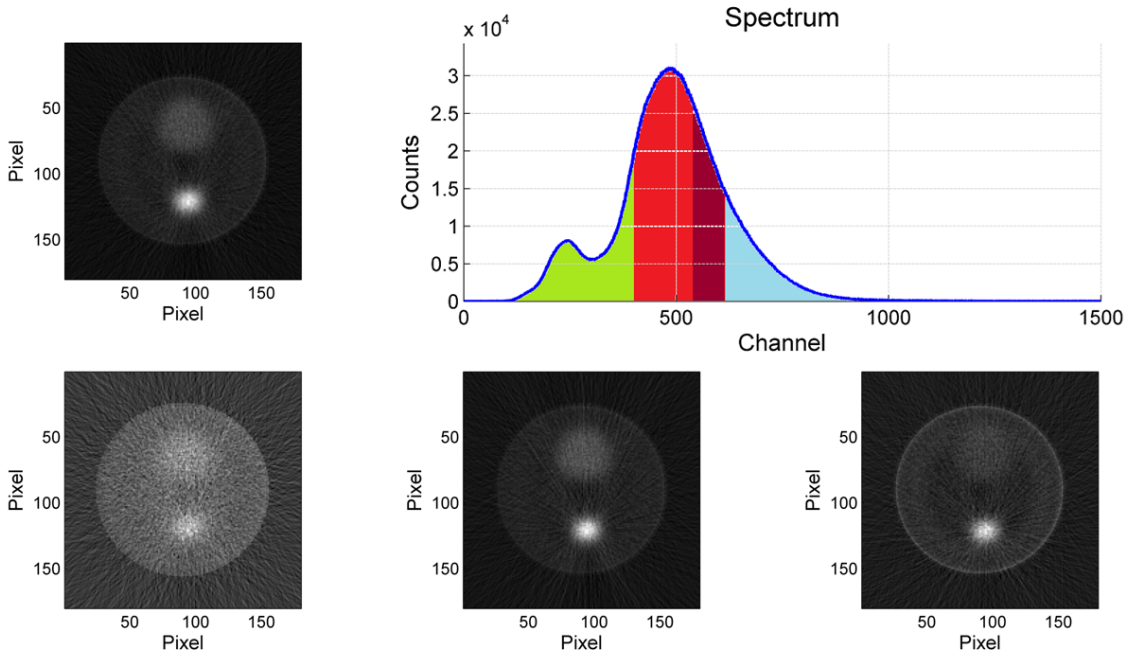

Figure 4.2: Energy range image reconstruction of an acquisition of the phantom with chalk and brass done with MHSP detector (30 kVp; 340 µA and 2 mm of filtering). Top - Left: Cross-sectional image reconstructed using the full spectrum. Top - Right: The spectrum with the ranges used for image reconstruction marked with different colours: green corresponds to the low energy range; red to the medium energy range and blue to the high energy range. The darker region in the spectrum corresponds to a superposition of medium and high energy ranges. Cross-sectional images of the phantom with chalk and air reconstructed using low (Bottom - Left); medium (Bottom - Middle) and high (Bottom - Right) energy ranges [90].

reconstructions (from 7 to 30 keV), the line profiles of the different images and the selected region in detail.

The contrast, SNR and CNR enhancements were evaluated comparing counting and EWT images with integrating image using the region marked with the red rectangle in Figure 4.3 (Bottom Right). The image contrast is defined as:

$$C = \frac{\mu' - \mu}{\mu' + \mu} \tag{4.1}$$

where μ' and μ are the mean intensities of the higher and lower intensity regions, respectively [3]. The contrast ratio of two different images, C_A and C_B, reconstructed with the same raw data but different weighting factors, is a measure of the contrast enhancement [90]:

$$C_{enh} = \frac{C_A}{C_B} \tag{4.2}$$

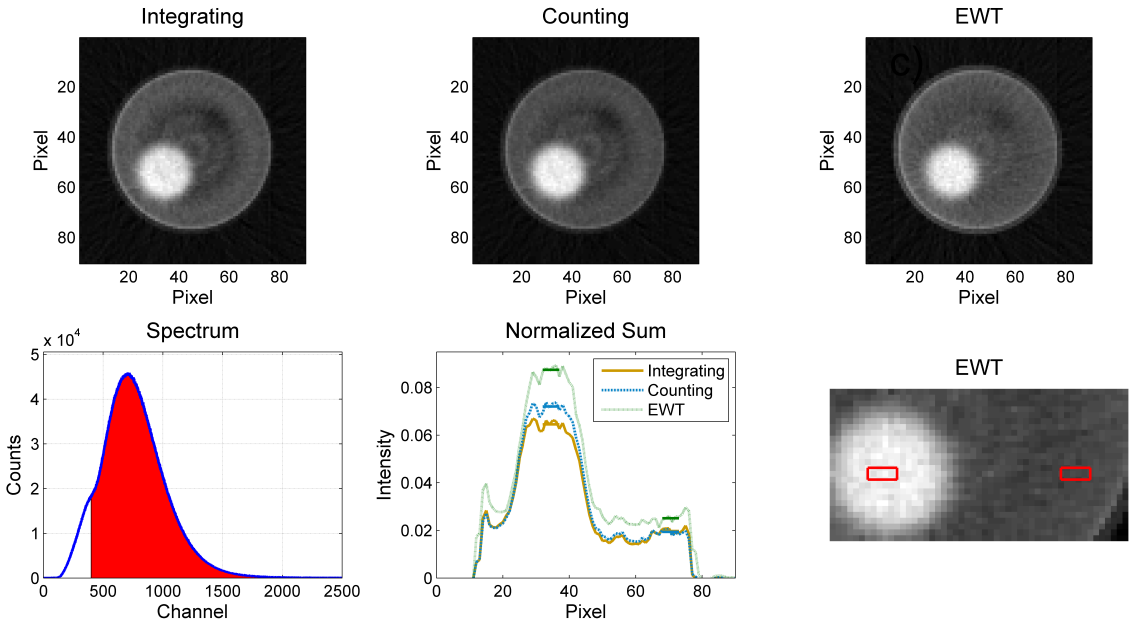

Figure 4.3: Top: Three types of cross-sectional images (integrating, counting and EWT) with the detail of the selected region for analysis in Bottom Right. Bottom - Left: Spectrum using the red area for the three reconstructions; Bottom - Middle: Line profiles of the selected regions to perform image analysis [90].

Whenever C_{enh} exceeds 1, the contrast of image A improved relatively to image B contrast. [90].

SNR of a ROI can be defined as:

$$SNR = \frac{\mu}{\sigma} \tag{4.3}$$

where μ is the mean intensity and σ the standard deviation of the intensity in the considered ROI [3]. The SNR enhancement between two different images, A and B, can be calculated as the ration between the respective SNR, SNR_A and SNR_B:

$$SNR_{enh} = \frac{SNR_A}{SNR_B} \tag{4.4}$$

As in contrast improvement, if SNR_{enh} is higher than 1, then an enhancement of SNR of image A relatively to B is verified [90].

CNR, also evaluated, can be calculated using:

$$CNR = \frac{C}{\sigma} \tag{4.5}$$

with C the contrast calculated using Equation 4.1 and σ the standard deviation of the back-

ground. Therefore, CNR enhancement can be determined using:

$$\mathrm{CNR}_{enh} = \frac{\mathrm{CNR}_A}{\mathrm{CNR}_B} \tag{4.6}$$

CNR enhancement can be analysed as contrast and SNR enhancement: if CNR_{enh} is greater than 1, a CNR improvement is verified from image A to image B [90].

An image contrast enhancement of 8% was verified when comparing the counting and integrating images. Between EWT and integrating images a greater enhancement of about 23% occurs. [90]

Concerning the SNR improvement, the same tendency is verified. Despite counting image having already an enhancement of about 10% relatively to the integrating image, the EWT image presents an image SNR about 22% higher than the integrating image. According to [76] EWT maximizes the image SNR.

The obtained value for CNR enhancement comparing counting and integrating images was about 11%, however the results were more evident between EWT and integrating images, in which an improvement of 31% was registered.

Table 4.1 summarizes the obtained results.

Table 4.1: Image quality improvement in terms of contrast, SNR and CNR parameters, comparing integrating images with counting and EWT images [90].

Integrating to	**Contrast Enhancement**	**SNR Enhancement**	**CNR Enhancement**
Counting	1.08	1.10	1.11
EWT	1.23	1.22	1.31

The MHSP based detector allowed to improve image quality using the energy information. Image enhancement was achieved in counting image, but the improvement was more evident in the EWT image. The enhancement between integrating and EWT images achieved in this work is slightly lower than the one reported by Shikhaliev et al in [34], in which also a calcium base material was analysed. In the same study, Shikhaliev et al achieved a CNR improvement of 63% for iodine and 13% for wax [34].

4.3 Multislice and 3D Reconstruction

The 2D-MHSP based detector was also used for multi-slice acquisitions and 3D reconstructions. The acquisition parameters were the same used to obtain the results of previous

sections, except for the acquisition time of each view and the slit dimension. Each view was acquired for 7 s with a slit aperture of $15 \times 25\,\mathrm{mm}^2$ placed in front of the detector window.

Multi-slice and 3D reconstructions were done with the PMMA phantom filled with chalk and air and filled with chalk and brass, in the 5 mm and 2 mm diameter holes, respectively. The cross-sectional images were reconstructed with 90×90 pixels from sinograms with 128 rays and 200 views. The cross-sectional images of the multi-slice acquisition were stacked in a 3D graphic. Then, to visualize a specific surface, a window of values representative of that surface was selected and the corresponding iso-surface is shown. Considering that the components' gray values are very different from each other, the selection of the window values was simplified. [90]

Figure 4.4 shows the cross-sectional images (top) and the 3D reconstruction (bottom) of the PMMA phantom with chalk and air.

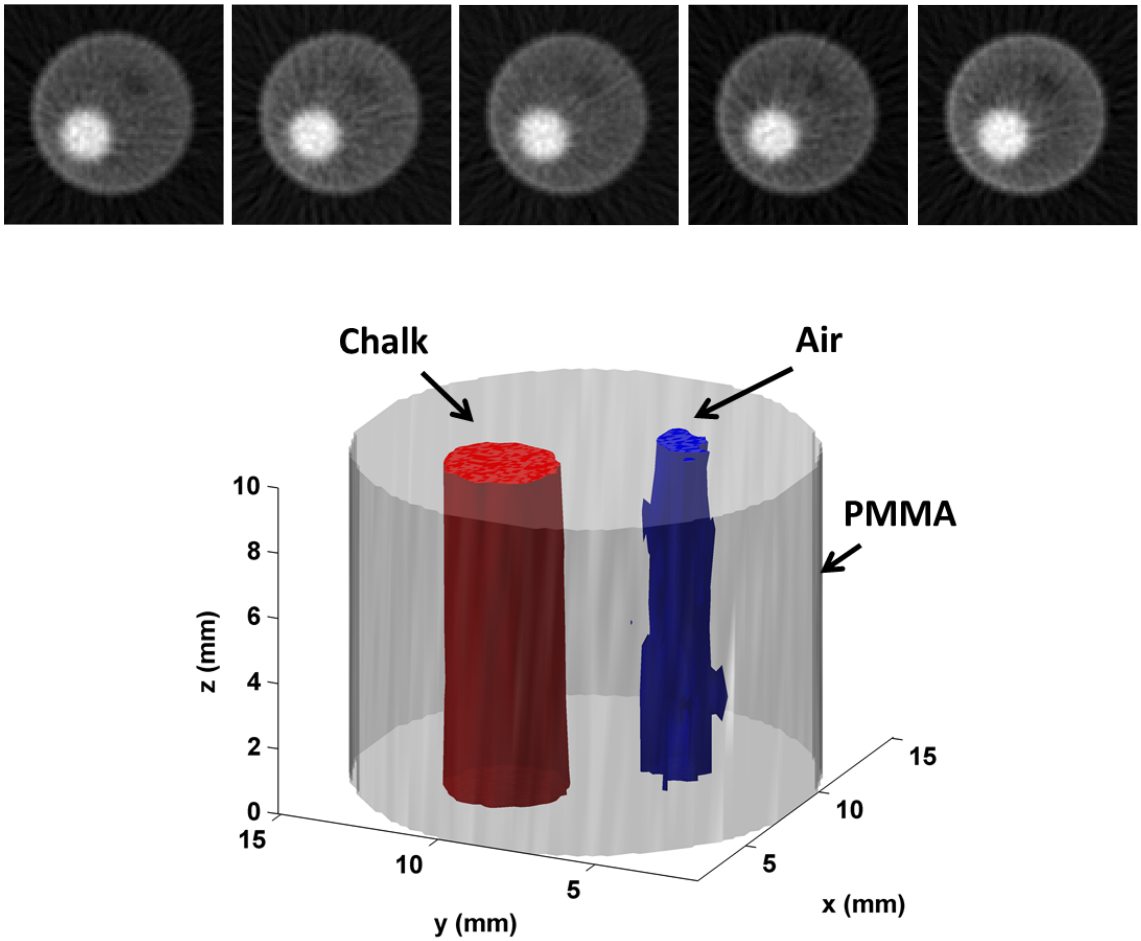

Figure 4.4: Sequence of cross-sectional images (top) and 3D image (bottom) of the phantom with chalk and air [102].

Each cross-sectional image shown in Figure 4.4 (top) corresponds to an object cross-

section thickness of 2 mm. Since the slices are contiguous and without overlap, the five images represent a cross-section thickness of 10 mm.

The 3D image of Figure 4.4 (bottom) was computed using the five slices shown previously and defining window values for PMMA, chalk and air surfaces, showing the corresponding iso-surfaces.

For the case of the phantom with chalk and brass filling the 5 mm and 2 mm diameter holes, the cross-sectional and 3D images are shown in Figure 4.5 on the top and bottom, respectively.

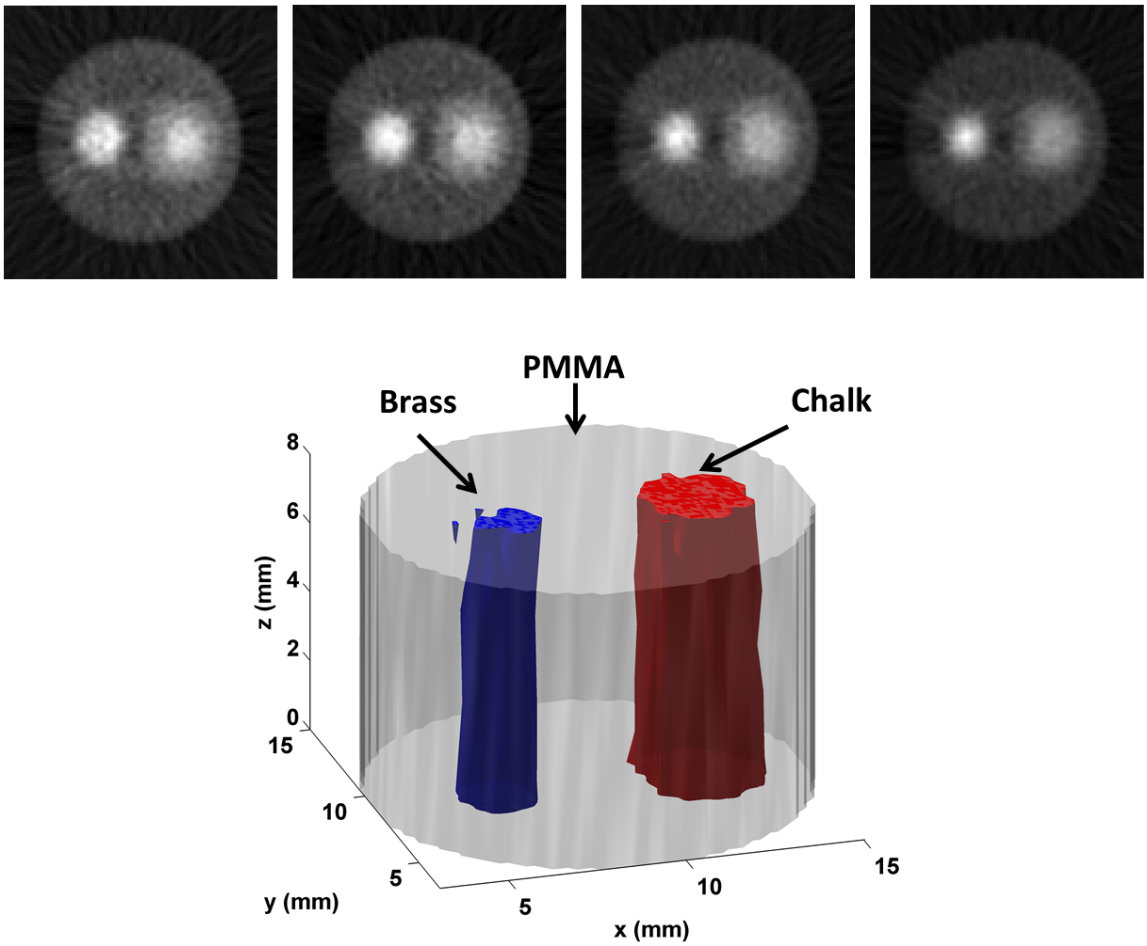

Figure 4.5: Sequence of cross-sectional images and 3D image of the phantom with chalk and brass based on the four cross-sectional images [102].

Contiguous slices without overlap were reconstructed. Each cross-sectional image shown in Figure 4.5 (top) corresponds to an object cross-section thickness of 2 mm, which means that the four images correspond to a cross-section thickness of 8 mm.

The 3D image of the PMMA phantom with chalk and brass shown in Figure 4.5 (bottom) was computed using the four slices of Figure 4.5 (top). The window values for PMMA, chalk

and brass surfaces, were chosen to show the corresponding iso-surfaces.

The cross-sectional images present beam hardening artefact, and on the PMMA phantom with chalk and brass images, misalignments of the centre of rotation relatively to the detector centre are also visible, leading to poor image quality. Image quality is also limited by the low statistics. Despite this, the PMMA, chalk, air and brass can be well distinguished in the images.

3D images show also good definition of all the surfaces in both cases. However, since the acquisition of the PMMA phantom with chalk and air has more statistics, the chalk rod is better defined in the 3D image. Also, in this acquisition the air rod has some small artefacts. In the second acquisition (PMMA + chalk + brass), the brass rod is more defined, comparatively to the air rod of the first one (PMMA + chalk + air), as expected, since in the cross-sectional images it can also be better distinguished from the PMMA (the gray value difference is greater).

4.4 Medipix2

A CT system using a Medipix2 detector was assembled at the Development Center for X-ray Technology of Fraunhofer Institute, in Fürth, Germany. This work was performed in the scope of the doctoral grant conceded by the Fundação para a Ciência e Tecnologia of Portugal for supplementary training activities in photon counting detectors for CT systems. The results obtained will be presented and compared with those of the developed MHSP detector.

The applied Medipix2 detector, assembled in a Quad geometry, has a 300 µm thick Si layer with an active area of $2.8 \times 2.8\,\mathrm{cm}^2$ in a total of 512×512 pixels with a pitch of 55 µm. It works in counting mode enabling a count rate of about 1×10^6 Hz/pixel and has two threshold levels for energy discrimination. [103, 104] The system was carefully aligned in the x and y dimensions and characterized.

For the energy resolution studies, the detector was irradiated with monoenergetic radiation obtained through excitation of specific materials, using an X-ray tube. The materials applied in the study were Zn, Zr, Mo, Sn and La. A threshold scan was performed for each monoenergetic radiation, which allowed performing an energy calibration, i.e., matching the threshold level with the energy value. An energy resolution of 23 % (at 8.64 keV) was achieved. [105]

For X-ray imaging, a magnification factor of 1.9 was set by defining a SDD of 36.6 cm and a SOD of 18.9 cm. A measure of the spatial resolution, for X-ray transmission imaging, was determined by placing a test pattern between the X-ray tube and detector. The test pattern consists of a phantom type 18d, which has from 0.5 to 20 line pairs per mm. An X-ray image of this phantom is shown in Figure 4.6 (left). The contrast between the absorbing wall and

air regions was measured in the X-ray transmission image for all the frequencies of line pairs, and the results are shown in Figure 4.6 (right). As expected, the contrast decreases as the

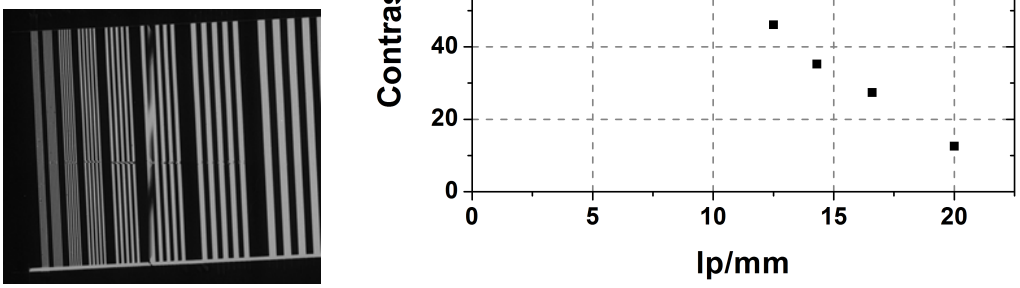

Figure 4.6: Letf: X-ray transmission image of the grid phantom used to measure spatial resolution; Right: Contrast between line pairs as a function of the line pairs per mm.

frequency of line pairs per mm increases. With the presented system configuration, 16 lp/mm were distinguished with a contrast of 27%. [105]

In case of CT images, in order to have a measurement of the minimum resolved detail, a phantom made of paper and Al foils with different thicknesses was produced. The thickness of the paper foils was constant (90 µm) and that of Al foils varied between 15 µm and 80 µm, allowing to create a low-high intensity pattern in the cross-sectional images. In Figure 4.7 (left) is visible a scheme and a CT image of the referred phantom. A study, shown in Figure 4.7 (right), similar to that done for X-ray transmission, was carried out. A thickness of 30 µm of Al was distinguished with 63% of contrast.

Two PMMA phantoms, the one described in Section 3.1.3 and another one with the same configuration but smaller dimensions, were imaged. The smaller phantom has a height of 20 mm, a diameter of 10 mm and its holes have 3 mm and 2 mm in diameter. For these acquisitions, a chalk rod and an aluminium rod were filling the 3 mm and 2 mm diameter holes, respectively. The low threshold level of the detector was set to 10 keV and the X-ray tube parameters were 50 kVp and 1 mA. The obtained X-ray transmission images are shown in Figure 4.8.

The 5 mm hole of the bigger PMMA phantom was filled with chalk and the other hole with air. Its X-ray transmission image (Figure 4.8 - left) acquired with Medipix2 detector shows the PMMA region well defined. The 2 mm diameter hole filled with air is also shown with less intensity. The chalk rod is visible with good contrast inside the other hole. It is

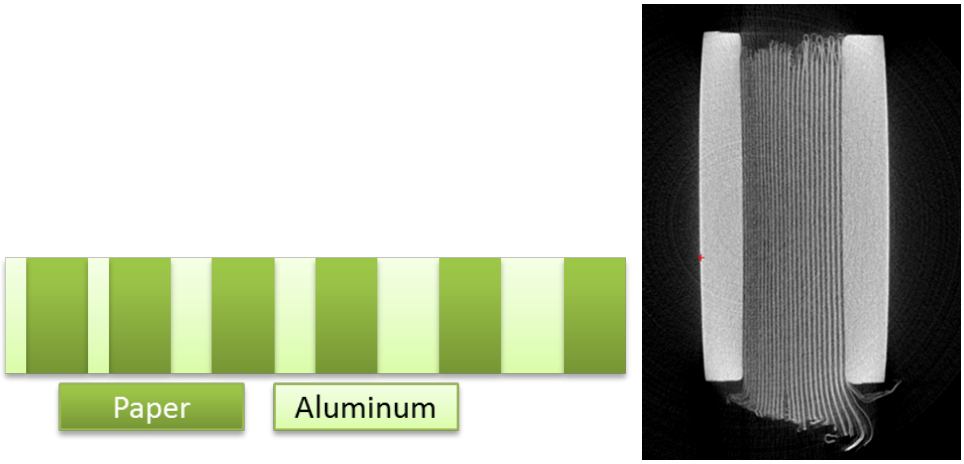

Figure 4.7: Scheme (Left) and cross-sectional image (Right) of the phantom produced to measure the minimum distance distinguishable with this system [105].

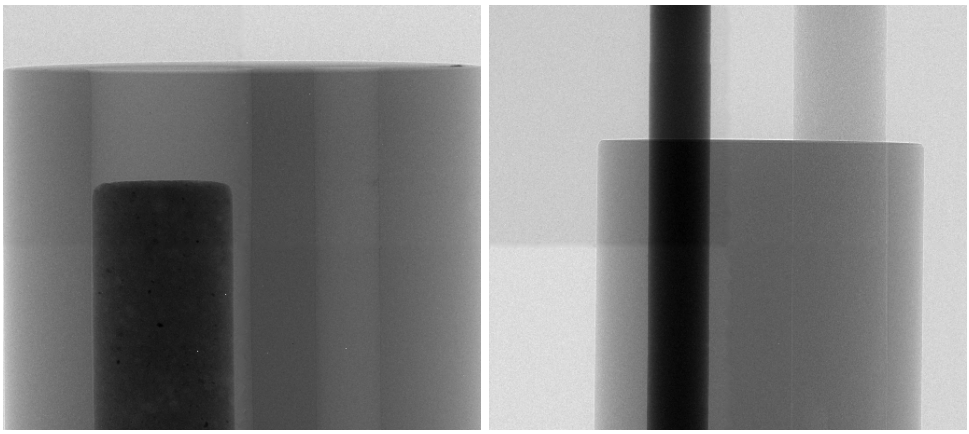

Figure 4.8: X-ray transmission images of the PMMA phantom described in Section 3.1.3 (Left) and of the smaller PMMA phantom (Right) [105].

interesting to note the lower and higher intensity regions shown in the chalk rod. As it will be shown later, these are also shown in the cross-sectional images. Another point to note is that the phantom dimensions and the magnification of the system made the projection of the phantom to be in the limit of the detection area of the detector. Concerning the image of the smallest phantom (Figure 4.8 right), both the chalk and the aluminium rods are well defined with good contrast and can be clearly distinguished. Generally, these images show good quality.

In order to acquire CT images free of artefacts due to system misalignments, a phantom with metallic spheres was used to align the system. The phantom was placed on the stepper motor, away from the rotation centre, in a position corresponding to the limit of an outer border of the detector. 36 views were acquired, which correspond to 10° of angular step.

Then, all the views were averaged and the result is shown in Figure 4.9. The resulting image

Figure 4.9: Average of the sphere phantom X-ray transmission images in a single image.

allows verifying the shift between the rotation and detector centres, the skew and determining the central plane. Therefore, knowing these misalignments makes it possible to correct them.

After alignment, cross-sectional images of the PMMA phantoms were acquired. The CT acquisitions were performed by acquiring 400 views with an acquisition time of 2 s per view, a low threshold level of 10 keV and an X-ray tube voltage and current of 50 kVp and 1 mA, respectively. Two cross-sectional images, one of each phantom, are shown in Figure 4.10.

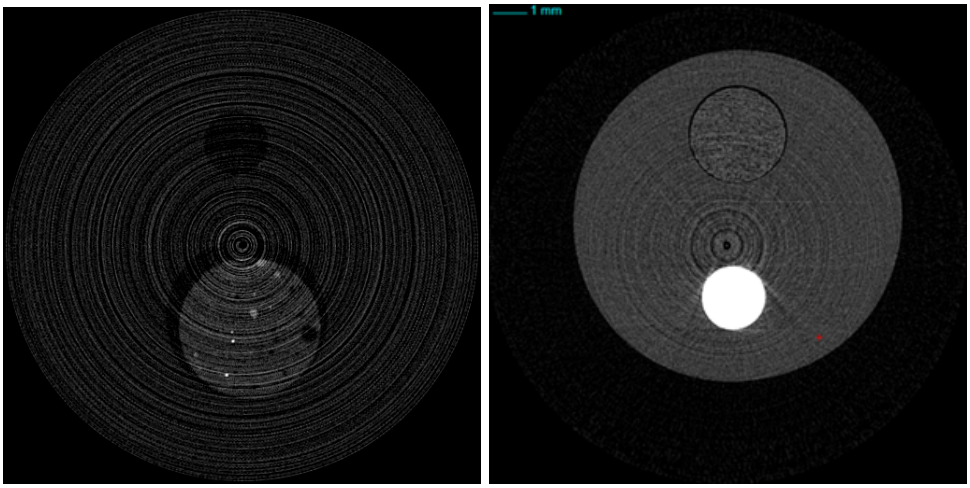

Figure 4.10: CT image of the PMMA phantom with chalk and air (Left) and of the smaller phantom with Al and graphite (Right).

Both CT images represent correctly the imaged objects and have good image quality. Despite some beam hardening and ring artefacts due to a high attenuating material and bad pixel responses, respectively, all the components are very well defined. In the image of the phantom with chalk and air, the ring artefacts are more evident. As referred in the analysis of the X-ray transmission images, inside the chalk rod region, some low and high intensity

areas are seen. The air rod is also perfectly defined. The image of the phantom filled with aluminium and graphite has less ring artefacts and, as expected, the aluminium rod region has an intensity greater than the remaining components.

Both 2D-MHSP and Medipix2 have an active area of 2.8 cm^2 and a different complexity in the electronics readout. 2D-MHSP has a simple and low-cost electronics readout based on four channels while Medipix2 has a dedicated readout for each pixel. Considering imaging capabilities, both detectors showed the imaged objects with reliability, which means that both are suitable for X-ray imaging applications. However, Medipix2 can provide a better spatial resolution (about 30 µm) than 2D-MHSP (about 130 µm), allowing images with better contours definition. This makes Medipix2 more suitable for applications that require high resolution images. On the other hand, 2D-MHSP can achieve higher energy resolution (13.5% at 5.9 keV) than Medipix2 (23% at 8.64 keV) which means that it is more suitable for applications that use energy information and therefore, must be precise, such as EWT.

CHAPTER

5

IMAGE RECONSTRUCTION GEOMETRY SIMULATION

The 2D-THCOBRA detector with an active area of $10 \times 10\,\mathrm{cm}^2$ has a sensitive area approximately 13 times larger than the 2D-MHSP based detector used previously. For this reason, the divergence angle of the X-ray beam increases significantly, up to a 2.7 factor. In order to assess if the parallel geometry algorithm for image reconstruction is still valid for the system using a $10 \times 10\,\mathrm{cm}^2$ detector, a basic simulation using Matlab® tools was performed. An important aspect to refer is that the tools used for simulation are very basic, since they do not allow to define all the parameters and variables in a CT system, such as X-ray spectrum or detector response. However the purpose was only to analyse the approximation to the parallel geometry and the effect of detector discharges in cross-sectional images.

5.1 Cylindrical Phantom with Two Cylindrical Holes

For this study, a phantom representing the attenuation coefficients of the PMMA phantom, described in Section 3.1.3, was generated in a Matlab® script, considering that no objects were filling the holes. An image of the generated phantom is shown in Figure 5.1.

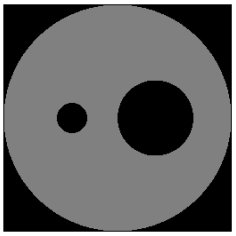

Figure 5.1: Matlab® phantom similar to PMMA phantom.

Using this phantom, fan projections were simulated according to the parameters used for acquisitions, such as the SDD, detector configuration and the number of views (limited by the minimum step of the stepper motor). Two sinograms, shown in Figure 5.2, were generated with and without Poisson noise. For this computation a SDD of about 180 cm (defined in pixels), a linear detector array and 400 views were considered. Poisson noise was added randomly to the projection images to simulate the real experimental conditions.

The sinograms of Figure 5.2 were used to reconstruct cross-sectional images using fan and parallel beam geometry algorithms, allowing a comparison between both algorithms. In this way, an evaluation of the approximation to parallel geometry used in this work is possible. Four images were obtained: two from the fan beam reconstruction algorithm and two from the parallel beam method, both using the sinograms with and without Poisson noise. The resulting images are shown in Figure 5.3.

These reconstructions provide an idea of the image that is possible to obtain using the PMMA phantom. The bottom images of Figure 5.3, reconstructed with parallel geometry algorithm, show a slightly unsharpened holes contour, essentially farther from the rotation

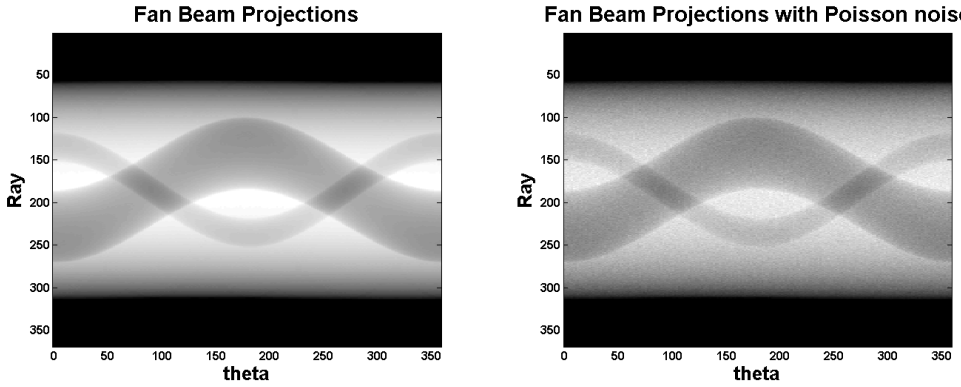

Figure 5.2: Sinograms generated using fan beam projection geometry without noise (Left) and adding Poison noise (Right).

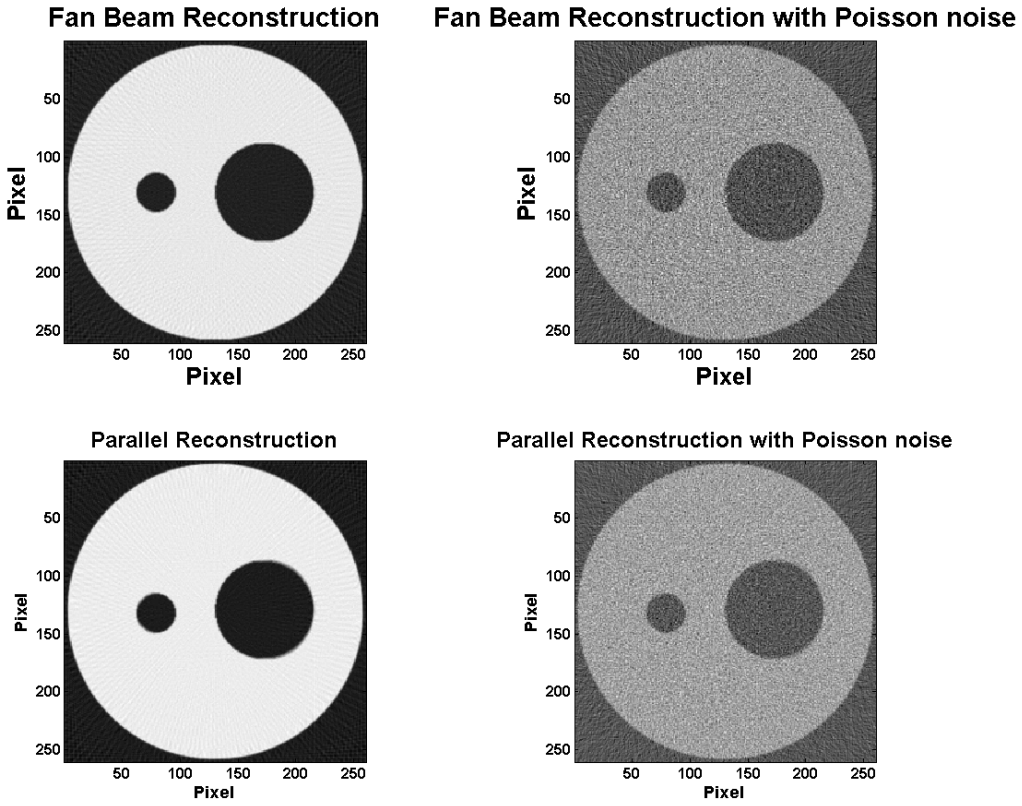

Figure 5.3: Top: Cross-sectional images reconstructed with fan beam algorithm from the non-noise sinogram (Left) and from the sinogram with Poisson noise (Right). Bottom: Cross-sectional images reconstructed using the parallel geometry algorithm from the non-noise sinogram (Left) and from the sinogram with Poisson noise (Right).

centre, comparatively to the top images (reconstructed using fan beam geometry algorithm). Despite this small, almost imperceptible, modification, the approximation to a parallel ge-

ometry algorithm can be carefully used, knowing that some artefacts may be expected. Also, in the images with Poisson noise, the intensity level of the PMMA phantom is much lower than in the images without noise. In Figure 5.4 the line profiles of the cross-sectional images

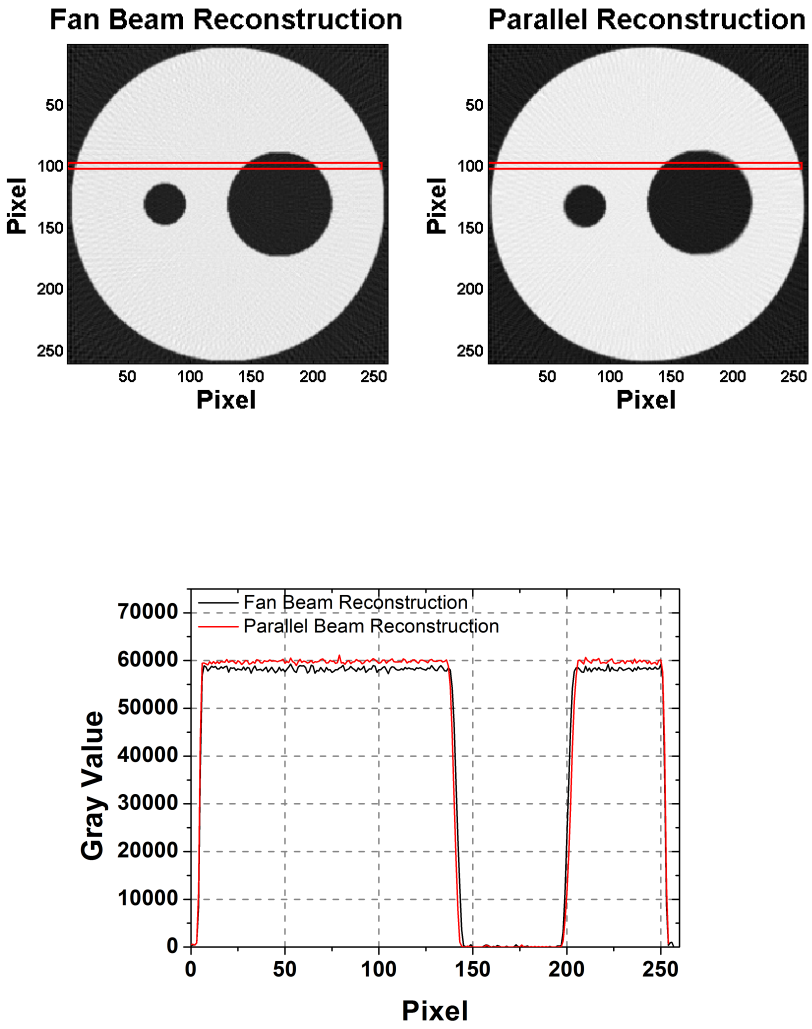

Figure 5.4: Top: Cross-sectional images marking the region used for the plot; Bottom: Profiles of the marked regions in cross-sectional images.

reconstructed with fan and parallel beam geometry algorithms are shown, also marking the selected region used for the plot. The result confirms the visual analysis, showing an almost imperceptible difference in the rod contours.

5.1.1 Influence of Discharges in CT reconstruction

MPGDs suffer discharges during their operation. To analyse the influence of discharges in the resulting image, CT reconstruction of sinograms where discharges were simulated was

done. During measurements, when the detector suffers a discharge and during the recovery time (some seconds) no events are recorded, leading to sinogram inconsistency, which can generate image artefacts [106, 107]. This situation was simulated, by observing the influence of the absence of data in some of the views in the reconstructed images. A high discharge frequency in a random pattern was defined in order to approximate the simulation to an experimental condition in which the detector was not stable. The defined discharge frequency is much higher than the occurred during the experimental acquisitions presented here. The cross-sectional images were reconstructed using the parallel geometry algorithm and the results are shown in Figure 5.5.

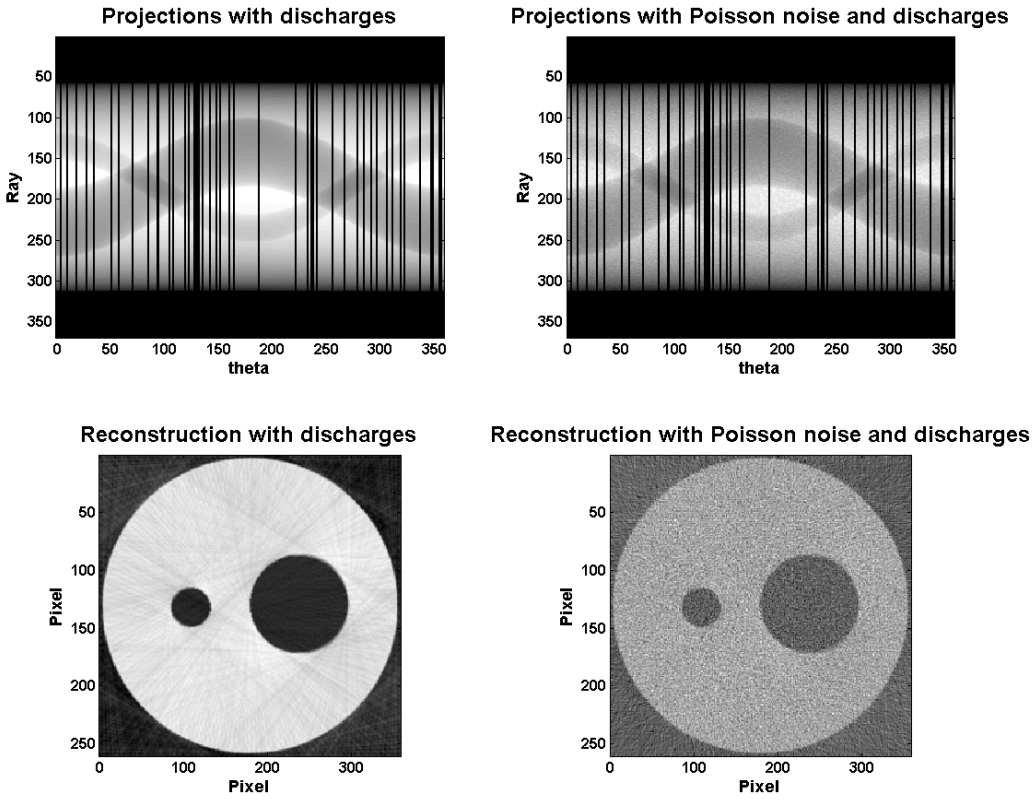

Figure 5.5: Top: Sinograms without (Left) and with Poisson noise (Right). Bottom: Reconstructed images using the sinograms.

Discharges, seen as black lines in the sinograms, introduce artefacts translated as stripes in the cross-sectional images, however in the cross-sectional image with Poisson noise added, the stripes are less evident, if at all, being cloaked by the noise.

5.2 Cylindrical Phantom containing Sharp Edges Objects

Another phantom designed with sharp edges (visible in Figure 5.6) was used to evaluate more thoroughly the reconstruction algorithm. Cross-sectional images of the phantom were

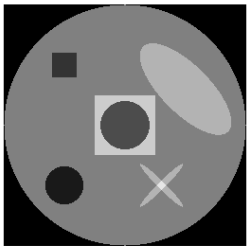

Figure 5.6: Matlab® phantom with sharp edges.

reconstructed using the fan and parallel beam algorithms without and with Poisson noise. The resulting images are shown in Figure 5.7.

To help in the image analysis, the regions of cross-sectional images (without noise) marked in red in Figure 5.7 were used to plot the respective line profiles, that are shown in Figure 5.8.

The cross-sectional images without Poisson noise (Figure 5.7 left) reconstructed using the parallel beam geometry algorithm show some artefacts compared to the ones reconstructed with the fan beam geometry such as blurred contours and double edges in the objects farther from the rotation centre. This means that the approximation to a parallel geometry introduces some reconstruction errors, however in the case where Poisson noise was added, the noise overlaps, prevailing and the referred artefacts are not so evident.

The line profiles of Figure 5.8 show some normal fluctuations in the intensity and have a relative intensity difference between the square, circle and background considered normal. The plotted graph confirms the points previously referred: the line profile of the image reconstructed with the fan beam algorithm shows a more marked intensity decrease in the regions of the square and circle, while the other line profile shows a step when the intensity decreases instead of a straight decreasing. The main question is: are these artefacts impairing the usage of the parallel geometry reconstruction algorithms? Probably not if the details to be reconstructed are properly rendered in the image.

5.2.1 Influence of Discharges in CT reconstruction

Cross-sectional images were also reconstructed using the parallel beam geometry after simulating discharges on the projections, as in the previous case, and the obtained images are seen in Figure 5.9.

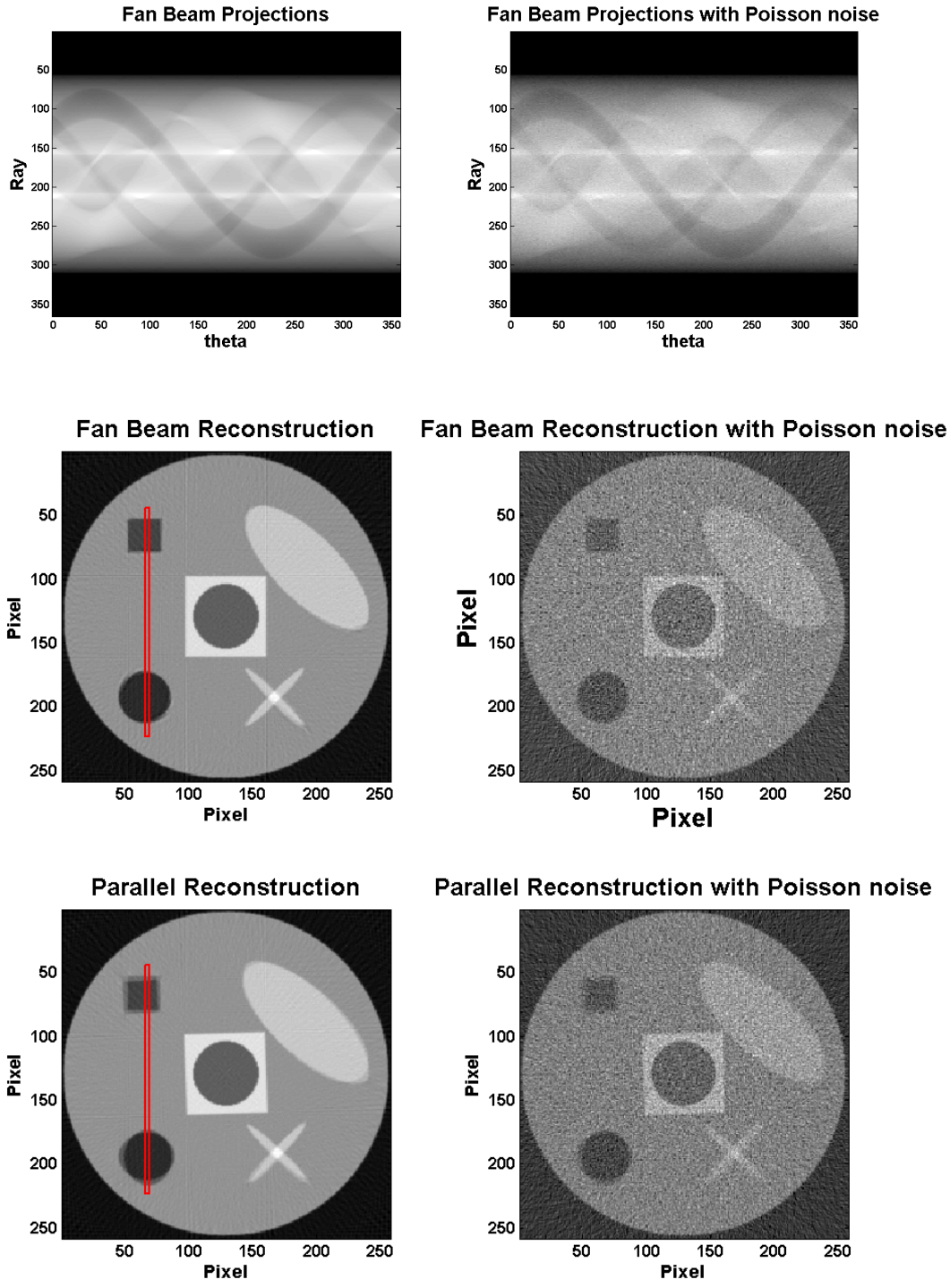

Figure 5.7: Top: sinograms generated using fan beam projection geometry without (Left) and with (Right) Poisson noise; Middle: cross-sectional images reconstructed using the fan beam geometry algorithm using the sinograms on the top image; Bottom: cross-sectional images reconstructed using the parallel beam geometry algorithm.

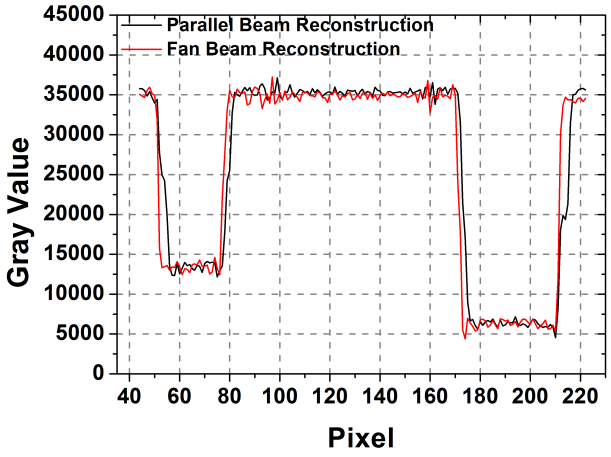

Figure 5.8: Line profiles of the regions marked in the cross-sectional images of Figure 5.7.

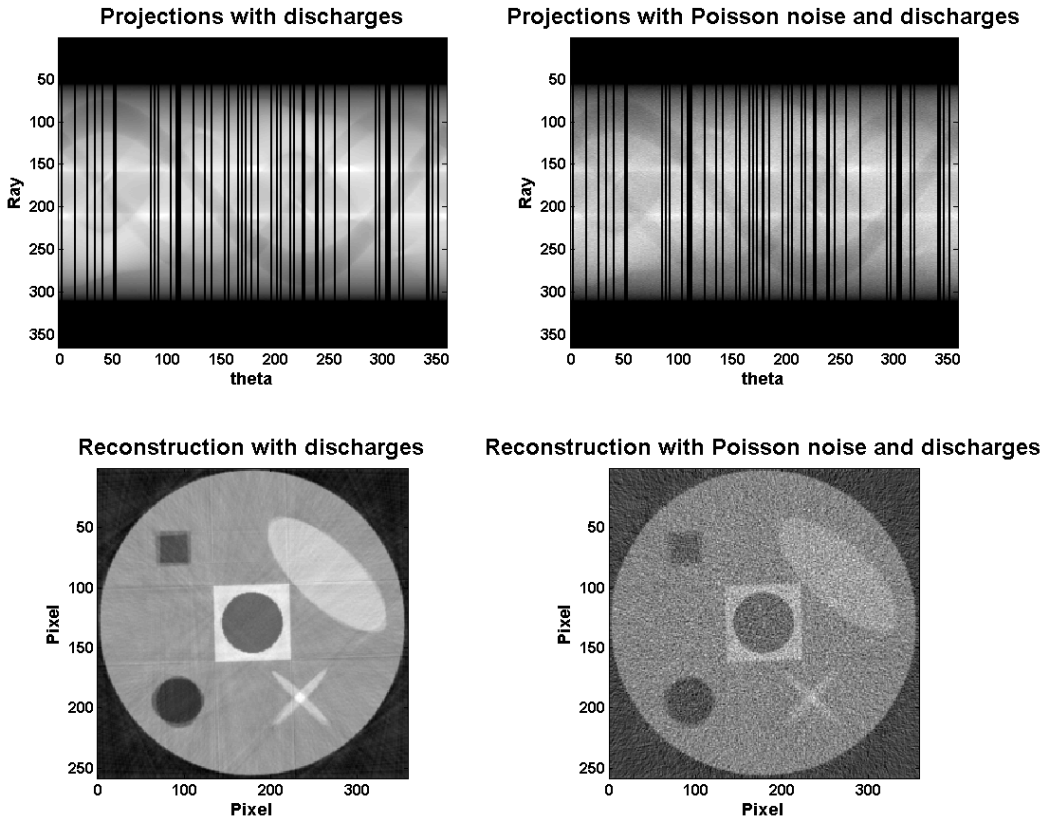

Figure 5.9: Top: sinograms with discharges without (Left) and with (Right) Poisson noise; Bottom: cross-sectional images of the respective sinograms.

Once again the not well defined contours and double contours are visible in the cross-sectional image without Poisson noise. Also, similarly to the previous case, white stripes

are introduced due to the views with discharges in the sinogram. The cross-sectional image obtained after adding Poisson noise to the projections does not show these artefacts so evidently, since they are cloaked by the noise.

Despite the image artefacts due to approximating the geometry to a parallel beam, simulations recently obtained related to the photoelectron range show interesting results. These simulations, done with Degrad software, show that a primary electron cloud generated from the photoelectron range in Ne/CH_4 can reach more than 3 mm (for a photon energy of approximately 13 keV) (Figure 7.6, p.126) [108], which means that after the photon interaction within the gas medium, the avalanche charge can be spread, and consequently detected, up to 3 mm away from the point of interaction, as explained in Section 2.2.3. Therefore, any approximation to a specific geometry will not truthfully represent the X-ray photons path (beam geometry). In this case, a model to describe this behaviour should be developed and applied, being aware that the more adequate model would probably be statistical. However, the development of such a model was not in the scope of this work and the applied model, although an approximation, provides reliable cross-sectional images.

CHAPTER

6

CT SYSTEM USING A 2D-THCOBRA DETECTOR WITH A THGEM

The DRIM group studied the 2D-THCOBRA detector with a THGEM in terms of gain, energy and spatial resolutions. The methods used to perform these studies are described in [75]. It was found that the detector allows a gain of 2.5×10^4 and an energy resolution of 20.3% (FWHM at 8 keV). The spatial resolution is 2.29 mm and 2.73 mm for anodes and tops directions, respectively, with the detector being irradiated with an X-ray tube voltage of 20 kVp. These values are limited by the photoelectron range in the gas medium, as it will be explained. [75]

CT X-ray imaging studies were done with the 2D-THCOBRA detector with a THGEM pre-amplification stage. Cross-sectional images of the PMMA phantom with chalk and brass and cross-sectional images of the sea snail were acquired.

6.1 Multi-slice and 3D Reconstruction

The PMMA phantom was imaged with an X-ray tube voltage and current of 22 kVp and 324 µA, respectively. For the reconstruction of cross-sectional images of the PMMA phantom with its holes filled with chalk and brass, 400 views were acquired, each with 5 s of acquisition time. The SDD and the SOD were 114 cm and 93 cm, respectively, achieving a magnification factor of 5.4. A collimator with $10 \times 3\,\mathrm{cm}^2$ was used to limit the irradiated area of the detector.

For image reconstruction, the sinograms were constructed with 256 rays and the cross-sectional images with 190×190 pixels. The number of pixels allows a good compromise between the spatial resolution and the SNR of the image, considering the detector response function and the image noise. This compromise was applied in all the acquisitions performed with the THCOBRA based detector operating in Ne/CH_4. The first attempt of reconstruction originated the image in Figure 6.1 (top-left), which is clearly not well reconstructed: none of the components is well defined. The Matlab® routine developed for CTRADIX to evaluate the deviation of the rotation and detector centres was used to determine if there was a shift and correct it. A shift of 16 pixels was found and the respective correction was performed. The resulting image is shown in Figure 6.1 (top-right). In this image all the components can be identified. Both images show the region used to plot the profiles shown in Figure 6.1 (bottom).

The line profiles visible in Figure 6.1 show what is clearly seen in the cross-sectional images before alignment, the brass rod is not distinguished from the PMMA and after alignment a well defined rod is visible. The variation of the gray value in the non-aligned image does not have an evident peak in the region of the brass rod, it has a slight increase in the intensity, but it is not clearly distinguishable from the PMMA. On the other hand, the line profile of the image reconstructed after aligning the sinogram shows a peak very well distinguished from the PMMA. Figure 6.1 shows an evident recovery of an acquisition which initially could not

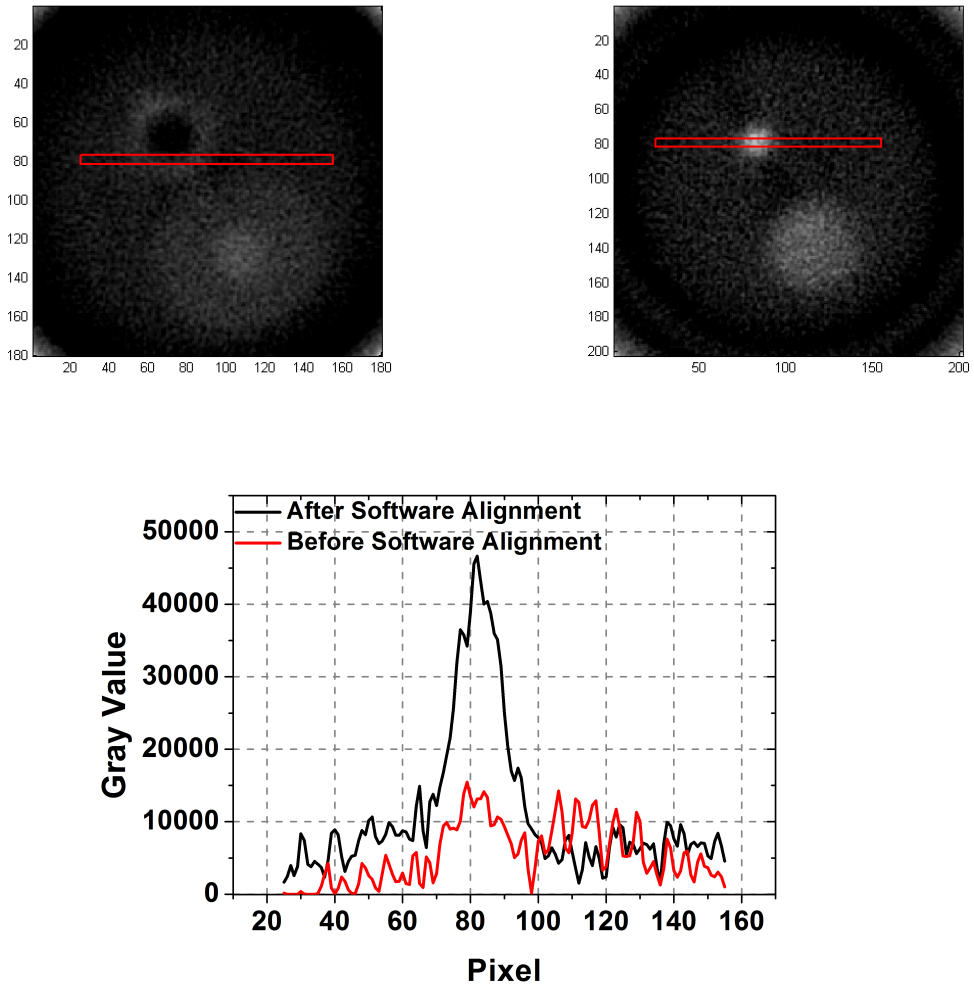

Figure 6.1: Cross-sectional images of the phantom with chalk and brass before (top-left) and after (top-rigth) software alignment. Bottom: line profiles of the marked regions shown in the cross-sectional images.

be well reconstructed. The components that could not be identified initially, after correcting the deviation of the centres, are well defined.

A multi-slice reconstruction, obtaining 5 cross-sectional images, was done. A slice thickness of 6 mm was achieved, since the slices were contiguous and without overlapping. The resulting cross-sectional images and the respective sinograms are shown in Figure 6.2.

Generally, the images show the scanned objects, however, with some visible noise. The sinograms show two discharges that occurred during the acquisition but the components (PMMA cylinder, chalk and brass rods) can be well distinguished with good contrast, despite the noise. The cross-sectional images show also all the components with good contrast. The relative intensity between the components is considered adequate: the brass rod is the more dense component and is the more intense object in the image; the chalk rod is less intense

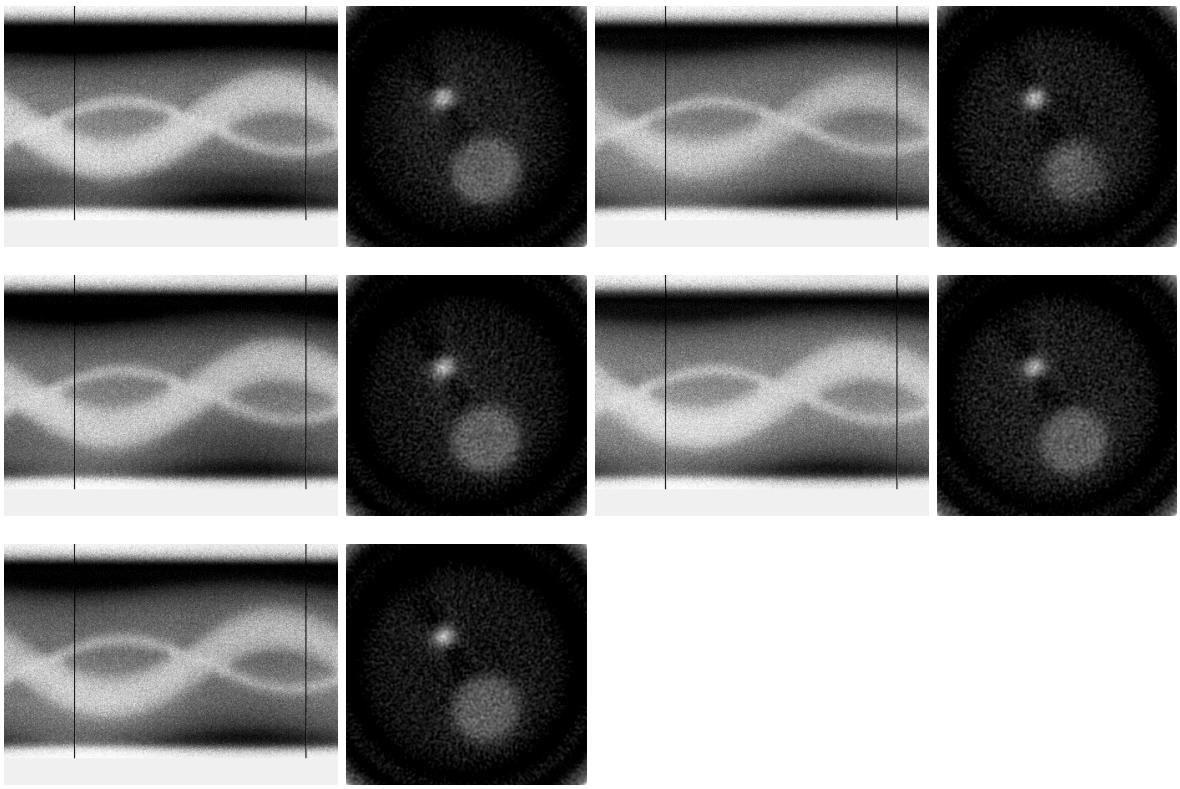

Figure 6.2: Sinograms of the PMMA phantom with chalk and brass (left) and the corresponding cross-sectional images (on the sinograms right).

than brass and more intense than PMMA, which is in accordance with its density. The CT images show also severe beam hardening artefacts near the brass rod. Another aspect to note is that the phantom was not centred with the detector centre which is seen both in the sinograms and in the cross-sectional images. Fortunately, this deviation could be successfully corrected, as already shown.

The cross sectional images presented in Figure 6.2 were stacked up to obtain a 3D image of the phantom with chalk and brass, shown in Figure 6.3.

The 3D image achieved with this acquisition could map the surfaces of all the components. The contours are slightly unsharpened, which was expected after analysing the cross-sectional images. It is interesting to note that the beam hardening effect, shown in the cross-sectional images, is also seen in this image: the PMMA surface is seen from the brass rod until the external PMMA surface.

Images corresponding to the same cross-sections represented in Figure 6.2 were reconstructed using a flat field correction. A flat field acquisition was performed in the same conditions of the phantom's and was used to correct the non-uniform response of the detector. An image of the flat field acquisition can be seen in Figure 6.4, in which the line profiles and the regions used to plot them are shown.

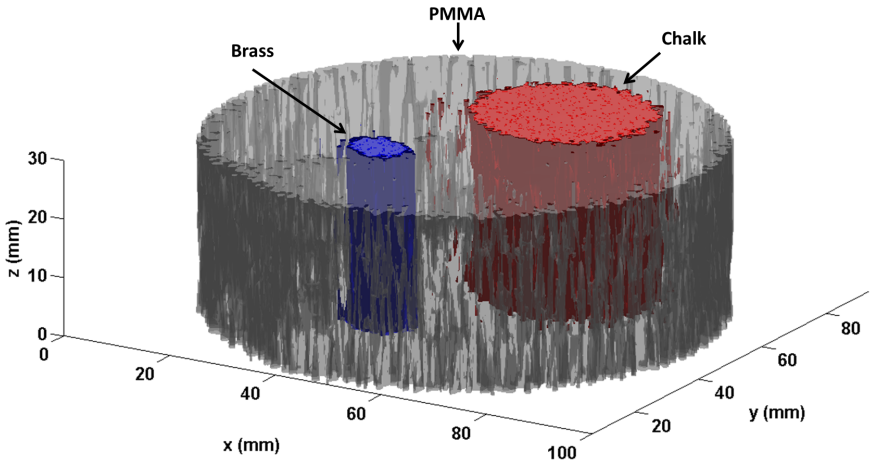

Figure 6.3: 3D image of the PMMA phantom with chalk and brass computed using the acquisitions done with the detector with the two structures.

The flat field image shows a more or less uniform intensity despite the high intensity arc that can be seen from the image corners up to the centre. Besides, in the centre a region with higher intensity is seen. Both line profiles marked with red show this arc, the intensity increases at the centre and in the horizontal line profile the intensity increases gradually up to the centre, which corresponds to what is seen in the image. The horizontal line profile marked in blue shows only the central region with higher intensity, and the remaining profile can be considered uniform with some fluctuations. The flat field image clearly demonstrates the non-uniform detector response. The images obtained after performing this correction are shown in Figure 6.5.

The cross-sectional images reconstructed after flat field correction show better general image quality than the ones without correction, especially in terms of uniformity, which is the purpose of this action. The image components, essentially the PMMA, are much better defined than in the images without correction. The images also show the same beam hardening artefact as the previous. To easily compare the effect of applying the flat field correction, the third slice reconstruction is shown side-by-side in Figure 6.6. Besides the qualitative visual analysis, the SNR enhancement (studied as described in Section 4.2) was evaluated between the cross-sectional images with and without flat field correction in the third slice. The region used to perform the measurements is marked on Figure 6.6. An improvement in SNR of 80% was achieved after correcting the images with a flat field image.

The cross-sectional images obtained after flat field correction were also used to compute a 3D image, shown in Figure 6.7.

The improvement in image quality after flat field correction is transferred to the 3D image. The PMMA cylinder is much more uniform and its surface is better defined in the 3D

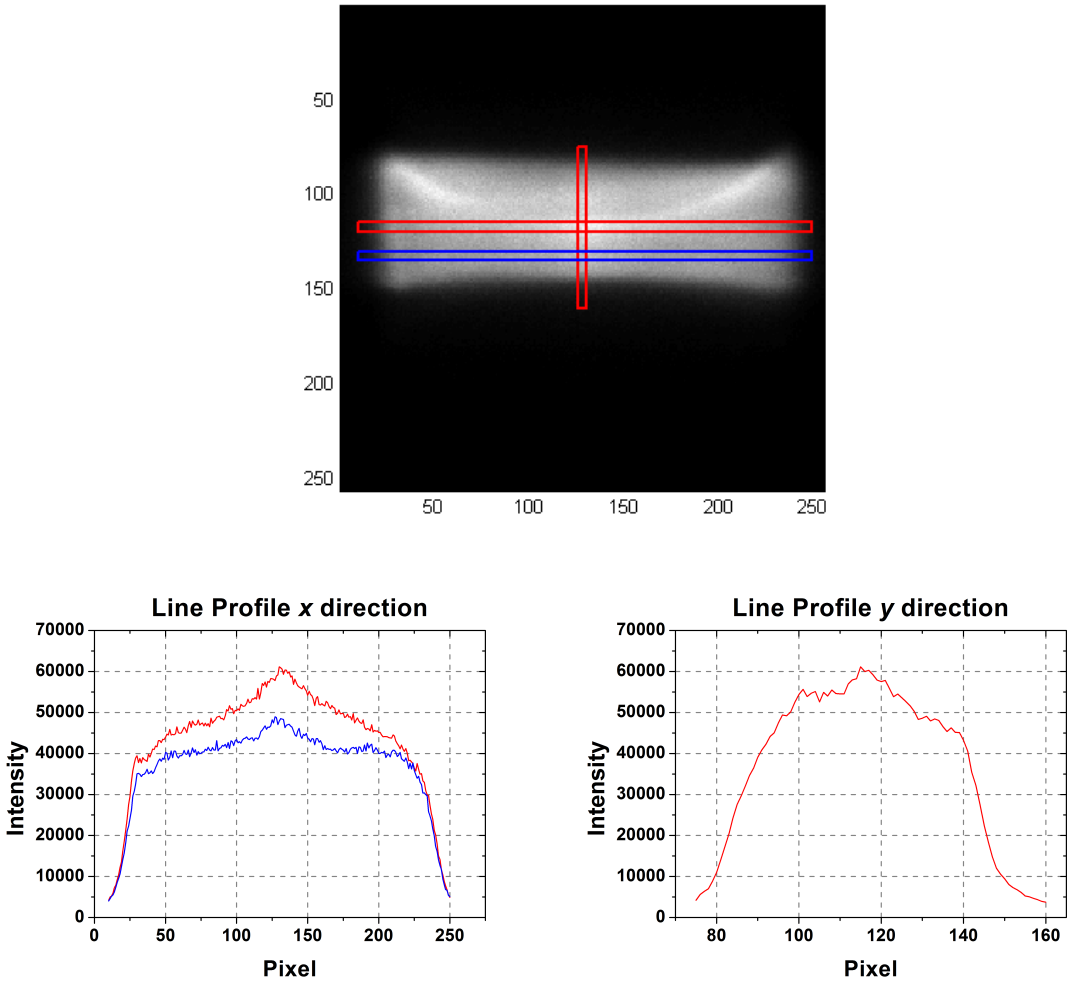

Figure 6.4: Top: Flat field image used to correct the non-uniform response of the detector, marking the regions in which the line profiles were plotted. Bottom: Line profile in x (Left) and y (Right) directions.

graphics. The chalk and brass rods are similar to the previous image and the beam hardening effect is also clearly visible in this image.

A sea snail was imaged with an X-ray tube voltage and current of 35 kVp and 12 µA, respectively, and the same collimator of the previous acquisitions was placed in front of the detector window. 400 views were acquired with an acquisition time of 10 s each. The SDD was set to 114 cm and the sample was placed as close to the detector as possible, therefore no magnification factor was defined. Seven cross-sectional images were reconstructed with a slice thickness of 2.9 mm each (considering that continuous slices without overlapping were defined). The achieved images are shown in Figure 6.8.

Both sinograms and cross-sectional images show visible noise. Despite this, the sea snail

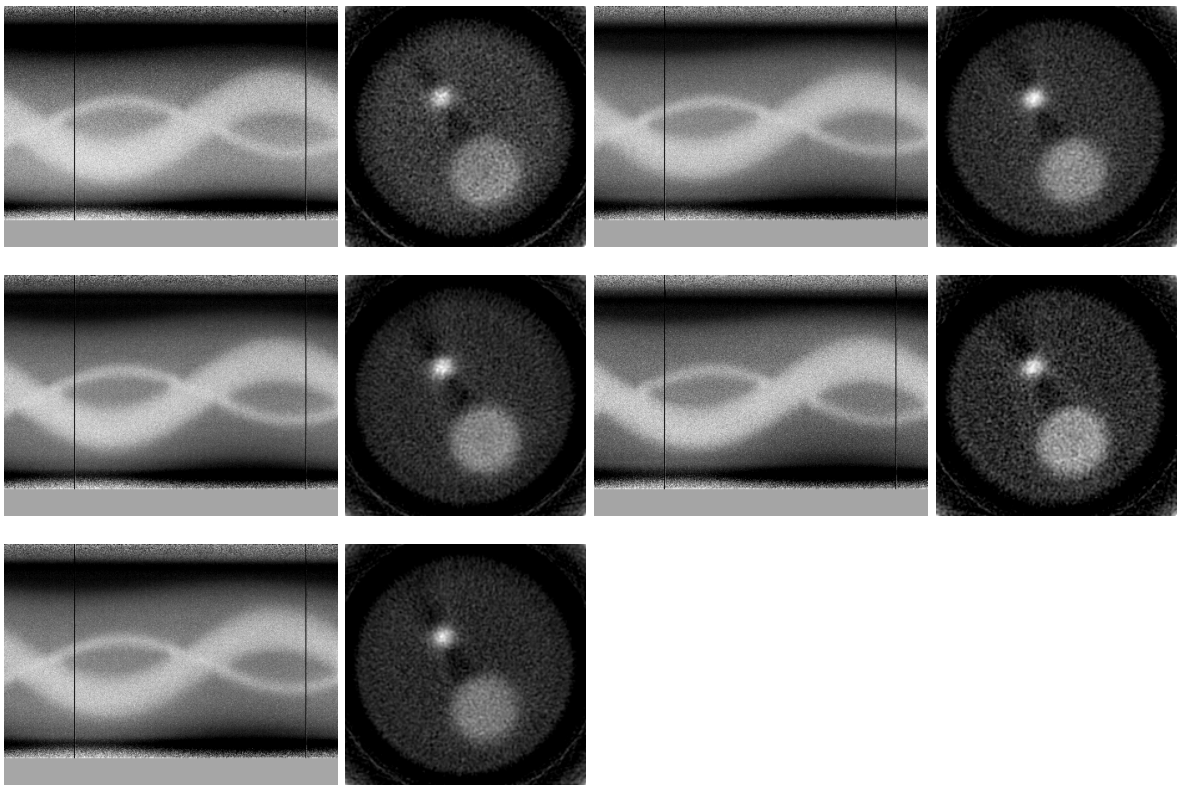

Figure 6.5: Sinograms of the PMMA phantom with chalk and brass (left) and the corresponding cross-sectional images (on the sinograms right) reconstructed using flat field correction.

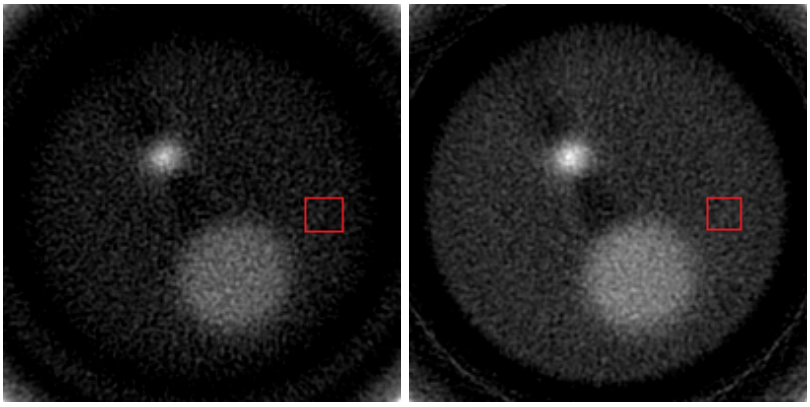

Figure 6.6: Third slice of the acquisition of the PMMA phantom with chalk and brass without (left) and with (right) flat field correction, marking the region used to evaluate the SNR.

and its structures can be distinguished in the sinograms and in the cross-sectional images. The sinograms show that two discharges occurred during acquisition, one with more significance than the other. The cross-sectional images show partial volume artefacts. To eliminate this

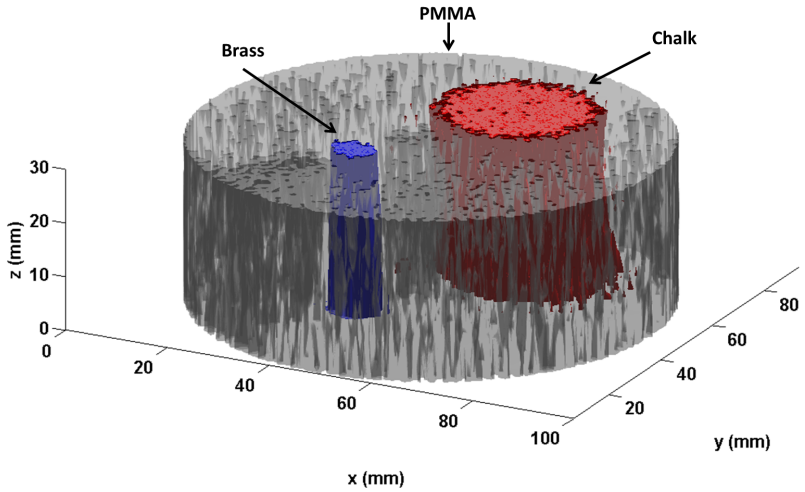

Figure 6.7: 3D image of the PMMA phantom with chalk and brass computed using cross-sectional images reconstructed after flat field correction.

effect, thinner slices should be reconstructed. However, for this acquisition, due to the limited statistics, the defined number of slices seem to reach a good relation between the image quality and slice thickness. The limits of spatial resolution also limit the image quality in terms of contour definition. Nevertheless, the sea snail exoskeleton is visible from the columella up to the apex.

The cross-sectional images of Figure 6.8 were used to compute a 3D image of the sea snail by defining a window of values representative of the sea snail shell. After computation, some perspectives of the obtained image were stored and are shown in Figure 6.9.

In the front view, the sea snail aperture can be seen, however the aperture should be more pronounced and go further into the sea snail. The sea snail apex can also be seen but not completely distinguished from the sutures near it. These aspects are due to the partial volume artefacts seen in the cross-sectional images. In the 3D oblique view the bigger sutures and the spiral shape of the sea snail shell are visible. The bottom view shows the interior cavity, not so large as it should be, but once again, this is due to the partial volume artefacts, that could be reduced with a smaller slice thickness if the acquisition had more statistics. The 3D images show some granularity and even though the sea snail shell surface is shown, some irregularities in the sample surface are visible, and partial volume artefacts limit the definition that was possible to achieve.

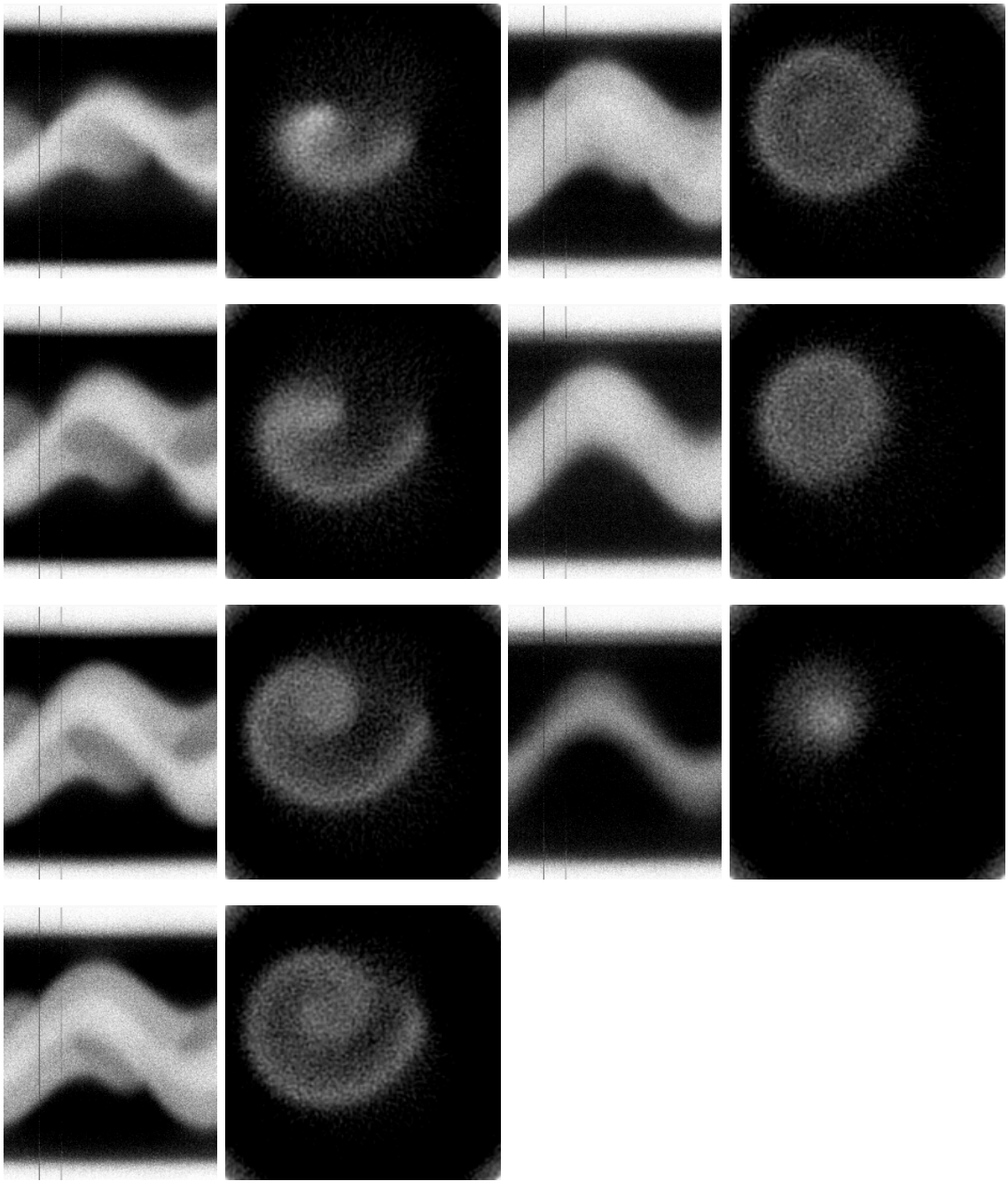

Figure 6.8: Sinograms of the sea snail and corresponding cross-sectional images.

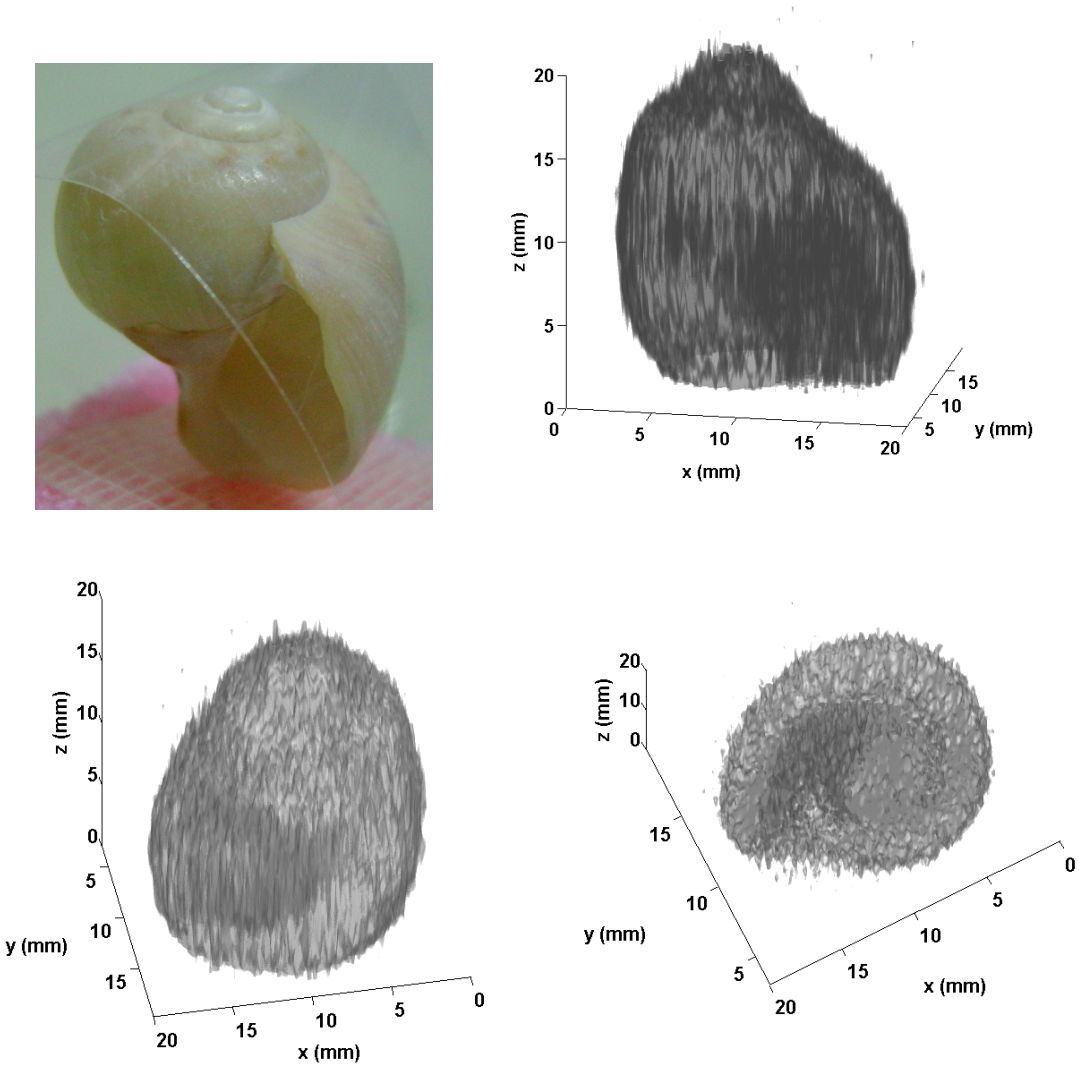

Figure 6.9: Photo and 3D images of the sea snail in different perspectives: front, oblique and bottom views.

CHAPTER

7

CT SYSTEM USING A 2D-THCOBRA BASED DETECTOR FILLED WITH NE/CH_4

The development of a 2D-THCOBRA structure with thinner anode strips to improve its performance lead to a simpler detector configuration, using only a 2D-THCOBRA structure inside the detector, as described in Section 3.1.4.2. Several characteristics of the new 2D-THCOBRA based detector filled with Ne/CH_4 (95/5) were studied for imaging purposes [109]. The studies made of the charge gain as a function of the applied voltage between the top electrodes and the cathodes and between the cathodes and the anodes, the count rate, the stability, the energy resolution as a function of the applied voltage and the spatial resolution as a function of the photon energy are presented below.

7.1 Charge gain

The charge gain as a function of the applied voltage to the detector was measured on the top and on the anode electrodes, in order to evaluate if the charge gain was enough to achieve the SNR of the output pulses for imaging purposes.

To determine the absolute value of the charge gain, the readout electronics was calibrated by sending a known pulse to the pre-amplifier and measuring the response using a 6.8 pF capacitor with 3.07% tolerance and the BNC PB-5 Precision Pulse Generator. A multi-channel analyser (MCA) 8000A from Amptek was used to measure the amplifier output pulse allowing to establish a relation between the MCA channel and the charge. Thus, since the charge is proportional to the deposited energy in the detector, a relation between the deposited energy and the MCA channel can be established. [75] Figure 7.1 shows a scheme of the experimental instrumentation used for calibrations.

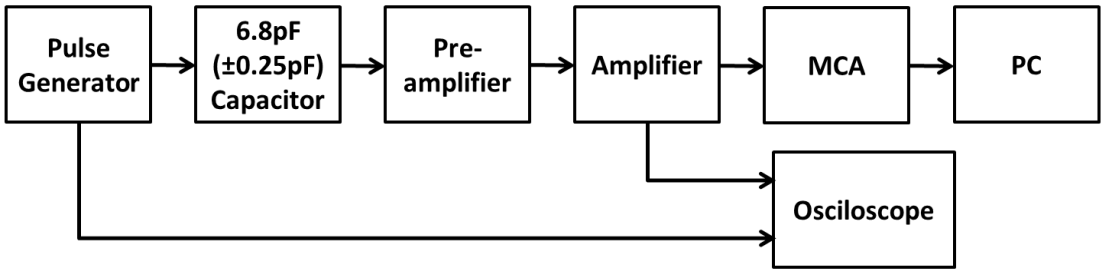

Figure 7.1: Scheme of the experimental apparatus of the gain calibration measurements for the THCOBRA detector with $10\times10\,cm^2$ active area.

The charge gain is the ratio between total and primary charges. Primary charge is calculated using the energy of the incident radiation and the W-value (29 eV per electron-ion pair [48]). After calibration, the total charge can be determined knowing the MCA channel. Then irradiating the detector with a known energy source, such as fluorescence radiation or a radioactive source, it is possible to calculate the primary charge and, measuring the detector response, to determine the total charge.

For acquisitions, a lead collimator with a 4 mm diameter hole was placed in front of the detector window. The detector was irradiated with fluorescence Cu K-lines generated through X-ray tube irradiation of a Cu target. A standard Gaussian was fitted to each pulse height spectrum acquired for each applied voltage and its centroid was obtained. [109]

For X-ray imaging applications it is very important to achieve a high gain since it allows good SNR of the pulses leading to a better detector performance, in terms of spatial and energy resolutions. Since the interaction position is determined using both anode and top signals, an evaluation of the gain in both electrodes is essential.

Figure 7.2 shows the obtained gains for anode and top electrodes as a function of the applied voltage between the cathode and top strips (V_{CT}) and between the anode and cathode strips (V_{AC}).

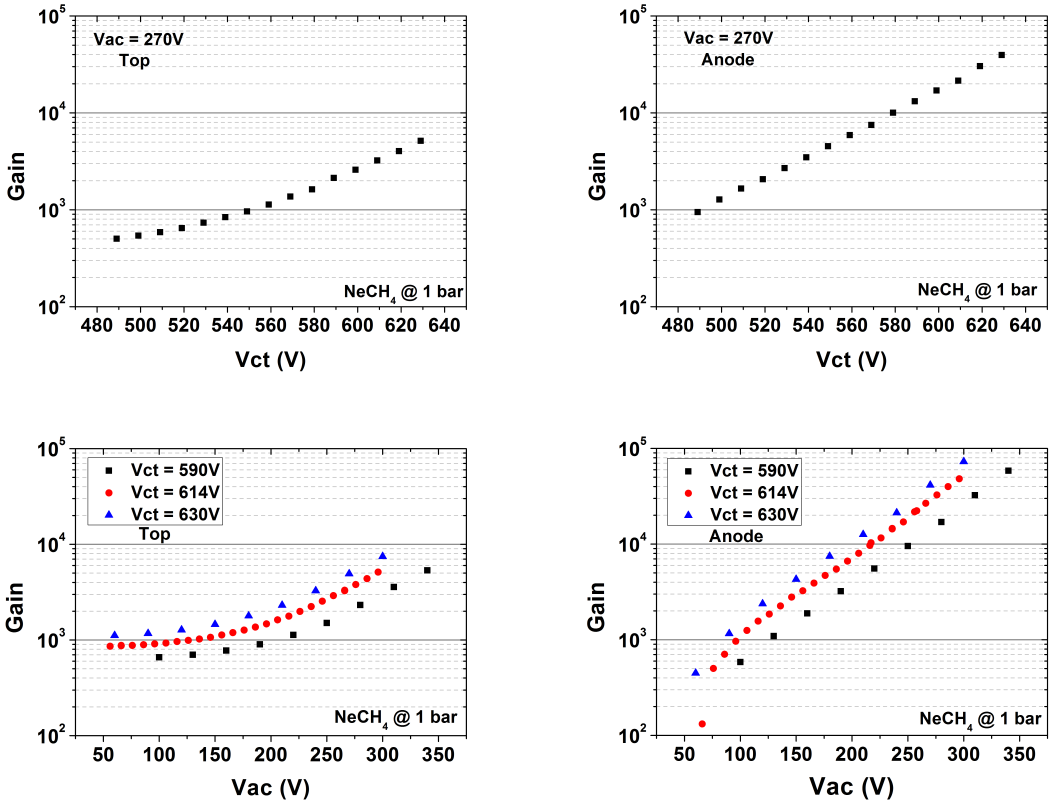

Figure 7.2: Gain as a function of the V_{CT} (Top) and V_{AC} (Bottom) applied to the structure, measured on top (Left) and anode (Right) electrodes [109].

As expected, the higher the applied voltage (both V_{CT} and V_{AC}) the greater the charge gain following an exponential behaviour with the increasing voltage, characteristic of the Townsend avalanche. Anode electrodes can achieve higher gains than top electrodes, since the top signal is induced by the movement of the charge near the anode strips. [109, 75]

For a fixed V_{CT}, the maximum gain achieved in the top electrodes was close to 8×10^3

and in the anode about 8×10^4 for a V_{CT} value of 630 V and a V_{AC} value of 300 V. Setting V_{AC} to 270 V, maximum gains of about 5×10^3 and 4×10^4 were achieved on top and anode electrodes, respectively, both for a V_{CT} value of 640 V. The measured gains allow a good pulse SNR, therefore are high enough for X-ray imaging. [109]

The provided gain is higher than the gain achieved with a single THGEM detector (4×10^4) and in the order of the one reached with a double THGEM detector (2×10^5) [72]. However, the 2D-THCOBRA detector presents a simpler solution since it has only one structure and does not need a readout plane for position discrimination for X-ray imaging purposes.

7.2 Energy Resolution

Since the photon energy can be used for image reconstruction, it is important to know how precise the energy information is. In order to study the energy resolution as a function of V_{AC}, a Cu target was irradiated by the X-ray tube, as in charge gain studies discussed above, and a spectrum was stored for each value of V_{AC} considered. A Gaussian function was fitted to each pulse height distribution and the energy resolution was calculated as described in Section 2.3.2. The obtained results are shown in Figure 7.3. [109]

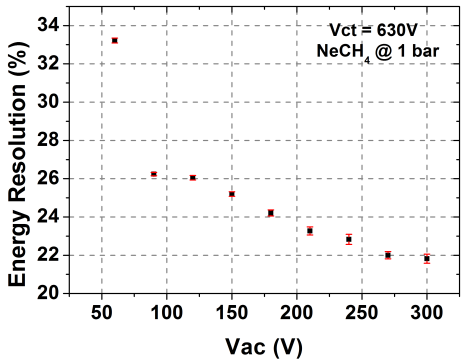

Figure 7.3: Energy resolution as a function of V_{AC}, with the detector chamber filled with Ne/CH_4 [109].

As expected, the energy resolution improves as the V_{AC} increases. This is mainly due to the higher charge gain and, consequently, greater SNR, which makes the statistical fluctuations less significant [5]. The best energy resolution of 22% (FWHM at 8 keV) was achieved for a V_{AC} value of 300 V. [109]

The reached energy resolution is better than the one achieved for a single THGEM detector (30% FWHM at 5.9 keV) operating in the same gas medium [72]. The previous 2D-THCOBRA detector (with the THGEM) gives a better value for the energy resolution (20.3% - FWHM - for the same energy).

7.3 Count Rate Capability and Time Stability

The gain as a function of the count rate per mm^2 and the gain as a function of time were studied in order to evaluate the detector count rate capability (without significant gain variation) and stability over time. For these studies, the detector was irradiated with the X-ray tube through a hole collimator of 500 µm in diameter. [109]

For the count rate studies, the X-ray tube current was increased gradually. A spectrum for each exposure parameter was stored and its peak amplitude was recorded. Concerning the stability study, the X-ray tube current was set to a constant value providing a count rate of about 2×10^6 mm^2. A spectrum was acquired at each two minutes during 1 h 30 min, with an acquisition time of 30 s. [109]

Figure 7.4 shows the obtained results for these performance parameters.

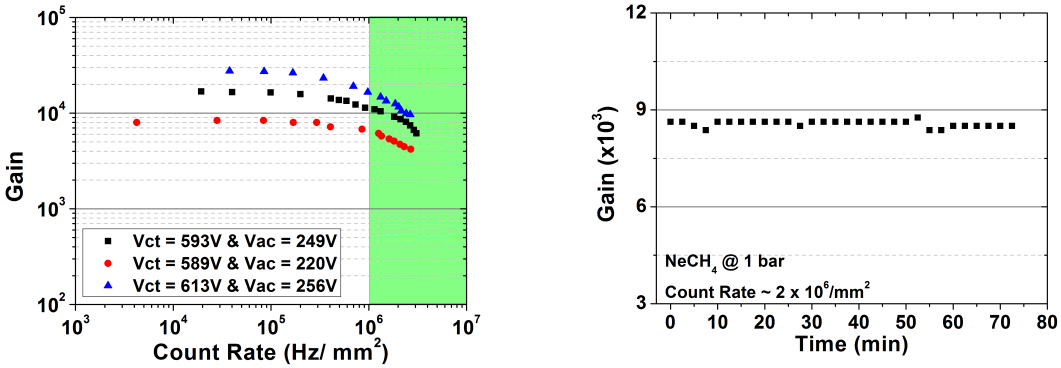

Figure 7.4: Gain as a function of the detector count rate (left) and gain as a function of the time (right) [109].

Figure 7.4 (left) shows that the gain does not change significantly as the count rate increases up to about 1 MHz mm^{-2}, independently from the applied voltages to the detector. Above this value the gain starts to decrease significantly. Therefore, to keep a linear relation between the incoming number of photons and the charge pulse amplitude, the count rate has to be kept below about 1 MHz mm^{-2}. Good detector operation stability allows reproducible results and stable spatial and energy resolutions. On the other hand, variations of the charge gain over time lead to the degradation of the resulting image and energy resolution. The behaviour of detector stability can be seen in Figure 7.4 (right). A stable detector operation was observed with very small variations, less than 5%. [109]

Concerning the detector count rate, as shown, 1 MHz mm^{-2} is possible, however the electronic instrumentation is limiting the total count rate. The pulse shaping takes about 4 µs which limits the count rate.

Good results were achieved in count rate and stability studies in the 2D-THCOBRA based detector filled with Ne/CH_4.

7.4 Spatial Resolution

Spatial resolution can be defined as the capability for a system to resolve fine details, i. e., the minimum size of an object that can be discriminated and seen in the image [3, 110]. The better the spatial resolution, the smaller the detected object details. Several approaches can be used to determine the spatial resolution, however, in all the methods, high contrast (high attenuation) objects are usually used in order to reduce noise influence.

To measure spatial resolution, the point spread function (PSF) can be used, despite being difficult to measure directly and not matching with other spatial resolution measurements. The edge response is a good alternative to PSF, since it allows the understanding of how the edges in the image are blurred and it is simple to measure. Then, the line spread function (LSF) can be determined by computing the first derivative of the edge response (Figure 7.5), and in turn the modulation transfer function (MTF) can be obtained by taking the FT of LSF. The 3% MTF value is taken as the limiting spatial resolution of the system. The FWHM of LSF is also a measurement of the system's spatial resolution. [110]

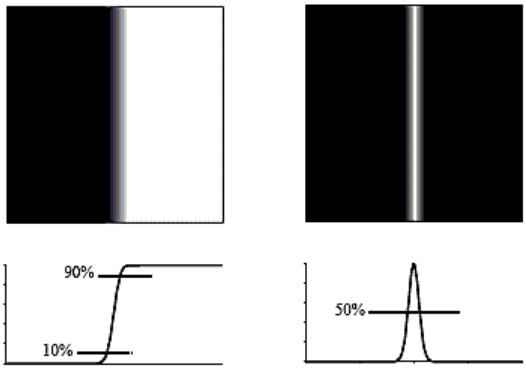

Figure 7.5: Edge response (left) and LSF (right) of an imaging system. The LSF is the derivative of the edge response. (Adapted from [110])

A measurement of the spatial resolution for this detector was obtained by determining the FWHM of the edge response function first derivative, LSF. The edge response was determined by imaging a sharp edge object, in this case a hexagonal stainless steel grid with a thickness of 100 µm, an absorbing wall of 360 µm and a pitch of 5 mm. [110] The grid was placed between the X-ray tube and detector window, defining a magnification factor of about 4.6. The X-ray tube voltage was set to 15 kVp.

In order to study the variation of the spatial resolution with the photon energy, six energy windows were defined to construct different images and measure the corresponding edge response functions. The results, shown in Figure 7.6 (left), represent the spatial resolution for each defined energy window. In Figure 7.6 (right) the images obtained for each energy window and the used grid are also shown. [109]

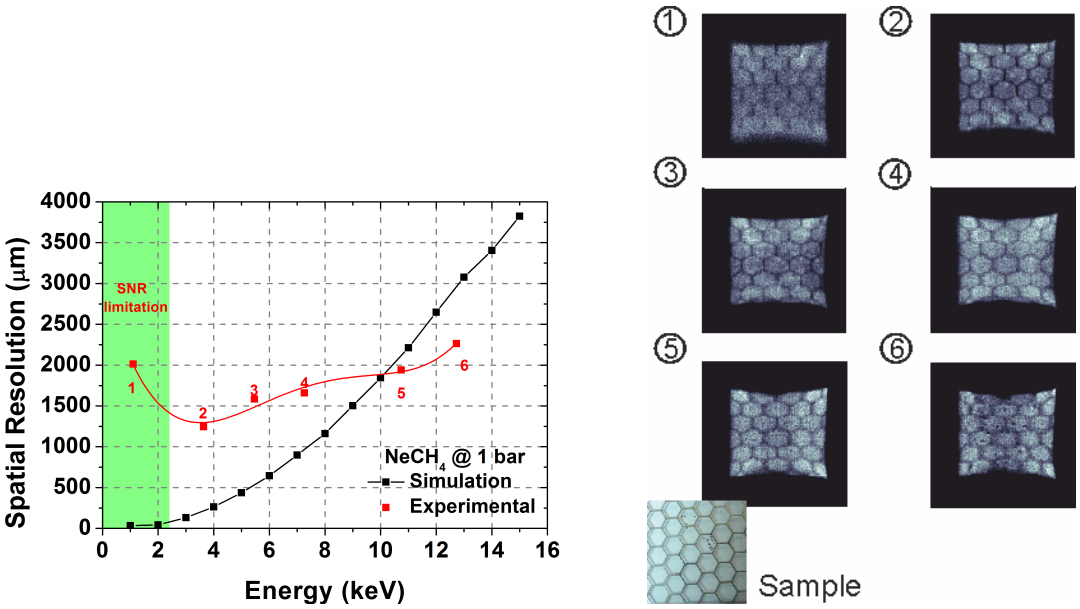

Figure 7.6: Left: Spatial resolution as a function of the photon energy; Right: Images constructed with different energy windows used to determine the spatial resolution represented on the left [109, 108].

As shown in Figure 7.6 (right), a different image is obtained depending on the selected energy window. The image corresponding to the lower energy window is noisier than the others. On the other hand, the image that shows visually better resolution is the second one, becoming worst when higher energies are used. Nevertheless, except for the first image, all the images show reasonable image quality. This is confirmed by the quantitative spatial resolution measurements shown in Figure 7.6 (left). For lower energies the SNR is the most limiting factor for the spatial resolution, while for higher energies it decreases as the energy increases. The best spatial resolution value achieved in this study was 1.2 mm for energy photons of about 3.6 keV. For higher energies, the primary electron cloud generated from the photoelectron range in the present gas medium strongly limits the spatial resolution [108, 75]. The simulation results were obtained using the Degrad program [108] and plotted in Figure 7.6 (left). The simulations were done considering a monoenergetic radiation while the experimental results consider an energy window for the measurements. Despite the differences on absolute values, the experimental and simulation results show the same behaviour: the spatial resolution degrades as the photon energy increases.

The value of the spatial resolution reached using a double THGEM detector (1.4 mm) is comparable to the best value achieved with 2D-THCOBRA detector, and, in both cases, is limited by the photoelectron range. [72]

7.5 CT Imaging

For demonstration, this detector was first applied in X-ray transmission imaging of a butterfly and a sea snail.

The imaged butterfly is shown in Figure 7.7 (top). The X-ray tube voltage and current were set to 5 kVp and 270 µA, respectively. For this study it was taken advantage of a magnification factor in both images shown in Figure 7.7 on the bottom. The butterfly body was imaged with a magnification factor of 2.5 and the detail with 3.8. [109]

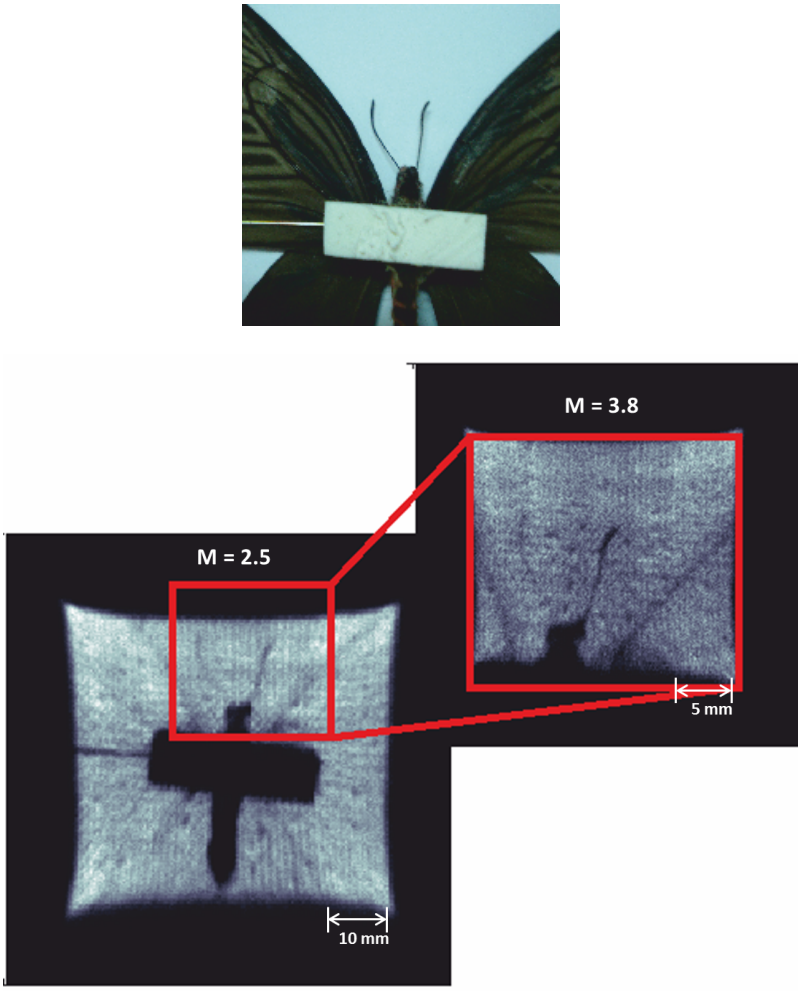

Figure 7.7: Top: Photography of the imaged butterfly; Bottom: X-ray transmission images with a magnification factor of 2.5 (Left) and 3.8 (Right), respectively [109].

Despite some artefacts, the images show good general quality with a good definition of the contours of the body and wings. Increasing the magnification factor allowed having a more detailed and defined image of antennas and coastal margin of the wings. In this case, due to the photon energy, a small photoelectron range is verified, as shown previously in Figure 7.6 (left). Furthermore, for this energy, the detection efficiency is good. [109]

The sea snail, shown in Figure 7.8 (left), was imaged with an X-ray tube voltage and current of 50 kVp and 4 µA, respectively, and a magnification factor of 4.6. The X-ray transmission image is shown in Figure 7.8 (right).

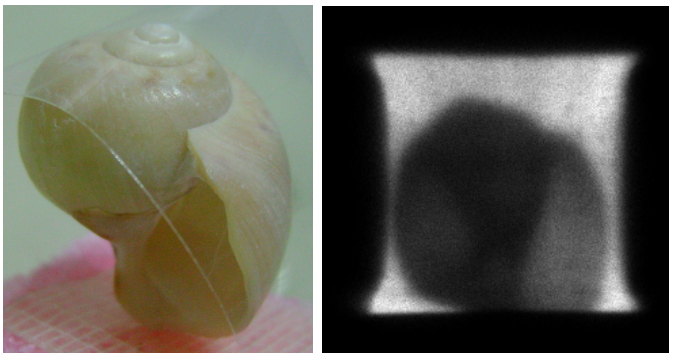

Figure 7.8: Sea snail photo and respective X-ray transmission image [109].

The sea snail exoskeleton is visible from the columellar wall to the apex. The image shows the sample contours and a fair contrast between the less and more dense areas, namely in the columella. The more dense structure at the central axis can be well distinguished. The photon energy does not maximize the detector's capabilities: the spatial resolution is reduced due to the significant photoelectron range (Figure 7.6 - left) and the detection efficiency in this energy region is very low. However, since the sea snail shell is mostly composed of calcium carbonate [111, 112], using a photon energy that maximizes these parameters (such as the case of the butterfly) will not provide an adequate image contrast. [109]

The presented images indicate good prospects of applying this detector in X-ray imaging, allowing good general image quality even without image processing.

The CT acquisitions made using this detector were performed taking advantage of magnification, to increase object detail in the image. It was used with a SDD of about 104.5 cm and a SOD of 22.5 cm, providing a magnification factor of 4.6.

Cross-sectional images of the PMMA phantom with chalk and air were acquired and multi-slice and 3D reconstructions were performed. The acquisitions were performed with an X-ray tube voltage and current of 25 kVp and 18 µA, respectively. The acquisition time of each view was 7 s and the motion time of the stepper motor was 5 ms. 400 views were acquired resulting in a total acquisition time of 47 min. After the first attempt to reconstruct the cross-sectional image, it was verified that the contours of the chalk rod were not well defined, which could be due to a misalignment of the sinogram rotation centre. A test using the CTRADIX tool developed for this purpose (described previously in Section 3.2.1) was performed. After evaluation, a shift correction of -2 pixels was applied before the multi-slice and 3D reconstructions. In Figure 7.9 (top) two cross-sectional images are shown, one ob-

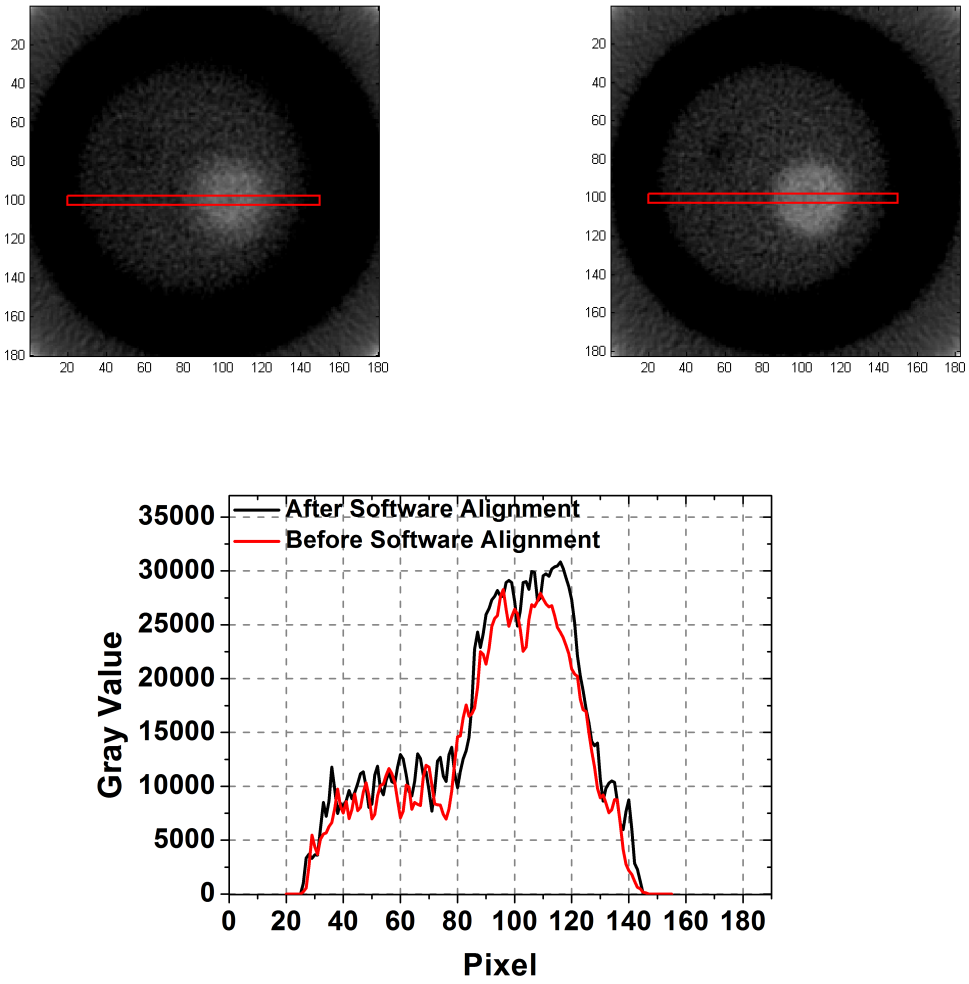

Figure 7.9: Top: Cross-sectional images of the PMMA phantom with chalk and air before (left) and after (right) software alignment marking the area used for the plot shown in the bottom.

tained with no correction of the rotation centre by software (left) and the other reconstructed after correcting the referred shift in the sinogram (rigth). The CT images show a rectangle defining the region used for the plot seen in 7.9 (bottom).

The gray value is a representation of the attenuation coefficient of the imaged objects. The air is represented as 0 gray value, the PMMA has a higher relative value and the chalk has an even greater value, which is considered adequate for the case, considering the attenuation coefficients of the components. Figure 7.9 (top - right) shows a slightly improved image. The contours of the chalk rod are visually better defined when compared with the cross-sectional image on the left. Also, the air rod can be better distinguished in the corrected image than in the first image. The plot of Figure 7.9 (bottom) shows that the intensity in the chalk region increases more abruptly in the contour regions (around pixels 90 and 120) in the corrected

image than in the other. Besides, its intensity is slightly higher. This means that the contours are more defined in the corrected image and supports what is visible in the cross-sectional images.

After applying the correction related with the misalignment, six cross-sectional images of the PMMA phantom with chalk and air were obtained. The images, shown in Figure 7.10, have 190 × 190 pixels and were reconstructed using sinograms with 256 rays. Since part of the phantom base was imaged and was not considered for reconstruction, each cross-sectional image corresponds to an object section of 2.8 mm.

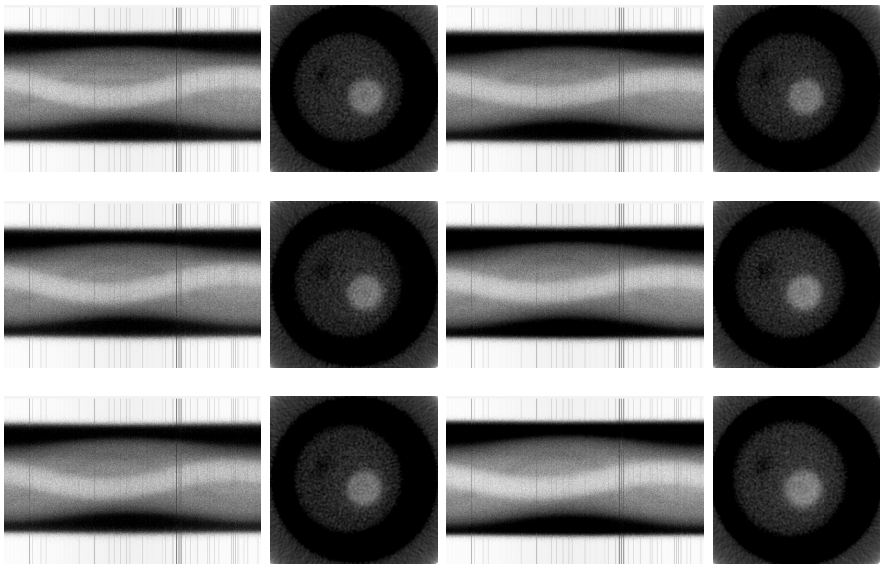

Figure 7.10: Sinograms of the PMMA phantom with chalk and air (left) and the corresponding cross-sectional images (on the sinograms right).

In the sinograms of Figure 7.10 the chalk rod and the PMMA phantom can be clearly distinguished. Although the air rod has lower contrast, it can be also seen. Some discharges, visible in the sinogram, occurred during acquisition. It appears that these are not decreasing the cross-sectional image quality significantly. The CT images show both the PMMA phantom and the chalk rod very well defined and with good contrast. The contours of the air rod are not so well defined as the other constituents, however it can be seen in all the cross-sectional images. The image quality could benefit with an acquisition of higher statistics and with post-processing to enhance the contrast, for example.

These images were used to reconstruct a 3D image of this section of the PMMA phantom, as previously explained in Section 4.3. The result is shown in Figure 7.11.

Despite some artefacts, the 3D image of the phantom with chalk and air shows the three surfaces. The most well defined surface is the one corresponding to the chalk rod with less surrounding structures with the same isovalue. The air rod and the PMMA are also well defined, however with more irregularities in their surfaces. Nevertheless, the image is a good

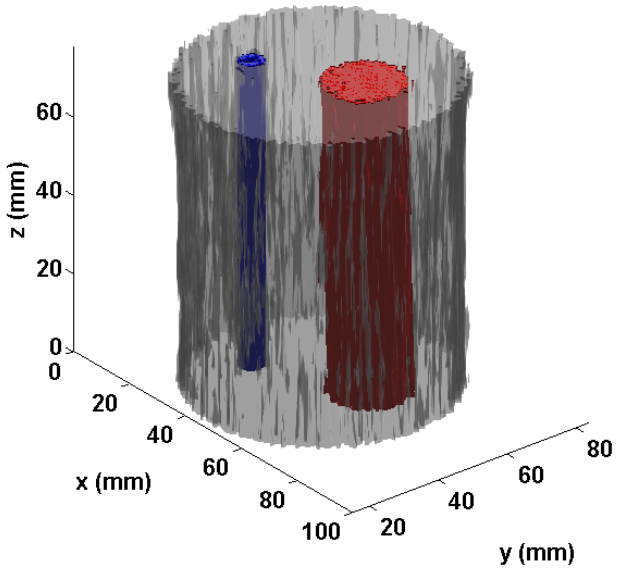

Figure 7.11: 3D image of the phantom with chalk and air, in which the PMMA surface is represented in gray, the chalk surface in red and the air surface in blue.

representation of the imaged object.

Other cross-sectional images of the PMMA phantom with chalk and brass were acquired and multi-slice and 3D reconstructions were performed. The acquisitions were done using the same parameters as in the previous case. In this case, a correction of the misalignment of the rotation and detector centres was needed, and, therefore, executed in the sinogram. A shift correction of 1 pixel was carried out. The sinograms were constructed with 256 rays and the cross-sectional images with 190×190 pixels. 10 CT images were reconstructed after correcting the misalignments, each corresponding to a cross-section of 1.7 mm. The resulting images are shown in Figure 7.12.

The sinograms show the structures of the imaged components (PMMA, chalk and brass) with a good contrast and it is possible to distinguish them very well. Some discharges occurred during the acquisition, which are visible in the sinograms. The cross-sectional images, similarly to the sinograms, show all the components very well distinguished with a good contrast. Also, beam hardening artefacts are visible between the chalk and brass rod and in the external area of the phantom near the brass rod.

The 3D image was reconstructed using the slices shown in Figure 7.12. It allowed separating the chalk and brass rod from each other and from the PMMA. Since a good contrast in the cross-sectional images was presented, the selection of the surfaces isovalues was easier. It is interesting to note that the beam hardening artefact is also visible in the 3D image. In

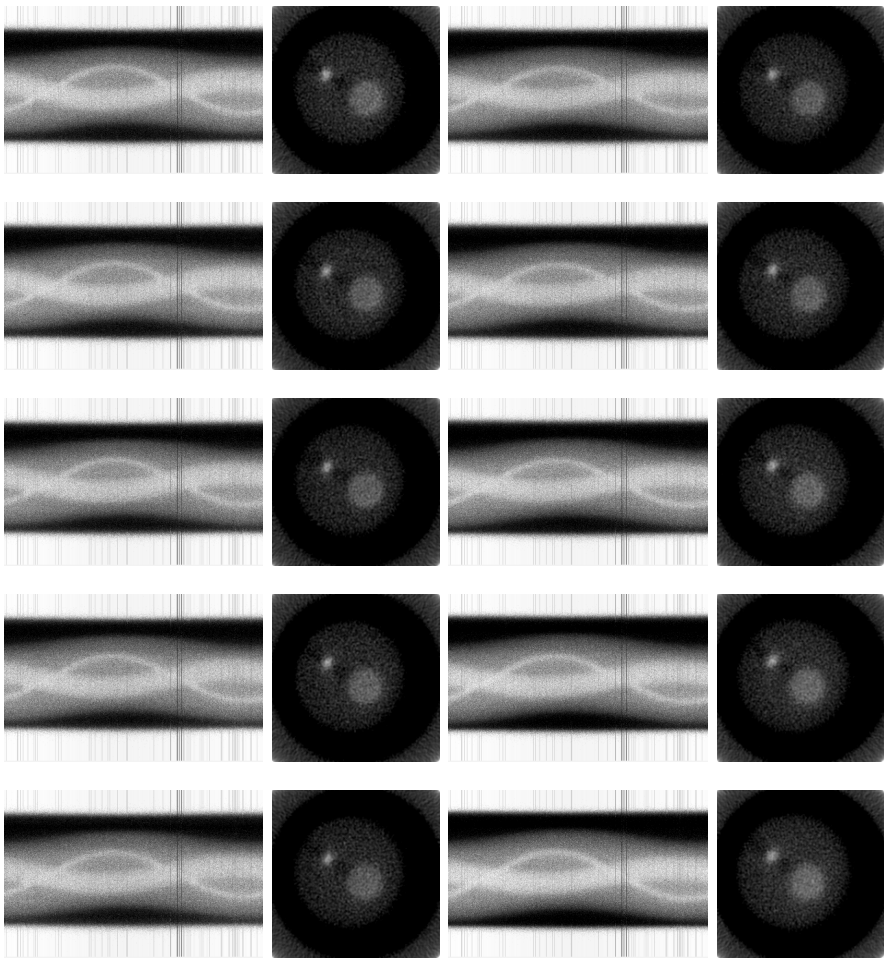

Figure 7.12: Sinograms of the PMMA phantom with chalk and brass (left) and the corresponding cross-sectional images (on the sinograms right).

the external area of the PMMA near the brass rod there is a lower intensity region due to this artefact.

The sea snail was also used for CT imaging. The X-ray tube voltage and current were set to 50 kVp and 6 µA, respectively, to acquire 400 views, each with an acquisition time of 10 s.

Sea snail cross-sectional images were reconstructed without flat field or energy correction. An image of this reconstruction is shown in 7.14 (top - left). In this image, the contours of the sea snail shell are not well defined. This might be due to misalignment of the rotation and detector centres. Thus, an alignment test was done using the CTRADIX tool developed for this purpose. A shift of -7 pixels between both centres (rotation and detector) was found. After correcting the shift in the sinogram, the new cross-sectional image was reconstructed and the result is shown in Figure 7.14 (top - right). The cross-sectional images of Figure 7.14 (top) show a rectangle marking the region chosen to plot the profile shown in Figure 7.14 (bottom).

The air is represented as 0 gray value and the exoskeleton has a much higher relative

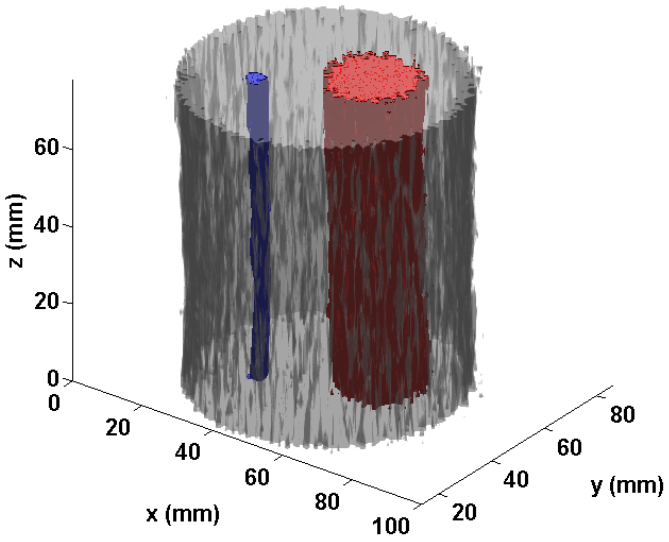

Figure 7.13: 3D image of the phantom with chalk and brass, in which the PMMA surface is represented in gray, the chalk surface in red and the brass surface in blue.

value, also considered adequate for the present case. The image reconstructed after alignment correction shows an improvement in the definition of the sea snail exoskeleton contours. The profile plot supports this idea. In the profile corresponding to the cross-sectional image reconstructed with the misaligned sinogram, an increase in the intensity is visible around the 105^{th} pixel. On the other hand, in the profile corresponding to the image obtained after alignment, an intensity peak around the 115^{th} pixel is visible. The intensity of this peak is about 30% higher than the first. This means that the sea snail shell is better defined in the image obtained after sinogram alignment. Comparing with the PMMA phantom with chalk and air, in this case the correction of the centres misalignment appears to be more effective. However, it has to be considered that the value of the shift in this case is also greater than in the PMMA phantom case: in the PMMA phantom it was -2 pixels while in the sea snail it was -7 pixels and both the artefacts (originated in the shift) and the correction become more evident.

After taking into account the correct shift to align the sinogram, multi-slice reconstruction of a sea snail acquisition was carried out. 15 sinograms and the respective cross-sectional images were obtained and are shown in Figure 7.15. The sea snail has a height of 2 cm, which means that each cross-sectional image corresponds to a slice in the object of approximately 6 mm (for the specified magnification factor).

The sinograms show the angular position of the sea snail structures relative to the detector, as they change during the acquisition. Some structures of the sea snail can be distinguished

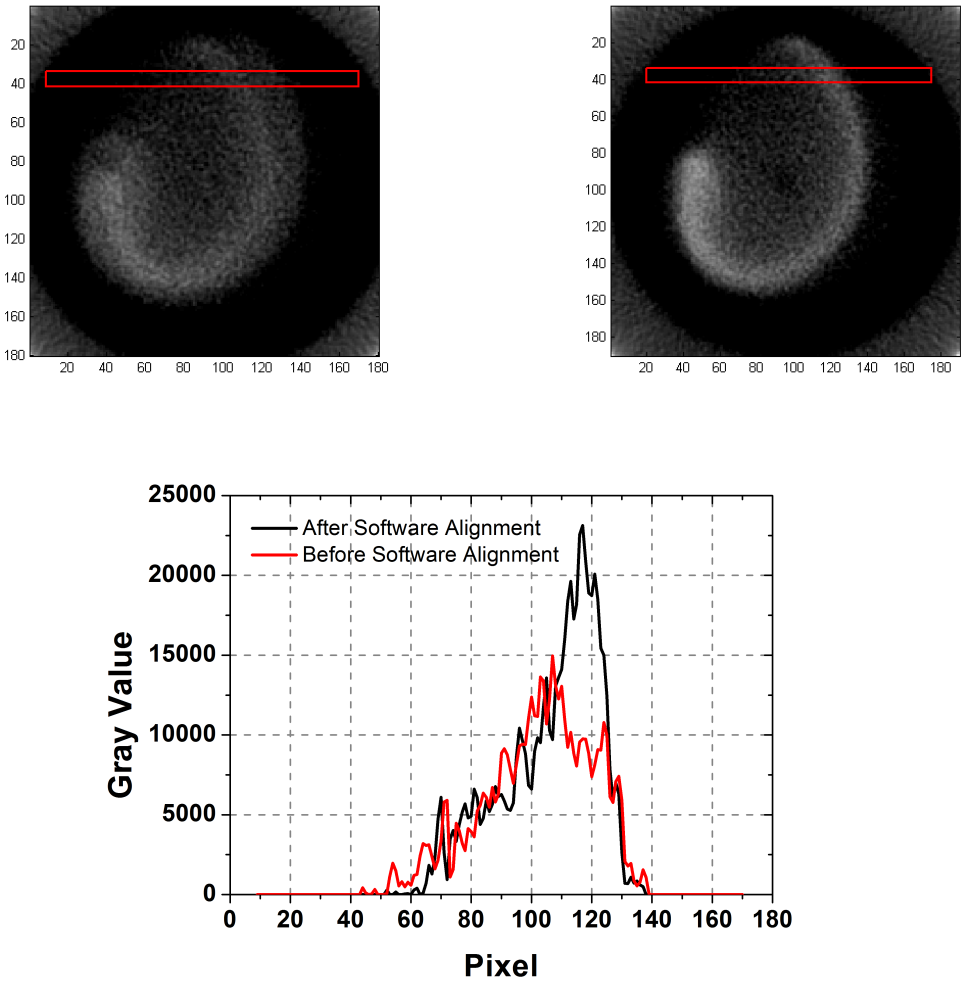

Figure 7.14: Top: Sea snail cross-sectional images before (left) and after (right) software alignment marking the area used for the plot shown in the bottom.

in the sinogram, as for example the central axis which is more dense. During the acquisition, some discharges occurred, which are visible in the sinogram. The longest discharge occurred at the end of the acquisition. However, no detrimental effect seems to come in the cross-sectional images as a consequence of it. The cross-sectional anatomy of the sea snail is well visible in the cross-sectional images. The sea snail exoskeleton is clearly visible from the bottom up to the apex. The internal space of the sea snail reduces from the columella up to the apex, which is also demonstrated in the CT images. In the cross-sectional images corresponding to the upper part of the sea snail, some partial volume effect is visible. Generally, the perceptual image quality is good taking into account the slice thickness. The CT images represent truthfully the sea snail, showing its exoskeleton with good definition and contrast.

Using the presented cross-sectional images, a 3D image was computed similarly as described in Section 4.3. Figure 7.16 shows the obtained images, in which different perspectives

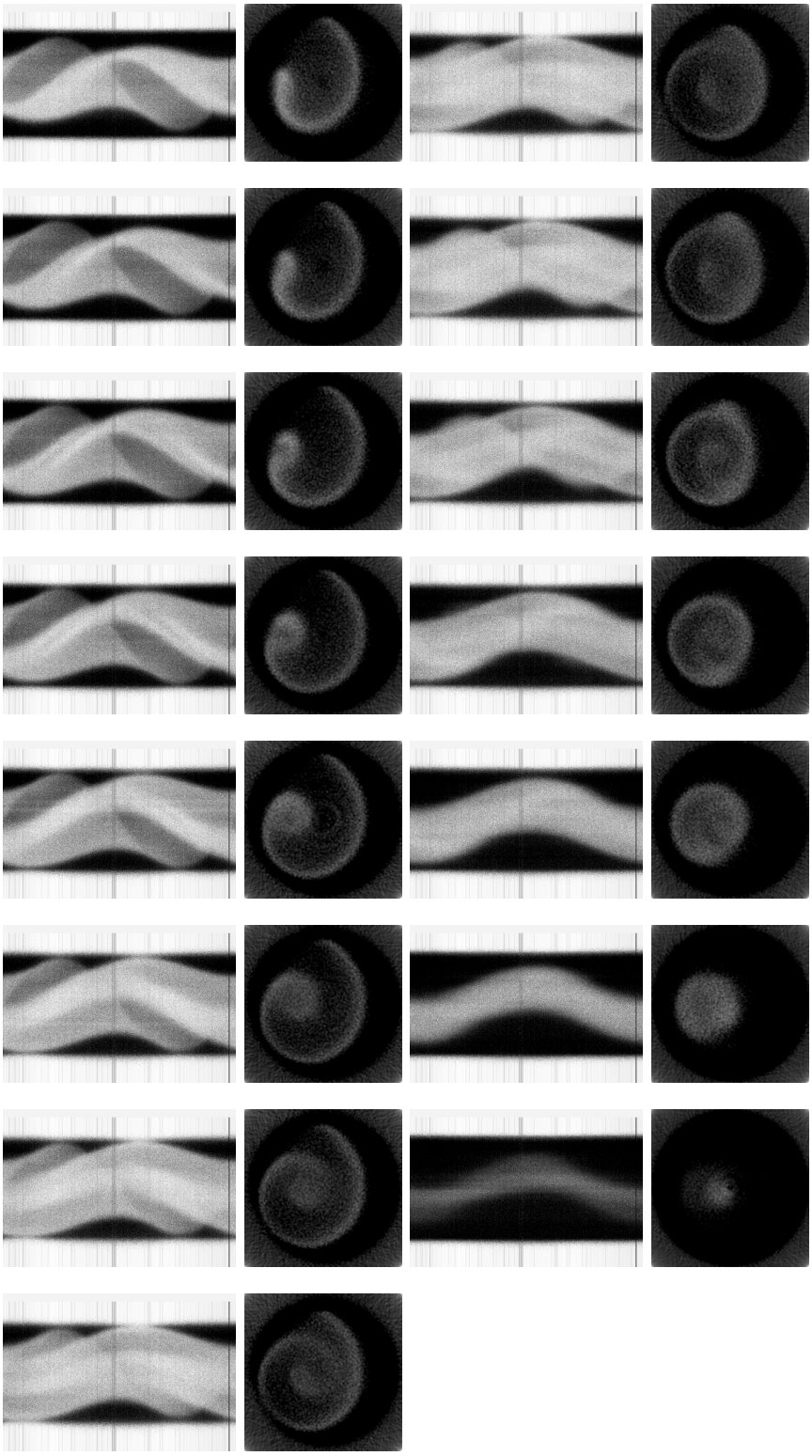

Figure 7.15: Sea snail sinograms (left) and the corresponding cross-sectional images (on the sinograms right).

of the sea snail are visible.

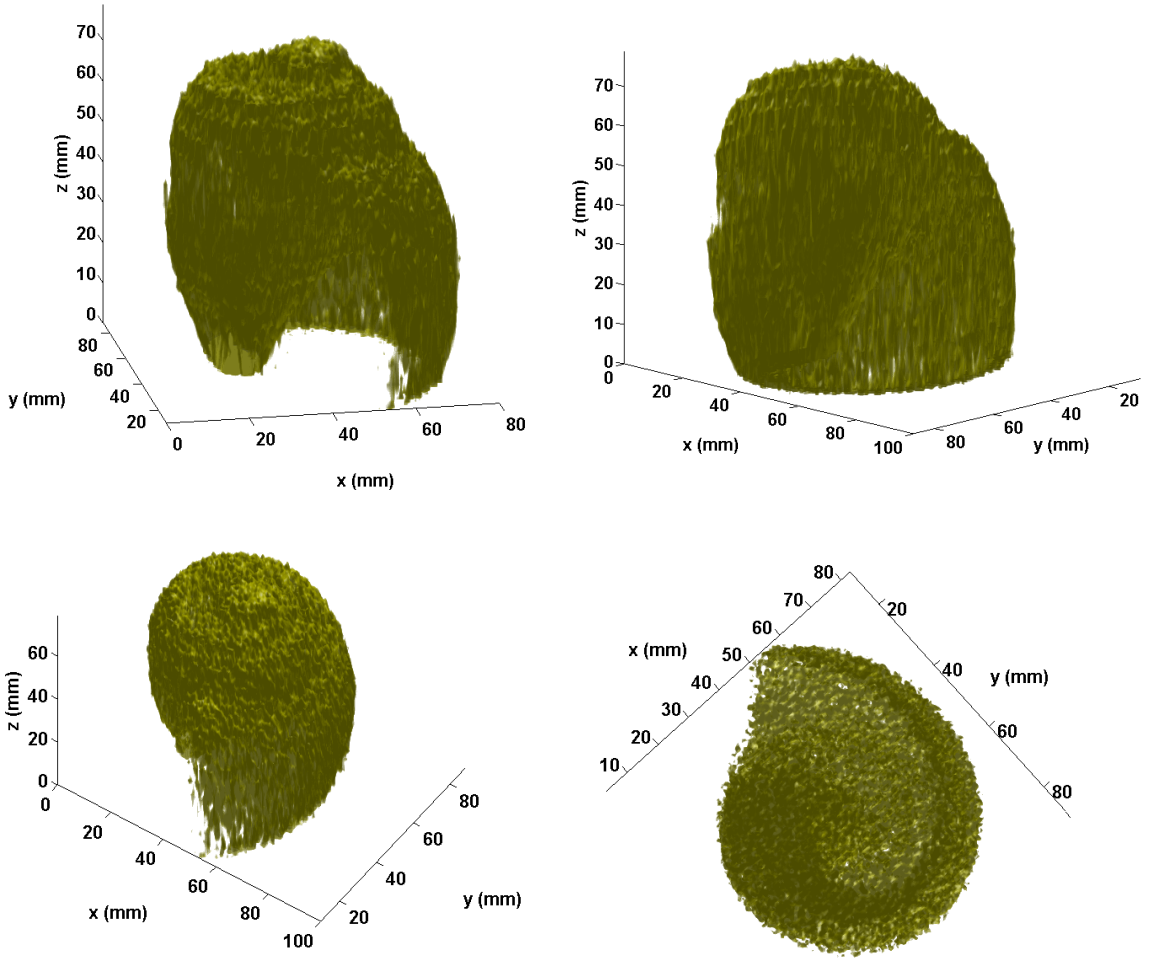

Figure 7.16: 3D image of the sea snail computed using the 15 cross-sectional images. Front (top - left), back (top - right), oblique (bottom - left) and bottom (bottom - right) perspectives are shown.

In the front perspective (Figure 7.16 top - left) in the left middle area of the volume, a part of the shell is not visible, because a small area is out of the FOV. This is consistent with the cross-sectional images in Figure 7.15, in which the shell is not completely visible. In this image, the sea snail aperture is clearly visible. In the back perspective of the 3D image (Figure 7.16 top - right) the sea snail back is truthfully represented. In the oblique perspective (Figure 7.16 bottom - left) the sutures are visible and can be distinguished from the remaining shell. Finally, in the bottom perspective (Figure 7.16 bottom - right), the interior cavity filled with air is also clearly visible.

A good representation of the sea snail was achieved. The contours have good definition and can be clearly separated from the regions of air.

The sea snail imaging is considered a successful example using the developed detector,

clearly separating the sea snail exoskeleton with good contrast and definition. Furthermore, no post-processing was applied to the images, which probably would enhance image quality significantly.

Comparing the sea snail 3D images obtained with this detector with the ones achieved with the previous detector configuration (with the THGEM), shown in Figure 6.9, it is possible to clearly see that these images represent much more truthfully the sea snail and have better image quality. The aperture, the sutures and the apex of the sea snail are much more visible in these images than in the previous. This can be due to the detector performance that is generally better and the higher magnification factor of the acquisition.

CHAPTER

8

2D-THCOBRA BASED DETECTOR FILLED WITH PURE KR

The 2D-THCOBRA based detector filled with Ne/CH_4 provided images with good quality, however its spatial resolution limits the global image quality and presents also a lack of efficiency. As shown in Figure 7.6, the photoelectron range in Ne/CH_4 limits the spatial resolution, and for this reason a heavier gas medium should be used in order to enhance this performance parameter. Pure Kr can present a solution for imaging applications since it allows higher absorption efficiency and better spatial resolution. As seen in Figure 8.1, pure Kr has an absorption efficiency about two orders of magnitude higher than Ne/CH_4; and concerning the spatial resolution, half of the value could be achieved as will be shown later in Section 8.4. A 2D-THCOBRA based detector filled with Kr was assembled, as described in Section 3.1.4.2, to overcome this limitation.

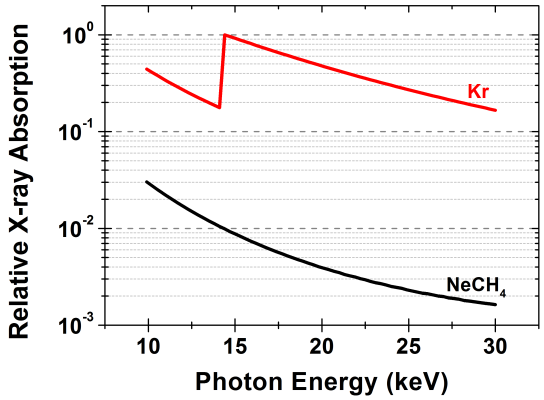

Figure 8.1: X-ray absorption for Ne/CH_4 and Kr, showing that Kr has an absorption efficiency two orders of magnitude higher than Ne/CH_4.

8.1 Charge gain

A charge gain study was performed similarly to the one made in the 2D-THCOBRA detector filled with Ne/CH_4. Thus, the charge gain as a function of the applied voltage to the detector was measured on the top and on the anode electrodes.

The readout electronics was also calibrated in order to obtain a charge gain absolute value. However, the calibration was performed with a different experimental setup. The charge pulse was sent to the pre-amplifier using the BNC PB-5 Precision Pulse Generator (the same used for the $10 \times 10\,cm^2$ detector) and a capacitor of 1.5 pF ($\pm$0.25pF). The output pulse was measured by the N1728B NIM and the spectrum was obtained using CTRADIX software. Thus, a relation between the N1728B NIM channel and the charge pulse can be established. Figure 8.2 shows a scheme of the experimental instrumentation used for calibrations.

For the charge gain measurements the detector was irradiated with a ^{109}Cd radioactive source. Afterwards, the primary charge was calculated using the W value (24.2 eV per

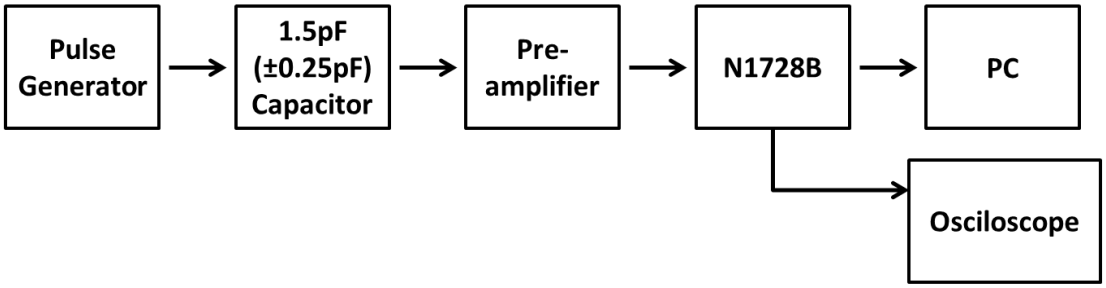

Figure 8.2: Scheme of the experimental apparatus of the gain calibration measurements for the $2.8 \times 2.8\,\mathrm{cm}^2$ active area detector.

electron-ion pair [48]) and the energy of the incident radiation and the total charge determined knowing the N1728B channel. Finally, the charge gain was determined by calculating the ratio between the total and primary charges. Figure 8.3 shows the obtained gains as a function of V_{CT} and V_{AC}.

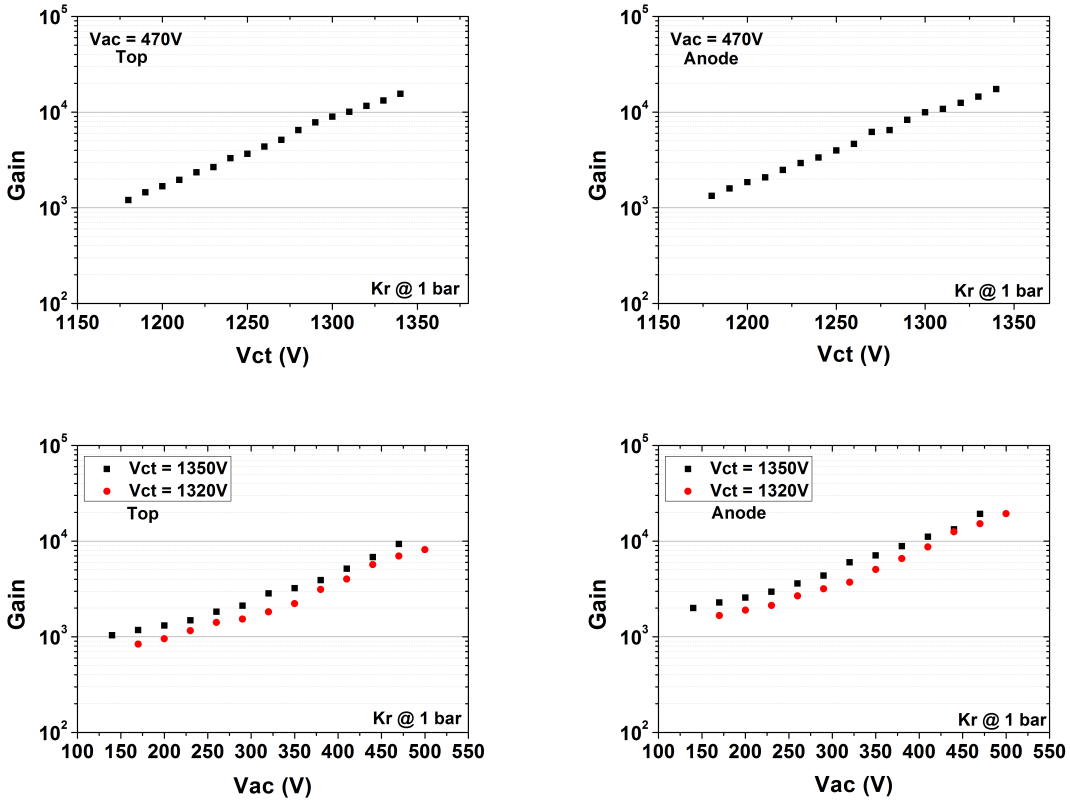

Figure 8.3: Gain as a function of V_{CT} (Top) and V_{AC} (Bottom) applied to the structure, measured on top (Left) and anode (Right) electrodes, with pure Kr filling the detector chamber.

As expected, a behaviour similar to the $10 \times 10\,\mathrm{cm}^2$ active area detector is verified. The

charge gain increases for higher applied voltages to the detector, following an exponential behaviour. As can be seen, maximum achievable gains of about 1×10^4 for anode and top electrodes were obtained.

For a fixed V_{AC} value of 470 V, gains of about 2×10^4 were achieved on anode and top electrodes with a V_{CT} value of 1340 V. The gains achieved for a fixed V_{CT} value of 1320 V were of about 1×10^4 and 2×10^4 on top and anode electrodes, respectively, applying a V_{AC} value of 500 V. For a fixed V_{CT} value of 1350 V the achieved gains were nearly the same with a V_{AC} value of 470 V.

This detector provides gains comparable with THGEM based detectors operating in pure Kr [113]. The 2D-THCOBRA detector presents a more simpler solution with only one microstructure and without readout plane, when compared with a THGEM based detector.

8.2 Energy Resolution

Energy resolution was measured as a function of V_{AC}. A 4 mm diameter hole lead collimator was placed in front of the detector window in the centre of the structure. X-rays from a ^{109}Cd radioactive source irradiated the detector and a pulse height distribution was stored for each V_{AC} voltage. The energy resolution was determined as in the case of the detector filled with Ne/CH_4. Figure 8.4 shows the obtained results.

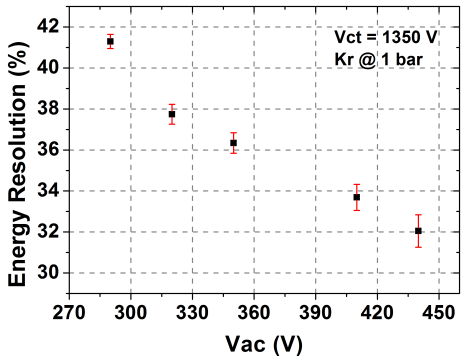

Figure 8.4: Energy resolution as a function of V_{AC}, with the detector operating in pure Kr.

An improvement of the energy resolution is verified for higher applied voltages. The best value was 32 % (FWHM at 22 keV) achieved for a V_{AC} value of 440 V. As seen from the figure, the limitation of the energy resolution is due to the maximum voltage that could be applied at the moment of the measurements.

The energy resolution of this detector is worse than the achieved with a single (23% FWHM at 5.9 keV) or a double (between 25% and 34% FWHM at 5.9 keV) THGEM detector [113]. With higher applied voltages it would, probably, be possible to reach a better energy resolution with the THCOBRA based detector. A different experimental configura-

tion (compared to the measurements made with the detector operating in $NeCH_4$) and the shaping time probably that was not optimized for the operation conditions can explain these results. It is intended to improve this point in the future, since a better energy resolution value is expected [113, 114].

8.3 Count Rate Capability and Time Stability

Count rate and detector stability studies were also done for this detector. The gain as a function of the count rate per mm^2 and the gain as a function of time were evaluated. The detector was irradiated directly with the X-ray tube through a 500 µm diameter hole lead collimator. The count rate study was performed increasing gradually the X-ray tube current and the detector stability study was done setting the X-ray tube current to a constant value providing a count rate of about $1 \times 10^5 Hz\,mm^{-2}$. This will be an aspect to further investigate in the future. The results can be seen in Figure 8.5.

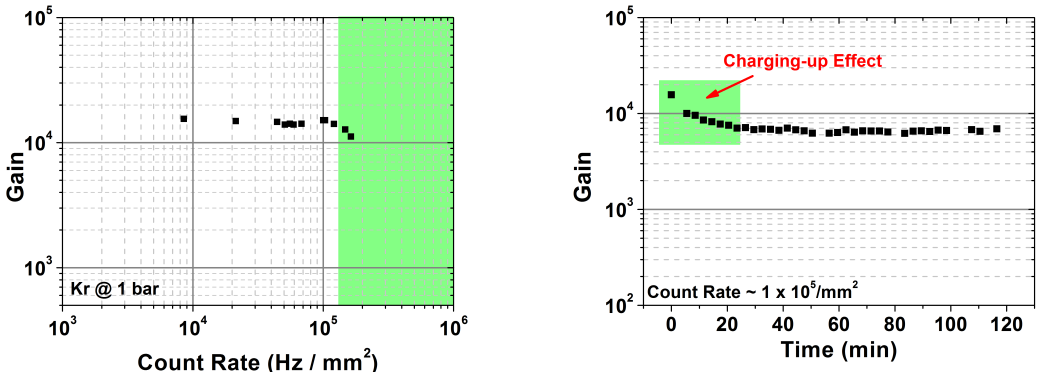

Figure 8.5: Gain as a function of the detector count rate (left) and gain as a function of time (right).

Figure 8.5 (left) shows that, up to count rates of $1 \times 10^5 Hz\,mm^{-2}$, the detector gain is very stable. Above this value, the gain decreases, which means that to keep a linear relation between the incoming photons and the charge pulse amplitude, the count rate shall be kept below $1 \times 10^5 Hz\,mm^{-2}$.

The detector stability study, shown in Figure 8.5 (right), demonstrates an initial gain decrease in the first 20 min, being very stable after that. The initial reduction in the gain suggests a charging up effect in which charges accumulate on the insulator surface of the structure and locally changes the electric field, resulting in a modification of the gain [72, 115–117]. At the point when no more charges impinge the insulator surface, the gain reaches a stable value. The gain variation can be very different depending on the structure itself, its geometry and fabrication process. [72, 115–117]

Despite the limited detector count rate of 1×10^5Hz mm^{-2}, X-ray imaging is possible keeping the count rate below this value to certify that the gain is as high as possible. On the other hand, after the first 20 min, where charging up occurs, the detector shows a very good stability, with variations lower than 11%, for long continuous operation periods.

8.4 Spatial Resolution

Spatial resolution was determined as a function of the applied voltage to the detector and as a function of the incident photon energy.

X-ray transmission images of the grid described in Section 7.4 were acquired with an X-ray tube voltage of 30 kVp. In order to determine a value for the spatial resolution in x and y directions (anode and top electrodes, respectively) two sets of acquisitions were done by placing the grid in front of the detector window (without magnification factor) in orthogonal directions for each set (Figure 8.6 - top).

For the study of the spatial resolution as a function of V_{AC}, an image was stored for each value of the applied voltage. Figure 8.6 (bottom) shows the obtained results.

As expected, the spatial resolution improves as V_{AC} increases, with the best values achieved for the maximum applied voltage (V_{AC} = 450 V). A spatial resolution of 600 µm and 500 µm was achieved for x (anode) and y (top) directions, respectively. The better value of spatial resolution reached for the top electrodes direction can be due to the contribution of ions to the measured signal, increasing the SNR of the pulse and enhancing the precision of the position determination.

The variation of the spatial resolution as a function of the incident radiation energy was also studied to evaluate the energy range in which the detector has a better performance in terms of spatial resolution. The procedure was similar to the one described in Section 7.4, taking into account that the maximum energy bin now corresponds to 30 keV. Six energy windowed images were constructed and the spatial resolution was determined. Figure 8.7 shows the obtained results together with the simulation data computed for pure Kr.

The X-ray images of the grid reconstructed with different energy bins, show a non-uniform detector response. The X-ray transmission images reconstructed with the two lowest energy bins are the noisiest (the first bin even noisier than the second). For the following energy bins, the images have lower noise and the spatial resolution increases. In the image corresponding to the highest energy bin, more severe non-uniform response is seen. The visual analysis of the images corroborates the measurements performed.

The position resolution simulation results plotted in Figure 8.7 show a dependence with the absorption curves for Kr. After interaction of a photon, with energy slightly higher than the absorption edge, with the gas atoms, a photoelectron with very low energy is originated by ionization, losing rapidly its energy near the photon interaction region. This means that

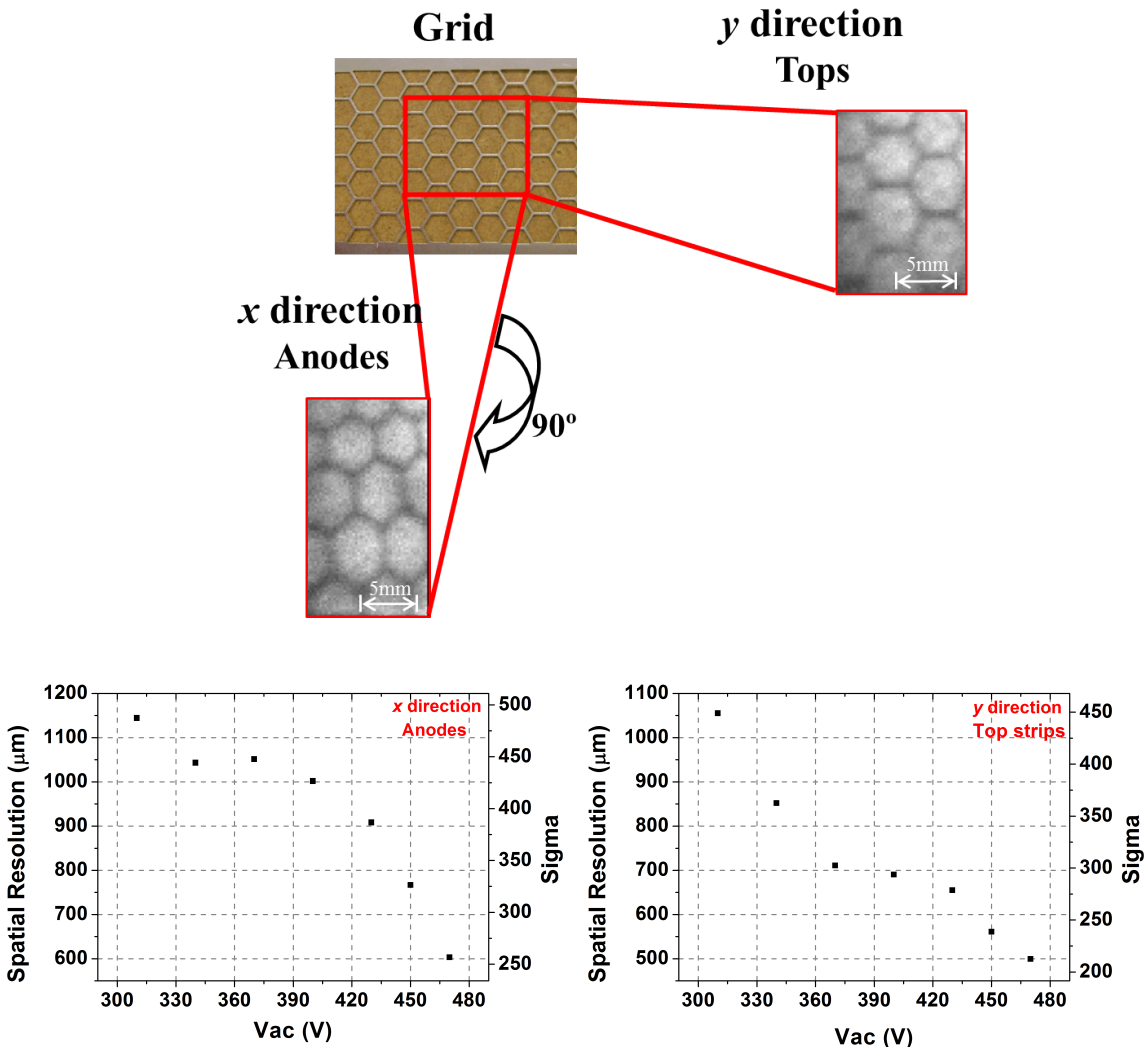

Figure 8.6: Top: Scheme used for the spatial resolution measurements for both x and y directions; Bottom: Spatial resolution as a function of V_{AC} achieved on the top (Left) and anode (Right) electrodes, with pure Kr filling the detector chamber.

the distribution of the charge avalanche will not be spread over a wide area, resulting in an improvement of spatial resolution. In the experimental data below 10 keV the spatial resolution is limited by the SNR. Above that energy, the behaviour of the experimental results is comparable with the simulation data. Just before the absorption edge (≈ 12.5 keV), the experimental and simulated values are close; above the absorption edge a significant difference between both data is observed and for higher energies the values are approaching again. The discrepancy between experimental and simulated spatial resolution, specially in the absorption edge, can be explained due to the fact of the simulation data were obtained considering monoenergetic photons while the experimental measurements were made using an energy bin with some width, limiting the energy resolution. Therefore, all the photons

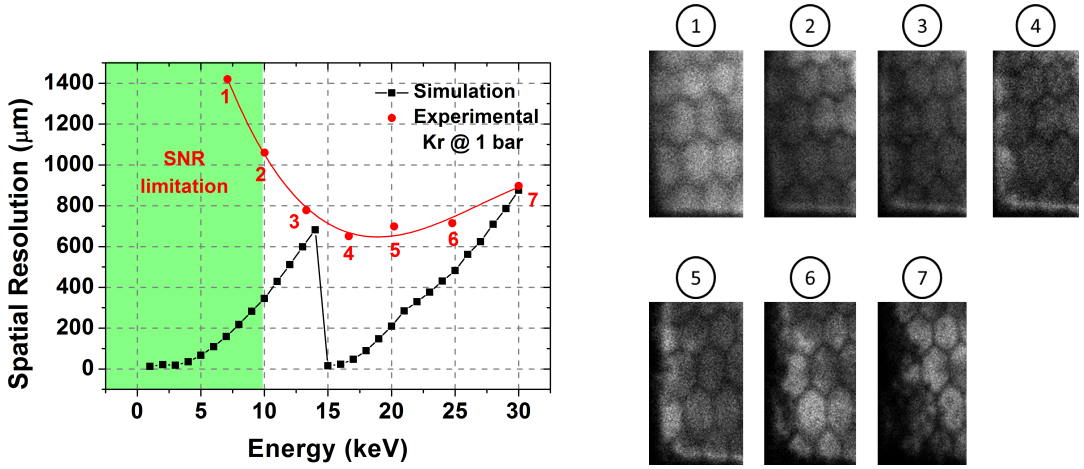

Figure 8.7: Left: Spatial resolution as a function of the incident photon energy simulated for monoenergetic photons and experimentally determined; Right: Images constructed with different energy windows used to determine the experimental spatial resolution represented on the left [108].

(with different energies within the considered bin) contribute to the measurement. Also, in the experimental data, a continuous spectrum is being used, which means that it is not possible to distinguish contributions from the various physical processes that can occur in the detector, such as fluorescence or Auger processes, that can degrade spatial resolution when considered for the measurements.

The comparison between the results of spatial resolution obtained with Ne/CH_4 and pure Kr, reveals an improvement of about 50%. This means that half of the value was determined using pure Kr as filling gas. The spatial resolution, together with the absorption efficiency, are the great advantages of using pure Kr instead of Ne/CH_4 as filling gas.

8.5 First X-ray Images

In order to assess the detector performance for X-ray imaging, some X-ray transmission images were acquired. The stainless steel grid, a SIM card and an operational amplifier were imaged.

The grid, already described, was imaged with an X-ray tube voltage and current of 30 kVp and 2 µA. Figure 8.8 shows the images obtained with a V_{CT} value of 1350 V and a V_{AC} value of 450 V reconstructed using all the energy spectrum.

The grid images show good quality and allowed having a measurement of the detector spatial resolution. The grid structure with a wall width of 500 µm is perfectly distinguishable

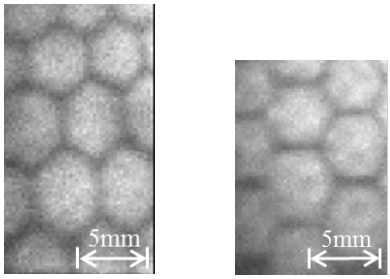

Figure 8.8: Grid images acquired for spatial resolution measurements in the anode (left) and tops (right) directions.

and well defined.

A SIM card was also imaged. The X-ray tube voltage and current were set to 25 kVp and 2 µA, respectively. The values of V_{CT} and V_{AC} during acquisitions were 1350 V and 450 V, respectively, corresponding to a gain of about 7×10^3. Initially, no magnification factor was defined, however, to improve image quality, a magnification factor was set. The SDD and the SOD were 140.5 cm and 81.5 cm, respectively, providing a magnification factor of about 1.7. Figure 8.9 shows the achieved images.

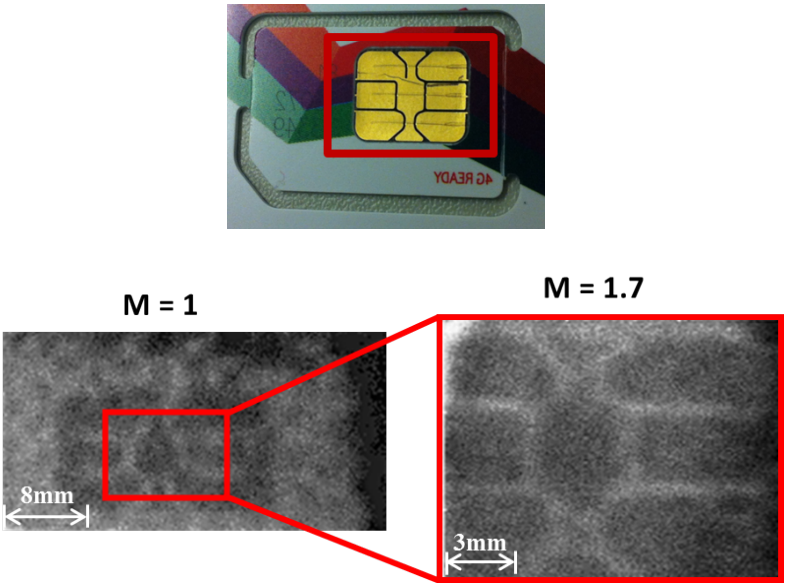

Figure 8.9: Top: SIM card with the imaged area marked with the red rectangle; Bottom: X-ray transmission images acquired without (left) and with magnification factor of 1.7 (right).

Both images show good definition of the SIM card constituents, essentially the gold connector plate. The image acquired without magnification, shows the gold connector plate and the surrounding plastic protector. This image shows some artefacts, such as a non-uniform intensity distribution along the image area. In the image acquired with magnification, these artefacts are not so evident. However, in the borders high and low intensities are visible,

which means that the detector response is not uniform in these areas. Nevertheless, a very good definition of the lines between the contacts of the gold connector plate is achieved using a magnification factor of 1.7.

An X-ray transmission image of an operational amplifier (Figure 8.10 - left) was acquired with an X-ray tube voltage and current of 30 kVp and 2 µA, respectively. A magnification factor of 2.7 was defined by having a SDD of 140.5 cm and a SOD of 52 cm. The applied voltages to the detector were the same as the SIM card example. The obtained image is shown in Figure 8.10 (right).

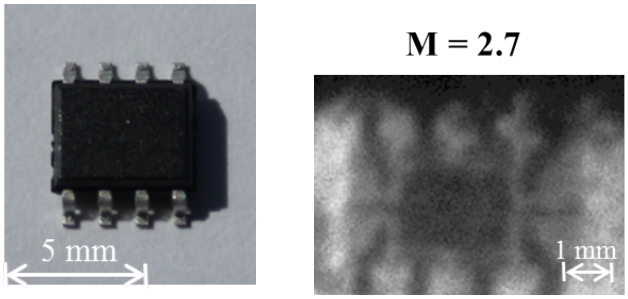

Figure 8.10: Left: Imaged operational amplifier; Right: X-ray transmission image acquired with a magnification factor of 2.7.

The X-ray image of Figure 8.10 (right) shows some artefacts related to non-uniformities of the image, as in the previous image of the SIM card. The operational amplifier is well defined. A good contrast is provided between the contacts, internal circuit and plastic protector of the operational amplifier, which are perfectly visible in the image. Since the datasheet was available, all the object dimensions are known and it was possible to determine a value for the spatial resolution. It was possible to achieve 252 µm measured at the FWHM (Figure 8.11) for the specified magnification. The present setup configuration allowed improving the minimum distance distinguishable in the object.

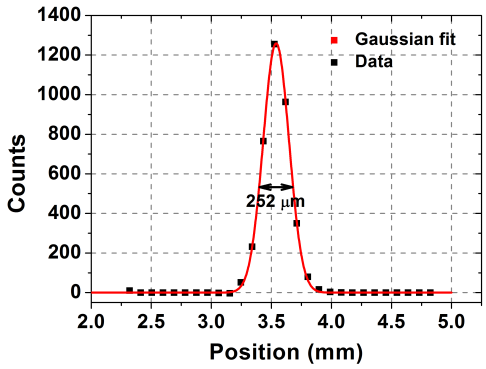

Figure 8.11: LSF obtained by computing the first derivative of the edge response, and fitted Gaussian function, which FWHM is approximately 252 µm (sigma ≈ 107 µm).

In order to study the imaging capabilities of the detector for CT, taking into account the measured properties, particularly LSF, a small exercise was made to have a prospect of a CT image and to analyse the limitation of the spatial resolution in a CT image obtained with this detector. The FT of the LSF gives the MTF of the detector, as referred in Section 7.4. The detector MTF indicates the impulse response of the detector and can be used to predict its influence on the cross-sectional image quality. The obtained CT image of a system is the result of the imaged object itself, $\hat{f}$, the MTF, h, and the bandwidth of the filter, w_{filter}. In the space domain, this can be written as [95]:

$$\hat{f} = [f * h] * w_{filter} \tag{8.1}$$

where * denotes convolution. The corresponding description in the frequency domain can be written as:

$$\hat{F} = [F \times H] \times W_{filter} \tag{8.2}$$

where capitals denote FT. The linearity and space invariance property is assumed to be true for the present detector, since several corrections for the non-uniformity detector response can be applied, such as the flat field and energy corrections. Therefore, using the known MTF and an ideal sinogram corresponding to the phantom shown previously in Figure 5.1 (created using the radon function of Matlab®) it was possible to reconstruct two images: with and without taking into account the detector response function of the detector. The FT of the sinogram was computed and it was multiplied (in the frequency domain) by the MTF of the detector. [95] The results are shown in Figure 8.12.

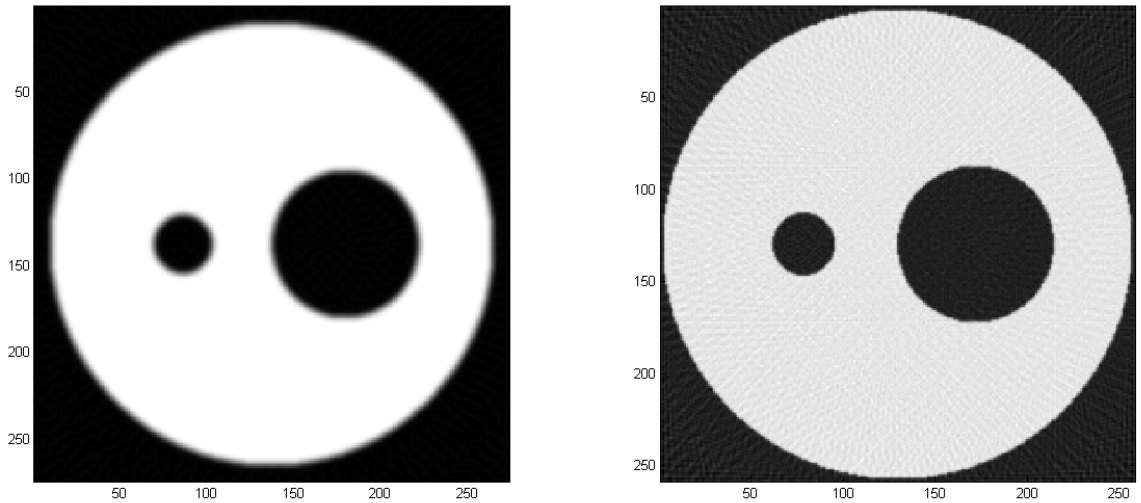

Figure 8.12: Images reconstructed from an ideal sinogram taking into account the detector response (left) and without the blurring caused by the response (right).

The image reconstructed considering the MTF of the detector shows the contours more blurred than the other image, showing a slight degradation of spatial resolution. This means that the spatial resolution in the future CT images will be limited by the detector response and not by the bandwidth of the applied filter. Or moreover the filter may be designed taking into account the detector spatial resolution establishing an appropriate trade off between spatial resolution and noise in the tomographic images.

This detector has shown good imaging capabilities. Generally, its characteristics are good for X-ray imaging applications, such as X-ray transmission or CT. Comparatively to the 2D-THCOBRA detector operating in Ne/CH_4, this detector operating in pure Kr does not allow so high gains (the maximum difference is almost one order of magnitude) and count rates (about one order of magnitude less), its energy resolution is not so good, but has important features for X-ray imaging: the detection efficiency is two orders of magnitude higher and the spatial resolution is considerably better (half of the value). A limitation to apply EWT in image reconstruction can arise from the energy resolution, since the photon energy information may not be accurately measured. However, there is a belief that the poor energy resolution obtained was due to the use of inadequate shaping of the pulses. Despite these aspects, the higher detection efficiency and specially the high spatial resolution achieved make this detector more suitable for X-ray imaging than a detector operating in Ne/CH_4. Furthermore, the noise level (pure Kr) can be further optimized to increase the SNR of the charge pulses and enhance the spatial resolution for lower energies, which will allow the improvement of the image quality. The intensity non-uniformities can, probably, be corrected using a flat field or energy correction (described in Section 3.2.1).

CHAPTER

9

CONCLUSIONS AND FUTURE WORK

This work lead to the development of a 2D-THCOBRA gaseous detector and the application of some detectors and different detector configurations to X-ray transmission and CT imaging. An improvement of the CT system during time was registered: in the beginning the components were aligned by eye and then a prototype of a CT system using an optical bench and laser lines was mounted, optimizing the alignment. At the same time, tools to correct the acquisition conditions and allow the reconstruction of images with better quality were developed and included in the software of the group.

The CT system using the 2D-MHSP detector allowed the reconstruction of images using the energy information, such as the images reconstructed using energy windows and the ones in which the EWT was applied. Different components of the image were enhanced depending on the energy window, which is related with the attenuation coefficients. Concerning the application of EWT, contrast, SNR and CNR enhancements were achieved for the same dose. The contrast was enhanced by 8% and 23%; the SNR enhancement was 10% and 22%; and the CNR enhancement was 11% and 31%, comparing the counting and the EWT images with the integrating image, respectively. Moreover, the multi-slice and 3D images allowed visualizing the components over the longitudinal axis of the object/sample. The 2D-MHSP based detector showed good performance for CT imaging.

2D-THCOBRA detector using a THGEM as a charge pre-amplification stage was used for CT acquisitions of a PMMA phantom with chalk and brass and of a sea snail. The acquisitions made with this detector allowed multi-slice reconstruction of CT images of the PMMA phantom with chalk and brass and the respective 3D images. In this case, although the images showed the samples correctly, evident noise (due to limited spatial resolution and low charge gain) was also seen, diminishing image quality, which was improved in the next detector configurations. With this detector, a flat field correction was performed to the acquisition image of the phantom with chalk and brass, resulting in a more uniform image in which the PMMA cylinder is enhanced. In the future, it is intended to systematically apply this kind of correction and the energy correction, in order to compare both procedures and study the impact on the image quality.

The detectors using a single 2D-THCOBRA, characterized in this work, achieved high gains, allowing a good SNR of the measured pulses, enough for X-ray transmission and CT imaging. When operating in Ne/CH_4, the maximum gains reached were 8×10^3 and 8×10^4 for top and anode electrodes, respectively. For the maximum gain value an energy resolution of 22% (FWHM at 8 keV) was measured. The operation stability showed very good results, keeping the charge gain with a variation less than 5% and allowing a count rate of $1\,\mathrm{MHz\,mm^{-2}}$ for a stable gain. The best spatial resolution measured with this detector was 1.2 mm for photon energies of 3.6 keV. Considering these characteristics, the spatial resolution is the main limiting factor for X-ray imaging applications, however some successful examples of multi-slice and 3D reconstructions of the PMMA phantom with chalk and air, the PMMA

phantom with chalk and brass and the sea snail were obtained. The images obtained with this detector show better general image quality than the 2D-THCOBRA detector coupled with a THGEM.

The 2D-THCOBRA detector operating in pure Kr allows maximum gains of 2×10^4 on top and anode electrodes, and for these gains a marginal energy resolution of 32% (FWHM at 22 keV) was reached, value that can be further improved by optimizing the electronics readout. This detector allows a count rate of 1×10^5 Hz mm^{-2}, a value lower than when operating in Ne/CH_4, but sufficient for the applications presented in this work. The detector reached a very stable operation after the initial charging up effect. Kr is a heavier gas than Ne, promoting a better spatial resolution. For these operation conditions, a spatial resolution of 500 µm was achieved. Generally, this detector seems to have a better image quality than the one operating in Ne/CH_4. The first X-ray transmission images show promising results, although some image artefacts, non-uniformity and granularity are seen in the images. Nevertheless, taking advantage of magnification, a spatial resolution of 252 µm (FWHM) was reached.

The 2D-MHSP based detector has smaller granularity than the 2D-THCOBRA detectors and allows a better position resolution. On the other hand, its manufacture is a more expensive and difficult process than that of 2D-THCOBRA, because of its smaller dimensions. Since the 2D-MHSP detector was already operational in the DRIM lab, it was possible to exploit the energy information of each single photon, while the other detectors were studied and used to test their imaging capabilities.

It was interesting to note the recovery of some CT images using the tool developed to correct, in the sinogram, deviations of the rotation and detector centres during acquisitions. As seen in the example of the PMMA phantom with chalk and brass of Section 6.1, in which any component could be correctly reconstructed, this tool recovered the images and proved to be working properly. In the future, an add-on will be added to this tool, intending to measure and correct an eventual skew of the rotation axis relatively the detector centre. Furthermore, the alignment of the CT system became more robust during time, with an optical bench, its accessories and the line lasers that allow a more effective system alignment in the acquisitions.

The image quality is limited due to the low statistics restricted by the detector count rate and computer processing power. The detector count rate is limited by the electronics readout and, increasing the acquisition time, the processing power needed to be increased in order to be able to reconstruct the cross-sectional images. Nevertheless, image quality improved during time, as did the electronic parameters, gas purity conditions, system alignment, acquisition parameters and processing procedure. To overcome this statistical limitation, iterative algorithms with statistical reconstruction techniques will be considered in the future.

The presented results show that gaseous detectors can be a good solution for X-ray imaging in which a very high spatial resolution is not a major requirement. The developed systems

show suitable characteristics for application in X-ray transmission and CT imaging.

In the future, it is also intended to increase the sensitive detection area by developing a 2D-THCOBRA of $15\times15\,\mathrm{cm}^2$ to apply the detector and CT system in breast and small animal imaging. Also, different gas mixtures of Kr and Xe will be studied. Pure Kr has an X-ray absorption higher than Xe between energies of 15 keV and 34 keV, being more suitable for breast studies. Xe is more adequate for X-ray imaging studies that require higher energies (e.g. small-animal imaging). In order to maximize X-ray absorption in a wider energy range, mixtures of both gases, will be considered and the behaviour of the detector for different mixtures and incident photon energies will be evaluated.

The main goals of this work, the development of the conditions to perform CT acquisitions, were achieved. The systematic studies of characterization and performance will be done in the future to reach a completely operational system. Thus, to allow a characterization of the CT system in terms of uniformity, spatial resolution, CT number, contrast resolution and slice-thickness, proper phantoms, shown in Figure 9.1, with water and biologic equivalent tissues were designed. The phantoms were developed based on standard protocols but adapted for the present case (p.e., detection area) and are presently under construction.

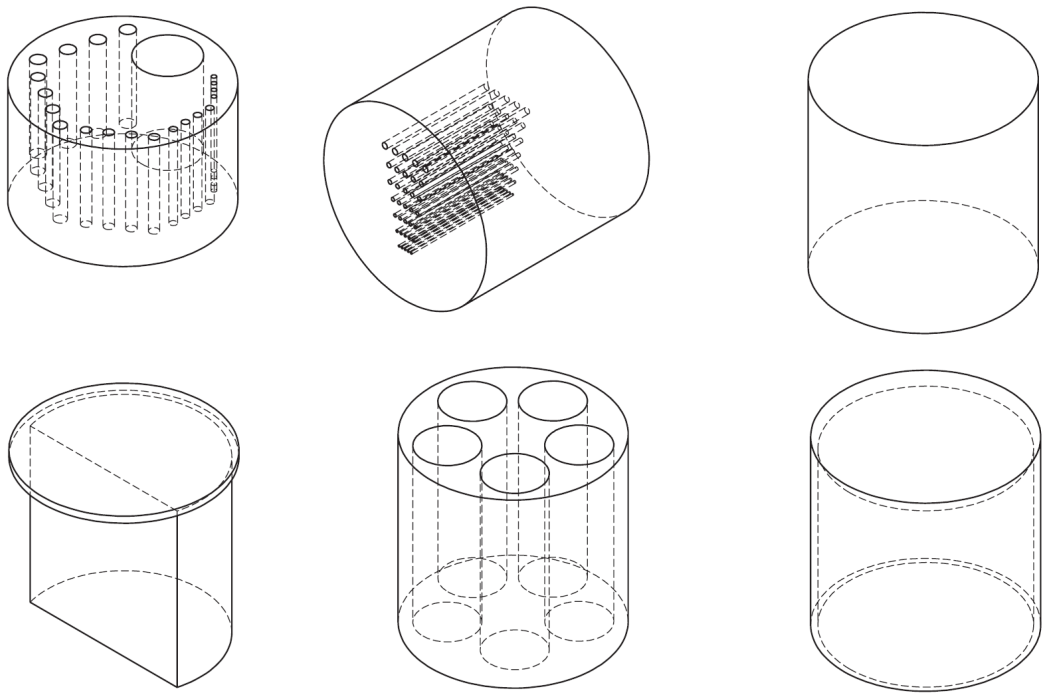

Figure 9.1: Sketch of the phantoms developed to characterize the CT systems in terms of their main characteristics: contrast and spatial resolution, uniformity and CT number.

An important point to recall is that no post-processing was applied to the presented images. Therefore, a great benefit in the image quality improvement can be reached by applying these techniques to the acquired images, which will be considered in the future.

APPENDIXES

Contributions

The work developed under this doctoral program resulted in several contributions, through the publication of articles in scientific journals and presentations at international conferences and workshops.

Publications

Papers in international peer-reviewed journals

- **L. F. N. D. Carramate**, A. L. M Silva, C. D. R. Azevedo, D. S. Covita and J. F. C. A. Veloso; *"THCOBRA X-ray imaging detector operating in Ne/CH_4"*. Accepted for publication in Journal of Instrumentation

- C. D. R. Azevedo, S. Biagi, R. Veenhof, P. M. Correia, A. L. M Silva, **L. F. N. D. Carramate** and J. F. C. A. Veloso; *"Position resolution limits in pure noble gaseous detectors for X-rays energies from 1 to 60 keV"*. Submitted to Physics Letters B

- A. L. M Silva, C. D. R. Azevedo, **L. F. N. D. Carramate**, T. Lopes, I. F. Castro, R. de Oliveira and J. F. C. A. Veloso; *"X-ray Imaging Detector Based on a Position Sensitive THCOBRA with Resistive Line"*. Journal of Instrumentation, 8 P05016, 2013. DOI: 10.1088/1748-0221/8/05/P05016

- **L. F. N. D. Carramate**, F. Nachtrab, M. Firsching, A. L. M. Silva, A. M. da Silva, J. F. C. A. Veloso and N. Uhlmann; *"Energy Resolving CT Systems Using Medipix2 and MHSP Detectors"*. Journal of Instrumentation, 8 C03022, 2013. DOI: 10.1088/1748-0221/8/03/C03022

- **L. F. N. D. Carramate**, C. A. B. Oliveira, A. L. M. Silva, A. M. da Silva, J. M. F. Dos Santos and J. F. C. A. Veloso; *"Multi-slice quantum Computed Tomography system using a MHSP"*. Journal of Instrumentation, 7 C01106, 2012. DOI: 10.1088/1748-0221/7/01/C01106

- **L. F. N. D. Carramate**, C. A. B. Oliveira, A. L. M. Silva, A. M. da Silva, J. M. F. Dos Santos and J. F. C. A. Veloso; *"Energy weighting technique in Quantum Computed Tomography using a MPGD"*. Journal of Instrumentation, 6 C02002, 2011. DOI: 10.1088/1748-0221/6/02/C02002

- C. A. B. Oliveira, C. A. Santos, **L. F. Carramate**, A. L. M. Silva, J. M. F. Dos Santos and J. F. C. A. Veloso; *"Energy Weighting in a 2D-MHSP x-ray Single Photon Detector"*. IEEE Transactions on Nuclear Science, NS57, N3, 2010. DOI: 10.1109/TNS.2010.2044806

Papers in conference proceedings

- J. F. C. A. Veloso, **L. F. N. D. Carramate**, I. F. Castro, P. M. M. Correia, L. M. Moutinho, D. Oliveira, A. C. P. Ribeiro and A. L. M. Silva; *"easyPET - a didatic system"*. Booklet of the 11th International Conference on Hands-on Science, pp 226-230, 21-25 July 2014. ISBN: 978-989-98032-5-1.

- **L. F. N. D. Carramate**, C. A. B. Oliveira, A. L. M. Silva, A. M. da Silva, J. M. F. Dos Santos and J. F. C. A. Veloso; *"Computed Tomography System Using a New MPGD for Small Animal Imaging with Energy Resolving Capability"*. IEEE Nuclear Science Symposium and Medical Imaging Conference Record, pp. 3664-3666, Oct. 29 - Nov. 3, 2012.

- A. L. M. Silva, C. D. R. Azevedo, **L. F. N. D. Carramate**, T. Lopes, R. de Oliveira and J. F. C. A. Veloso; *"X-ray imaging detector based on a 2D sensitive THCOBRA with resistive line readout"*. IEEE Nuclear Science Symposium and Medical Imaging Conference Record, pp. 1160-1164, Oct. 29 - Nov. 3, 2012.

Communications

Oral Communications

- A. L. M. Silva, **L. F. N. D. Carramate**, T. Lopes, C. D. R. Azevedo and J. F. C. A. Veloso; *"Further studies on the position-sensitive THCOBRA for imaging purposes"*. RD51 Collaboration Meeting; July 5-6 2013; Zaragoza, Spain.

- J. F. C. A. Veloso, A. L. M. Silva, **L. F. N. D. Carramate**, C. D. R. Azevedo, D. S. Covita and R. de Oliveira; *"The udot-THCOBRA: a new gaseous electron multiplier concept"*. 3rd International Conference on Micro Pattern Gaseous Detectors; July 1-4 2013; Zaragoza, Spain.

- **L. F. N. D. Carramate**, C. D. R. Azevedo, A. L. M. Silva, T. Lopes, P. Correia, I. F. Castro, A. M. da Silva and J. F. C. A. Veloso; *"CT System With Energy Resolving Capability using a THCOBRA based Detector"*. 15th iWoRID - International Workshop on Radiation Imaging Detectors; June 24-27 2013; Paris, France.

- **L. F. N. D. Carramate**, F. Nachtrab, M. Firsching, A. M. da Silva, J. F. C. A. Veloso and N. Uhlmann; *"Energy Resolving CT Systems Using Medipix2 and MHSP Detectors"*. 14th iWoRID - International Workshop on Radiation Imaging Detectors; July 1-5 2012; Figueira da Foz, Portugal.

- **L. F. N. D. Carramate**, C. A. B. Oliveira, A. L. M. Silva, A. M. da Silva , J. M. F. Dos Santos and J. F. C. A. Veloso; *"Multi-slice Quantum Computed Tomography using*

a MHSP". 13th iWoRID - International Workshop on Radiation Imaging Detectors; July 3-7 2011; Zürich, Switzerland.

- **L. F. N. D. Carramate**, C. A. B. Oliveira, A. L. M. Silva, H. Natal da Luz , C. D. R. Azevedo, M. Peres, A. M. da Silva , J. M. F. Dos Santos and J. F. C. A. Veloso; *"First Steps on Photon Counting Computed Tomography"*. PPHSS - Portuguese Physics for Health Summer School; July 26-28 2010; Covilhã, Portugal.

- **L. F. N. D. Carramate**, C. A. B. Oliveira, A. L. M. Silva, A. M. da Silva , J. M. F. Dos Santos and J. F. C. A. Veloso; *"Energy Weighting Technique in Quantum Computed Tomography using a MPGD"*. 12th International Workshop on Radiation Imaging Detectors; July 11-15 2010; Cambridge, United Kingdom.

- **L. F. N. D. Carramate**, C. A. B. Oliveira, A. L. M. Silva, H. Natal da Luz, C. D. R. Azevedo, M. Peres, A. M. da Silva , J. M. F. Dos Santos and J. F. C. A. Veloso; *"Computed Tomography System Based on a MPGD"*. European Conference on X-Ray Spectrometry; June 20-25 2010; Figueira da Foz, Portugal.

- C. A. B. Oliveira, **L. F. Carramate**, C. A. Santos, A. L. M. Silva, C. D. R. Azevedo, A. L. Ferreira, H. N. da Luz, J. M. F. Dos Santos and J. F. C. A. Veloso; *"Quantum X-ray Imaging using a MHSP: Radiography and Computed Tomography applications"*. Advanced Detectors for Imaging in Physics and Medical Diagnosis; March 2-5 2010; Kolkata, India.

- **L. F. Carramate**, C. A. Santos, C. A. B. Oliveira, A. L. M. Silva, M. Peres, A. M. da Silva, J. M. F. Dos Santos and J. F. C. A. Veloso; *"Small Field of View Quantum Computed Tomography System Based on a MPGD"*. IEEE Nuclear Science Symposium and Medical Imaging Conference; October 25-31 2009; Orlando, Florida, USA.

Poster Communications

- **L. F. N. D. Carramate**, C.D.R Azevedo; A.L.M. Silva, A.M. da Silva and J. F. C. A. Veloso; *"THCOBRA Detector Operation in Pure Kr for Imaging Purposes"*. 16th International Workshop on Radiation Imaging Detectors; June 22-26 2014; Trieste, Italy.

- A. L. M. Silva, **L. F. N. D. Carramate**, E. Oliveri, L. Ropelewski, M. Van Stenis, C.D.R. Azevedo and J. F. C. A. Veloso; *"Triple-GEM detector: in direction of a Xe and Kr sealed X-ray imaging detector"*. 3rd International Conference on Micro Pattern Gaseous Detectors; July 1-4 2013; Zaragoza, Spain.

- A. L. M. Silva, **L. F. N. D. Carramate**, T. Lopes, , C. D. R. Azevedo and J. F. C. A. Veloso; *"Further studies on the position-sensitive THCOBRA for imaging*

purposes". 3rd International Conference on Micro Pattern Gaseous Detectors; July 1-4 2013; Zaragoza, Spain.

- **L. F. N. D. Carramate**, C. A. B. Oliveira, A. L. M. Silva, C. D. R. Azevedo, A M. da Silva and J. F. C. A. Veloso; *"CT System using a MHSP for Small Animal Imaging with Energy Resolving Capability"*. IEEE Nuclear Science Symposium and Medical Imaging Conference; October 29 - November 3 2012; Anaheim, USA.

- A. L. M. Silva, C. D. R. Azevedo, **L. F. N. D. Carramate**, T. Lopes, R. de Oliveira and J. F. C. A. Veloso; *"X-ray imaging detector based on a 2D sensitive THCOBRA with resistive line readout"*. IEEE Nuclear Science Symposium and Medical Imaging Conference; October 29 - November 3 2012; Anaheim, USA.

- **L. F. N. D. Carramate**, C. A. B. Oliveira, A. L. M. Silva, C. D. R. Azevedo, A M. da Silva and J. F. C. A. Veloso; *"Computed Tomography System using a MHSP in Multi-slice Operation"*. IEEE Nuclear Science Symposium and Medical Imaging Conference; October 23-29 2011; Valencia, Spain.

Other Contributions

Papers in international peer-review journals

- A. Trindade, B. Falcão **L. F. N. D. Carramate**, M. I. S. F. Marques, R. A. S. Ferreira and P. S. André; *"Low-cost spectrograph based on a WebCam: a student project"*. International Journal of Electrical Engineering Education, Vol. 51, No 1, 2014. DOI: 10.7227/IJEEE.51.1.1

- C. D. R. Azevedo, F. A. Pereira, T. Lopes, P.Correia, A. L. M. Silva, **L. F. N. D. Carramate** and J. F. C. A. Veloso; *"A Gaseous Compton Camera using a 2D sensitive gaseous photomultiplier for Nuclear Medical Imaging"*. Nuclear Instruments and Methods A, Vol. 732, pp 551-555, 2013 DOI:10.1016/j.nima.2013.05.116

- T. Lopes, A. L. M. Silva, C. D. R. Azevedo, **L. F. N. D. Carramate**, D. S. Covita and J. F. C. A. Veloso; *"Position sensitive VUV gaseous photomultiplier based on Thick-multipliers with resistive line readout"*. Journal of Instrumentation, 8 P09002, 2013 DOI: 10.1088/1748-0221/8/09/P09002

- J. F. C. A. Veloso, A. L. M. Silva, C. A. B. Oliveira, A.L. Gouvêa, C. D. R. Azevedo, **L. F. N. D. Carramate**, H. Natal da Luz and J. M. F. dos Santos; *"Energy resolved X-ray fluorescence imaging based on a micropattern gas detector"*. Spectrochimica Acta B, 65, pp 241-247 , 2010 DOI: 10.1016/j.sab.2010.03.006

- C. D. R. Azevedo, C. A. B. Oliveira, H. Natal da Luz, **L. F. Carramate**, A. L. Ferreira, J. M. F. dos Santos and J. F. C. A. Veloso; *"Gas VUV Photosensors Operating Face-to-Face"*. Nuclear Instruments and Methods A, Vol. 610, pp 238-241, 2009 DOI:10.1016/j.nima.2009.05.146

Oral Communications

- J.C.F.A. Veloso; **L.F.N.D. Carramate**; I.F.C. Castro; P.M.M. Correia; L.M. Moutinho; D. Oliveira; A.C.P. Ribeiro; A.L.M. Silva; *"easyPET"*. Lisbon Mini Maker Faire, 19-21 September 2014, Lisboa, Portugal

- J.C.F.A. Veloso; **L.F.N.D. Carramate**; I.F.C. Castro; P.M.M. Correia; L.M. Moutinho; D. Oliveira; A.C.P. Ribeiro; A.L.M. Silva; *"easyPET - um sistema PET didático"*. FÍSICA 2014 – 19ª Conferência Nacional de Física e 24º Encontro Ibérico para o Ensino da Física, 2-4 September 2014, Lisboa, Portugal

- J.C.F.A. Veloso; **L.F.N.D. Carramate**; I.F.C. Castro; P.M.M. Correia; L.M.C. Moutinho; D. Oliveira; A.C.P. Ribeiro; A.L.M. Silva; *"EasyPET - didactic PET system"*. Hands-on Science, July 21-25 2014, Aveiro, Portugal

- A. L. M. Silva, C. D. R. Azevedo, **L. Carramate** and J. F. C. A. Veloso; *"EDXRF Imaging with new gaseous detectors: examples of qualitative analysis"*. Iber2013, XII Iberian Meeting on Atomic and Molecular Physics; September 9-11 2013; Seville, Spain.

- T. Lopes, A. L. M. Silva, **L. F. N. D. Carramate**, C. D. R. Azevedo and J. F. C. A. Veloso; *"A VUV sensitive gaseous photomultiplier with position capability based on thick multipliers"*. RD51 Collaboration Meeting; July 5-6 2013; Zaragoza, Spain.

- C. D. R. Azevedo, F. A. Pereira, T. Lopes, P. M. M. Correia, A. L. M. Silva, **L. F. N. D. Carramate** and J. F. C. A. Veloso; *"A Gaseous Compton Camera with MPGD-based readout"*. 3rd International Conference on Micro Pattern Gaseous Detectors; July 1-4 2013; Zaragoza, Spain.

- C. D. R. Azevedo, F. Pereira, T. Lopes, A. L. M. Silva, **L. Carramate**, J. M. F. dos Santos and J. F. C. A. Veloso; *"A Gaseous Compton Camera for Nuclear Medical Imaging"*. 14th iWoRID - International Workshop on Radiation Imaging Detectors; 1-5 July 2012; Figueira da Foz, Portugal

Poster Communications

- J.C.F.A. Veloso; **L.F.N.D. Carramate**; I.F.C. Castro; P.M.M. Correia; L.M.C. Moutinho; D. Oliveira; A.C.P. Ribeiro; A.L.M. Silva, A.I. Veloso; *"easyPET: a user friendly*

PET system for didactic purposes". 7th edition of the International Conference on New Developments In Photodetection – NDIP14, 30 June - 4 July 2014, Tours, France

- T. Lopes, A. L. M. Silva, **L. F. N. D. Carramate**, C. D. R. Azevedo and J. F. C. A. Veloso; *"VUV Sensitive Gaseous Photomultiplier with Position Capability Based on Thick Multipliers"*. 3rd International Conference on Micro Pattern Gaseous Detectors; July 1-4 2013; Zaragoza, Spain.

- J. F. C. A. Veloso, C.D.R. Azevedo, F. A. Pereira, T. Lopes, P. Correia, A. L. M. da Silva and **L. F. N. D. Carramate**; *"A Gaseous Compton Camera using a 2D sensitive gaseous photomultiplier for Nuclear Medical Imaging"*. 13th Vienna Conference on Instrumentation; February 11-15 2013; Vienna, Austria

REFERENCES

[1] J. Hsieh, "*Computed tomography: principles, design, artifacts, and recent advances*", SPIE & Jonh Wiley& Sons, Inc., 2009.

[2] F. D. Amaro et al., "*The Thick-COBRA: a new gaseous electron multiplier for radiation detectors*", Journal of Instrumentation, vol. 5, no. 10, pp. P10002, 2010.

[3] T. M. Buzug, "*Computed Tomography: from Photon Statistics to Modern Cone-Beam CT*", Springer-Verlag, 2008.

[4] J. Bushberg et al., "*The essential physics of medical imaging*", Lippincott Williams & Wilkins, 2002.

[5] G. F. Knoll, "*Radiation detection and measurement*", Jonh Wiley & Sons, Inc, 2010.

[6] W. R. Hendee and E. R. Ritenour, "*Medical Imaging Physics*", Wiley-Liss, 2002.

[7] K. Iniewski, "*Medical Imaging Principles detectors and applications*", Jonh Wiley & Sons, Inc, 2009.

[8] C. Bert et al., "*Computed tomography using the Medipix1 chip*", Nuclear Instruments and Methods in Physics Research Section A: Accelerators, Spectrometers, Detectors and Associated Equipment, vol. 509, no. 1-3, pp. 240–250, 2003.

[9] M. Berger et al., XCOM: Photon Cross Sections Database, http://www.nist.gov/pml/data/xcom/index.cfm.

[10] E. Podgorsak, "*Radiation physics for medical physicists*", Springer-Verlag, 2010.

[11] S. Ricq, F. Glasser and M. Garcin, "*CdTe and CdZnTe detectors behavior in X-ray computed tomography conditions*", Nuclear Instruments and Methods in Physics Research Section A: Accelerators, Spectrometers, Detectors and Associated Equipment, vol. 442, no. 1-3, pp. 45–52, 2000.

[12] W. A. Kalender, "*Computed Tomography - Fundamentals, System Technology, Image Quality, Applications*", Publicis Publishing, 2011.

[13] S. Tavernier et al., "*Radiation detectors for medical applications*", Springer-Verlag, 2006.

[14] A. D. Guerra, "*Ionizing Radiation Detectors for Medical Imaging*", World Scientific Publishing Co. Re. Ltd., 2004.

[15] J. P. Schlomka et al., "*Experimental feasibility of multi-energy photon-counting K-edge imaging in pre-clinical computed tomography*", Physics in medicine and biology, vol. 53, no. 15, pp. 4031–4047, 2008.

[16] C. Xu et al., "*Preliminary evaluation of a silicon strip detector for photon-counting spectral CT*", Nuclear Instruments and Methods in Physics Research Section A: Accelerators, Spectrometers, Detectors and Associated Equipment, vol. 677, pp. 45–51, 2012.

[17] A. C. Silva et al., "*Dual-Energy (Spectral) CT : Applications in Ab- dominal Imaging*", RadioGraphics, vol. 31, no. 4, pp. 1031–1047, 2011.

[18] C. A. Coursey et al., "*Dual-Energy Multidetector CT : How Does It Work , What Can It Tell Us , and When Can We Use It in Abdominopelvic Imaging*", RadioGraphics, vol. 30, no. 4, pp. 1037–1052, 2010.

[19] H. Alkadhi and S. Leschka, "*Dual-energy CT: Principles, clinical value and potential applications in forensic imaging*", Journal of Forensic Radiology and Imaging, vol. 1, no. 4, pp. 180–185, 2013.

[20] M. Ohana et al., "*Thoracic dual energy CT: Acquisition protocols, current applications and future developments.*", Diagnostic and interventional imaging, pp. 1–10, 2014.

[21] D. Vavrik et al., "*First tests of a Medipix-1 pixel detector for X-ray dynamic defectoscopy*", Nuclear Instruments and Methods in Physics Research Section A: Accelerators, Spectrometers, Detectors and Associated Equipment, vol. 487, no. 1-2, pp. 216–223, 2002.

[22] C. Xu et al., "*Energy resolution of a segmented silicon strip detector for photon-counting spectral CT*", Nuclear Instruments and Methods in Physics Research Section A: Accelerators, Spectrometers, Detectors and Associated Equipment, vol. 715, pp. 11–17, 2013.

[23] X. Liu et al., "*A Silicon-Strip Detector for Photon-Counting Spectral CT : Energy Resolution*", vol. 61, no. 3, pp. 1099–1105, 2014.

[24] H. Bornefalk and M. Danielsson, "*Photon-counting spectral computed tomography using silicon strip detectors: a feasibility study.*", Physics in medicine and biology, vol. 55, no. 7, pp. 1999–2022, 2010.

[25] M. Persson et al., "*Energy-resolved CT imaging with a photon-counting silicon-strip detector*", In *Proc. SPIE 9033, Medical Imaging 2014: Physics of Medical Imaging*, 2014.

[26] O. Hagiwara et al., "*Energy-discrimination X-ray computed tomography system utilizing a silicon-PIN detector and its application to 2.0-keV-width K-edge imaging*", Nuclear Instruments and Methods in Physics Research Section A: Accelerators, Spectrometers, Detectors and Associated Equipment, vol. 638, no. 1, pp. 165–170, 2011.

[27] AMPTEK, XR-100CR Si-PIN X-Ray Detector, http://www.amptek.com/products/xr-100cr-si-pin-x-ray-detector/.

[28] M. N. Boone et al., "*High spectral and spatial resolution X-ray transmission radiography and tomography using a Color X-ray Camera.*", Nuclear instruments & methods in physics research. Section A, Accelerators, spectrometers, detectors and associated equipment, vol. 735, pp. 644–648, 2014.

[29] I. Ordavo et al., "*A new pnCCD-based color X-ray camera for fast spatial and energy-resolved measurements*", Nuclear Instruments and Methods in Physics Research Section A: Accelerators, Spectrometers, Detectors and Associated Equipment, vol. 654, no. 1, pp. 250–257, 2011.

[30] O. Scharf et al., "*Compact pnCCD-based X-ray camera with high spatial and energy resolution: a color X-ray camera.*", Analytical chemistry, vol. 83, no. 7, pp. 2532–8, 2011.

[31] P. M. Shikhaliev, T. Xu and S. Molloi, "*Photon counting computed tomography: Concept and initial results*", Medical Physics, vol. 32, no. 2, pp. 427, 2005.

[32] P. Shikhaliev, J. Ducote and S. Molloi, "*Quantum efficiency of the MCP detector: Monte Carlo calculation*", IEEE Transactions on Nuclear Science, vol. 52, no. 5, pp. 1257–1262, 2005.

[33] P. M. Shikhaliev et al., "*Scanning-slit photon counting x-ray imaging system using a microchannel plate detector*", Medical Physics, vol. 31, no. 5, pp. 1061, 2004.

[34] P. M. Shikhaliev, "*Energy-resolved computed tomography: first experimental results.*", Physics in medicine and biology, vol. 53, no. 20, pp. 5595–613, 2008.

[35] P. M. Shikhaliev, "*Computed tomography with energy-resolved detection: a feasibility study.*", Physics in medicine and biology, vol. 53, no. 5, pp. 1475–95, 2008.

[36] P. M. Shikhaliev, "*Tilted angle CZT detector for photon counting/energy weighting x-ray and CT imaging.*", Physics in medicine and biology, vol. 51, no. 17, pp. 4267–87, 2006.

[37] P. M. Shikhaliev, "*Projection x-ray imaging with photon energy weighting: experimental evaluation with a prototype detector.*", Physics in medicine and biology, vol. 54, no. 16, pp. 4971–92, 2009.

[38] P. M. Shikhaliev and S. G. Fritz, "*Photon counting spectral CT versus conventional CT: comparative evaluation for breast imaging application.*", Physics in medicine and biology, vol. 56, no. 7, pp. 1905–30, 2011.

[39] E. Roessl et al., "*Preclinical spectral computed tomography of gold nano-particles*", Nuclear Instruments and Methods in Physics Research Section A: Accelerators, Spectrometers, Detectors and Associated Equipment, vol. 648, pp. S259–S264, 2011.

[40] K. Kowase and K. Ogawa, "*Photon Counting X-ray CT System with a Semiconductor Detector*", 2006 IEEE Nuclear Science Symposium Conference Record, pp. 3119–3123, 2006.

[41] G. Healthcare, LightSpeed® VCT XT, http://www.gehealthcare.com/dose/media/6038/2009_10_-_discovery_pet_ct_690_lightspeed_vct_xt_insert_-_fv.pdf.

[42] J. S. Iwanczyk et al., "*Photon Counting Energy Dispersive Detector Arrays for X-ray Imaging.*", IEEE transactions on nuclear science, vol. 56, no. 3, pp. 535–542, 2009.

[43] R. Levinson et al., Clinical Use of Photon Counting Detectors in CT, http://www.aapm.org/meetings/amos2/pdf/42-11928-41219-702.pdf.

[44] W. Stomp, Philips Introduces IQon, World′s First Spectral Detector CT, http://www.medgadget.com/2013/12/philips-introduces-iqon-worlds-first-spectral-detector-ct.html.

[45] P. Radiology, IQon Spectral CT, http://www.healthcare.philips.com/main/clinicalspecialities/radiology/solutions/IQon.html#modulepage=360.

[46] I. T. News, Philips Introduces IQon Spectral CT System at RSNA 2013, http://www.itnonline.com/article/philips-introduces-iqon-spectral-ct-system-rsna-2013.

[47] D. Europe, Simultaneous conventional and spectral CT imaging, http://www.google.pt/url?sa=t&rct=j&q=&esrc=s&source=web&cd=8&cad=rja&uact=8&ved=0CGwQFjAH&url=http://www.dieurope.com/LiteratureRetrieve.aspx?ID=117350&ei=pInkU52BGeKc0AW0q4CYBg&usg=AFQjCNGS0HlRhoorQn08a-UGg1SpMWVz-A&sig2=ZnUwmybcco5h1I0xqnYifw&bvm=bv.72197243,bs.1,d.d2k.

[48] E. Aprile et al., "*Noble Gas Detectors*", Wiley-VCH, 2006.

[49] W. Blum, W. Riegler and L. Rolandi, "*Particle Detection with Drift Chambers*", Springer-Verlag, 2008.

[50] W. Leo, "*Techniques for Nuclear and Particle Physics Experiments*", Springer-Verlag, vol. 58, 1987.

[51] G. Steinhauser and K. Buchtela, "*Handbook of Radioactivity Analysis*", Elsevier, pp. 191–231, 2012.

[52] G. C. Smith, J. Fischer and V. Radeka, "*Photoelectron range limitation to the spatial resolution for X-rays in gas proportional chambers*", IEEE Transactions on Nuclear Science, no. 1, pp. 111–115, 1984.

[53] A. LIQUIDE, Noble gases: Krypton, Neon, Xenon, http://www.airliquide.com/en/company/our-businesses-our-products/air-gases/noble-gases-krypton-neon-xenon.html.

[54] M. L. Klein and J. A. Venables, "*Rare Gas Solids*", Academic Press, 1976.

[55] J. F. C. A. Veloso, J. M. F. Santos and C. A. N. Conde, "*A proposed new microstructure for gas radiation detectors: The microhole and strip plate*", Review of Scientific Instruments, vol. 71, no. 6, pp. 2371–2376, 2000.

[56] A. Oed, "*Position-sensitive detector with microstrip anode for electron multiplication with gases*", Nuclear Instruments and Methods in Physics Research Section A: Accelerators, Spectrometers, Detectors and Associated Equipment, vol. 263, pp. 351–359, 1988.

[57] L. Shekhtman, "*Micro-pattern gaseous detectors*", Nuclear Instruments and Methods in Physics Research Section A: Accelerators, Spectrometers, Detectors and Associated Equipment, vol. 494, pp. 128–141, 2002.

[58] F. Sauli, "*GEM: A new concept for electron amplification in gas detectors*", Nuclear Instruments and Methods in Physics Research Section A: Accelerators, Spectrometers, Detectors and Associated Equipment, vol. 386, no. 2-3, pp. 531–534, 1997.

[59] S. Bachmann et al., "*Development and applications of the gas electron multiplier*", Nuclear Instruments and Methods in Physics Research Section A: Accelerators, Spectrometers, Detectors and Associated Equipment, vol. 471, no. 1-2, pp. 115–119, 2001.

[60] F. Sauli, "*Imaging with the gas electron multiplier*", Nuclear Instruments and Methods in Physics Research Section A: Accelerators, Spectrometers, Detectors and Associated Equipment, vol. 580, no. 2, pp. 971–973, 2007.

[61] J. F. C. A. Veloso et al., "*The microhole and strip plate gas detector: Initial results*", Review of Scientific Instruments, vol. 73, no. 2, pp. 488, 2002.

[62] H. Natal da Luz et al., "*MHSP with position detection capability*", Nuclear Instruments and Methods in Physics Research Section A: Accelerators, Spectrometers, Detectors and Associated Equipment, vol. 573, no. 1-2, pp. 191–194, 2007.

[63] H. Natal da Luz et al., "*A simple X-ray position detection system based on a MHSP*", Nuclear Instruments and Methods in Physics Research Section A: Accelerators, Spectrometers, Detectors and Associated Equipment, vol. 580, no. 2, pp. 1083–1086, 2007.

[64] H. Natal da Luz et al., "*Micro-Hole and Strip Plate (MHSP) operation in CF_4*", Nuclear Instruments and Methods in Physics Research Section A: Accelerators, Spectrometers, Detectors and Associated Equipment, vol. 580, no. 1, pp. 286–288, 2007.

[65] H. Natal da Luz et al., "*MHSP operation in pure xenon*", Nuclear Instruments and Methods in Physics Research Section A: Accelerators, Spectrometers, Detectors and Associated Equipment, vol. 552, no. 3, pp. 259–262, 2005.

[66] J. Veloso et al., "*High-rate operation of the Micro-Hole and Strip Plate gas detector*", Nuclear Instruments and Methods in Physics Research Section A: Accelerators, Spectrometers, Detectors and Associated Equipment, vol. 580, no. 1, pp. 362–365, 2007.

[67] F. D. Amaro et al., "*Operation of MHSP multipliers in high pressure pure noble-gas*", Journal of Instrumentation, no. 1 P04003, 2006.

[68] H. Natal da Luz et al., "*Single Photon Counting X-Ray Imaging System Using a Micro Hole and Strip Plate*", IEEE Transactions on Nuclear Science, vol. 55, no. 4, pp. 2341–2345, 2008.

[69] R. Chechik et al., "*Thick GEM-like hole multipliers: properties and possible applications*", Nuclear Instruments and Methods in Physics Research Section A: Accelerators, Spectrometers, Detectors and Associated Equipment, vol. 535, no. 1-2, pp. 303–308, 2004.

[70] A. Breskin et al., "*A concise review on THGEM detectors*", Nuclear Instruments and Methods in Physics Research Section A: Accelerators, Spectrometers, Detectors and Associated Equipment, vol. 598, no. 1, pp. 107–111, 2009.

[71] C. Shalem et al., "*Advances in Thick GEM-like gaseous electron multipliers Part I: atmospheric pressure operation*", Nuclear Instruments and Methods in Physics Research Section A: Accelerators, Spectrometers, Detectors and Associated Equipment, vol. 558, no. 2, pp. 475–489, 2006.

[72] M. Cortesi et al., "*THGEM operation in Ne and Ne/CH_4*", Journal of Instrumentation, vol. 4, no. 08, pp. P08001–P08001, 2009.

[73] C. Shalem et al., "*Advances in thick GEM-like gaseous electron multipliers Part II: Low-pressure operation*", Nuclear Instruments and Methods in Physics Research Section A: Accelerators, Spectrometers, Detectors and Associated Equipment, vol. 558, no. 2, pp. 468–474, 2006.

[74] COMSOL, Multiphysics Software Product Suite, http://www.comsol.com/products.

[75] A. L. M. Silva et al., "*X-ray imaging detector based on a position sensitive THCOBRA with resistive line*", Journal of Instrumentation, vol. 8, no. 05, pp. P05016–P05016, 2013.

[76] J. Giersch, D. Niederlöhner and G. Anton, "*The influence of energy weighting on X-ray imaging quality*", Nuclear Instruments and Methods in Physics Research Section A: Accelerators, Spectrometers, Detectors and Associated Equipment, vol. 531, pp. 68–74, 2004.

[77] D. Niederlöhner et al., "*The energy weighting technique: measurements and simulations*", Nuclear Instruments and Methods in Physics Research Section A: Accelerators, Spectrometers, Detectors and Associated Equipment, vol. 546, no. 1-2, pp. 37–41, 2005.

[78] G. Patatoukas et al., "*The effect of energy weighting on the SNR under the influence of non-ideal detectors in mammographic applications*", Nuclear Instruments and Methods in Physics Research Section A: Accelerators, Spectrometers, Detectors and Associated Equipment, vol. 569, no. 2, pp. 260–263, 2006.

[79] L. Smekal et al., "*Geometric misalignment and calibration in cone-beam tomography*", Medical Physics, vol. 31, no. 12, pp. 3242–3266, 2004.

[80] I. Vidal-Migallon et al., "*Simulation of mechanical misalignments in a cone- beam micro-CT system*", IEEE Nuclear Science Symposium Conference Record, vol. M10-270, pp. 5007–5009, 2008.

[81] L. Shepp, S. Hilal and R. Schulz, "*The tuning fork artifact in computerized tomography*", Computer Graphics and Image Processing, vol. 10, no. 3, pp. 246–255, 1979.

[82] S. G. Azevedo et al., "*Calculation of the Rotational Centers in Computed Tomography Sinograms*", IEEE Transactions on Nuclear Science, vol. 37, no. 4, pp. 1525–1540, 1990.

[83] Y. Sun, Y. Hou and J. Hu, "*Reduction of artifacts induced by misaligned geometry in cone-beam CT.*", IEEE Transactions on Biomedical Engineering, vol. 54, no. 8, pp. 1461–71, 2007.

[84] P. Acarnley, "*Stepping Motors - a guide to theory and practice*", Institution of Engineering and Technology, 2002.

[85] A. Francisco, "*Motores Eléctricos*", ETEP - Edições Técnicas e Profissionais, 2008.

[86] V. V. Athani, "*Stepper Motors - Fundamentals, Applications and Design*", New Age International, 1997.

[87] Arduino, Arduino Uno, http://arduino.cc/en/Main/arduinoBoardUno.

[88] Arduino, Arduino Motor Shield, http://arduino.cc/en/Main/ArduinoMotorShieldR3.

[89] S. Microelectronics, L298 DUAL FULL-BRIDGE DRIVER, http://www.st.com/st-web-ui/static/active/en/resource/technical/document/datasheet/CD00000240.pdf.

[90] L. F. N. D. Carramate et al., "*Energy weighting technique in Quantum Computed Tomography using a MPGD*", Journal of Instrumentation, vol. 6, no. 02, pp. C02002, 2011.

[91] Quadrant - Engineering Plastic Products, Ketron 1000 PEEK, http://www.quadrantplastics.com/fileadmin/quadrant/documents/QEPP/EU/Product_Data_Sheets_PDF/AEP/Ketron_1000_PEEK_PDS_E_25042014.pdf.

[92] Henkel, Hysol TRA-BOND 2116, https://tds.us.henkel.com//NA/UT/HNAUTTDS.nsf/web/23343FD6F2EFC63085257589006B254C/$File/TRA-BOND 2116-EN.pdf.

[93] S. G. Group, St 171® and St 172 - Sintered Porous Getters, http://www.saesgetters.com/sites/default/files/St 171 - 172_Sintered Porous Getters_1.pdf.

[94] C. Epstein, "*Introduction to the mathematics of medical imaging*", Society of Industrial and Applied Mathematics, 2008.

[95] A. C. Kak and M. Slaney, "*Principles of computerized tomographic imaging*", Society of Industrial and Applied Mathematics, 2001.

[96] A. T. Dhawan, "*Medical Image Analysis*", Jonh Wiley & Sons, Inc, 2003.

[97] L. W. Goldman, "*Principles of CT and CT technology.*", Journal of nuclear medicine technology, vol. 35, no. 3, pp. 115–128, 2007.

[98] Mathworks, iradon, http://www.mathworks.com/help/images/ref/iradon.html.

[99] F. V. Hessman and E. Modrow, "*An Introduction to Astronomical Image Processing with ImageJ*", (C) Copyright Hessman & Modrow, 2008.

[100] D. Davidson et al., "*Limitations to flat-field correction methods when using an X-ray spectrum*", Nuclear Instruments and Methods in Physics Research Section A: Accelerators, Spectrometers, Detectors and Associated Equipment, vol. 509, no. 1-3, pp. 146–150, 2003.

[101] J. F. C. A. Veloso et al., "*Energy resolved X-ray fluorescence imaging based on a micropattern gas detector*", Spectrochimica Acta Part B: Atomic Spectroscopy, vol. 65, no. 3, pp. 241–247, 2010.

[102] L. F. N. D. Carramate et al., "*Multi-slice quantum Computed Tomography system using a MHSP*", Journal of Instrumentation, vol. 7, no. 01, pp. C01106–C01106, 2012.

[103] X. Llopart et al., "*Medipix2: A 64-k pixel readout chip with 55-μm square elements working in single photon counting mode*", IEEE Transactions on Nuclear Science, vol. 49, no. 5, pp. 2279–2283, 2002.

[104] T. M. Collaboration, The Medipix2 Chip, https://medipix.web.cern.ch/medipix/pages/medipix2/medipix2.php.

[105] L. F. N. D. Carramate et al., "*Energy resolving CT systems using Medipix2 and MHSP detectors*", Journal of Instrumentation, vol. 8, no. 03, pp. C03022, 2013.

[106] G. H. Chen and S. Leng, "*A new data consistency condition for fan-beam projection data*", Medical Physics, vol. 32, no. 4, pp. 961, 2005.

[107] J. Xu, K. Taguchi and B. M. W. Tsui, "*Statistical projection completion in X-ray CT using consistency conditions.*", IEEE transactions on medical imaging, vol. 29, no. 8, pp. 1528–40, 2010.

[108] C. D. R. Azevedo et al., "*Position resolution limits in pure noble gaseous detectors for X-rays energies from 1 to 60 keV*", submitted to Physcis Letters B, .

[109] L. F. N. D. Carramate et al., "*THCOBRA X-ray imaging detector operating in Ne/CH4*", accepted for publication in JINST, .

[110] S. Smith, "*The Scientist and Engineer's Guide to Digital Signal Processing*", California Technical Publishing, 1997.

[111] F. Horne, How are seashells created? Or any other shell, such as a snail's or a turtle's?, http://www.scientificamerican.com/article/how-are-seashells-created/.

[112] R. Nordsieck, Snails (Gastropoda): Body Construction, http://molluscs.at/gastropoda/index.html?/gastropoda/morphology/body_construction.html.

[113] J. M. Maia et al., "*THGEM electron multiplier in high pressure Kr*", Journal of Instrumentation, vol. 4, no. 10, pp. P10006–P10006, 2009.

[114] M. S. Hemm and M. H. Ari, "*^{54}Xe and ^{36}Kr gas filled proportional counters and characteristic X-rays detection*", American Journal of Physics and Applications, vol. 2, no. 4, pp. 95–103, 2014.

[115] P. M. M. Correia et al., "*A dynamic method for charging-up calculations: the case of GEM*", Journal of Instrumentation, vol. 9, no. 07, pp. P07025–P07025, 2014.

[116] M. Alfonsi et al., "*Simulation of the dielectric charging-up effect in a GEM detector*", Nuclear Instruments and Methods in Physics Research Section A: Accelerators, Spectrometers, Detectors and Associated Equipment, vol. 671, pp. 6–9, 2012.

[117] B. Azmoun et al., "*A Study of Gain Stability and Charging Effects in GEM Foils*", 2006 IEEE Nuclear Science Symposium Conference Record, vol. 2, pp. 3847–3851, 2006.